

Jordan Journal of Mechanical and Industrial Engineering (JJMIE)

JJMIE is a high-quality scientific journal devoted to fields of Mechanical and Industrial Engineering. It is published by Hashemite University in corporation with the Jordanian Scientific Research Support Fund.

EDITORIAL BOARD

Guest editor

Prof. Mohammad Ahmad Hamdan

Editorial board

Prof. **Mohammad Ahmad Hamdan**
University of Jordan

Prof. **Naseem Sawaqed**
Mutah University

Prof. **Amin Al Robaidi**
Al Balqa Applied University

Prof. Mohammad AL-Tahat
University of Jordan

Editor-in-Chief

Prof. Ahmed M. Al-Ghandoor

Prof. **Naser Al-Huniti**
University of Jordan

Prof. **Mohammad Hayajneh**
Jordan University of Science and Technology

Prof. Suhil Kiwan
Jordan University of Science and Technology

THE INTERNATIONAL ADVISORY BOARD

Abu-Qudais, Mohammad
Jordan University of Science & Technology, Jordan

Abu-Mulaweh, Hosni
Purdue University at Fort Wayne, USA

Afaneh Abdul-Hafiz
Robert Bosch Corporation, USA

Afonso, Maria Dina
Institute Superior Tecnico, Portugal

Badiru, Adedji B.
The University of Tennessee, USA

Bejan, Adrian
Duke University, USA

Chalhoub, Nabil G.
Wayne State University, USA

Cho, Kyu-Kab
Pusan National University, South Korea

Dincer, Ibrahim
University of Ontario Institute of Technology,
Canada

Douglas, Roy
Queen's University, U. K

El Bassam, Nasir
International Research Center for Renewable
Energy, Germany

Haik, Yousef
United Arab Emirates University, UAE

Jaber, Jamal
Al- Balqa Applied University, Jordan

Jubran, Bassam
Ryerson University, Canada

Kakac, Sadik
University of Miami, USA

Khalil, Essam-Eddin
Cairo University, Egypt

Mutoh, Yoshiharu
Nagaoka University of Technology, Japan

Pant, Durbin
Iowa State University, USA

Riffat, Saffa
The University of Nottingham, U. K

Saghir, Ziad
Ryerson University, Canada

Sarkar, MD. Abdur Rashid
Bangladesh University of Engineering &
Technology, Bangladesh

Siginer, Dennis
Wichita State University, USA

Sopian, Kamaruzzaman
University Kebangsaan Malaysia, Malaysia

Tzou, Gow-Yi
Yung-Ta Institute of Technology and Commerce,
Taiwan

EDITORIAL BOARD SUPPORT TEAM

Language Editor

Dr. Qusai Al-Debyan

Publishing Layout

Eng. Ali Abu Salimeh

SUBMISSION ADDRESS:

Prof. Ahmed Al-Ghandoor, Editor-in-Chief
Jordan Journal of Mechanical & Industrial Engineering,
Hashemite University,
PO Box 330127, Zarqa, 13133 , Jordan
E-mail: jjmie@hu.edu.jo



Hashemite Kingdom of Jordan



Hashemite University

Jordan Journal of
Mechanical and Industrial Engineering

JJMIIE

An International Peer-Reviewed Scientific Journal
Financed by Scientific Research Support Fund

Special Issue

<http://jjmie.hu.edu.jo/>

ISSN 1995-6665

Jordan Journal of Mechanical and Industrial Engineering (JJMIE)

JJMIE is a high-quality scientific journal devoted to fields of Mechanical and Industrial Engineering. It is published by The Jordanian Ministry of Higher Education and Scientific Research in corporation with Hashemite University.

Introduction: The Editorial Board is very committed to build the Journal as one of the leading international journals in mechanical and industrial engineering sciences in the next few years. With the support of the Ministry of Higher Education and Scientific Research and Jordanian Universities, it is expected that a heavy resource to be channeled into the Journal to establish its international reputation. The Journal's reputation will be enhanced from arrangements with several organizers of international conferences in publishing selected best papers of the conference proceedings.

Aims and Scope: *Jordan Journal of Mechanical and Industrial Engineering* (JJMIE) is a refereed international journal to be of interest and use to all those concerned with research in various fields of, or closely related to, mechanical and industrial engineering disciplines. *Jordan Journal of Mechanical and Industrial Engineering* aims to provide a highly readable and valuable addition to the literature which will serve as an indispensable reference tool for years to come. The coverage of the journal includes all new theoretical and experimental findings in the fields of mechanical and industrial engineering or any closely related fields (Materials, Manufacturing, Management, Design, Thermal and Fluid, Energy, Control, Mechatronics, and Biomedical). The journal also encourages the submission of critical review articles covering advances in recent research of such fields as well as technical notes.

Guide for Authors

Manuscript Submission:

High-quality submissions to this new journal are welcome now and manuscripts may be either submitted online or email.

Online: For online and email submission upload one copy of the full paper including graphics and all figures at the online submission site, accessed via <http://jjmie.hu.edu.jo>. The manuscript must be written in MS Word 2010 Format. All correspondence, including notification of the Editor's decision and requests for revision, takes place by e-mail and via the Author's homepage, removing the need for a hard-copy paper trail.

Submission address and contact:

Prof. Ahmed Al-Ghandoor
Editor-in-Chief
Jordan Journal of Mechanical & Industrial Engineering,
Hashemite University,
PO Box 330127, Zarqa, 13115, Jordan
E-mail: jjmie@hu.edu.jo

Types of contributions: Original research papers and Technical reports

Corresponding author: Clearly indicate who is responsible for correspondence at all stages of refereeing and publication, including post-publication. Ensure that telephone and fax numbers (with country and area code) are provided in addition to the e-mail address and the complete postal address. Full postal addresses must be given for all co-authors.

Original material: Submission of an article implies that the work described has not been published previously (except in the form of an abstract or as part of a published lecture or academic thesis), that it is not under consideration for publication elsewhere, that its publication is approved by all authors and that, if accepted, it will not be published elsewhere in the same form, in English or in any other language, without the written consent of the Publisher. Authors found to be deliberately contravening the submission guidelines on originality and exclusivity shall not be considered for future publication in this journal.

Withdrawing: If the author chooses to withdraw his article after it has been assessed, he shall reimburse JJMIE with the cost of reviewing the paper.

Manuscript Preparation:

General: Editors reserve the right to adjust style to certain standards of uniformity. Original manuscripts are discarded after publication unless the Publisher is asked to return original material after use. Please use MS Word 2010 for the text of your manuscript.

Structure: Follow this order when typing manuscripts: Title, Authors, Authors title, Affiliations, Abstract, Keywords, Introduction, Main text, Conclusions, Acknowledgements, Appendix, References, Figure Captions, Figures and then Tables. Please supply figures imported into the text AND also separately as original graphics files. Collate acknowledgements in a separate section at the end of the article and do not include them on the title page, as a footnote to the title or otherwise.

Text Layout: Use 1.5 line spacing and wide (3 cm) margins. Ensure that each new paragraph is clearly indicated. Present tables and figure legends on separate pages at the end of the manuscript. If possible, consult a recent issue of the journal to become familiar with layout and conventions. All footnotes (except for table and corresponding author footnotes) should be identified with superscript Arabic numbers. To conserve space, authors are requested to mark the less important parts of the paper (such as records of experimental results) for printing in smaller type. For long papers (more than 4000 words) sections which could be deleted without destroying either the sense or the continuity of the paper should be indicated as a guide for the editor. Nomenclature should conform to that most frequently used in the scientific field concerned. Number all pages consecutively; use 12 or 10 pt font size and standard fonts.

Corresponding author: Clearly indicate who is responsible for correspondence at all stages of refereeing and publication, including post-publication. The corresponding author should be identified with an asterisk and footnote. Ensure that telephone and fax numbers (with country and area code) are provided in addition to the e-mail address and the complete postal address. Full postal addresses must be given for all co-authors. Please consult a recent journal paper for style if possible.

Abstract: A self-contained abstract outlining in a single paragraph the aims, scope and conclusions of the paper must be supplied.

Keywords: Immediately after the abstract, provide a maximum of six keywords (avoid, for example, 'and', 'of'). Be sparing with abbreviations: only abbreviations firmly established in the field may be eligible.

Symbols: All Greek letters and unusual symbols should be identified by name in the margin, the first time they are used.

Units: Follow internationally accepted rules and conventions: use the international system of units (SI). If other quantities are mentioned, give their equivalent in SI.

Maths: Number consecutively any equations that have to be displayed separately from the text (if referred to explicitly in the text).

References: All publications cited in the text should be presented in a list of references following the text of the manuscript.

Text: Indicate references by number(s) in square brackets in line with the text. The actual authors can be referred to, but the reference number(s) must always be given.

List: Number the references (numbers in square brackets) in the list in the order in which they appear in the text.

Examples:

Reference to a journal publication:

[1] M.S. Mohsen, B.A. Akash, "Evaluation of domestic solar water heating system in Jordan using analytic hierarchy process". Energy Conversion & Management, Vol. 38 (1997) No. 9, 1815-1822.

Reference to a book:

[2] Strunk Jr W, White EB. The elements of style. 3rd ed. New York: Macmillan; 1979.

Reference to a conference proceeding:

[3] B. Akash, S. Odeh, S. Nijmeh, "Modeling of solar-assisted double-tube evaporator heat pump system under local climate conditions". 5th Jordanian International Mechanical Engineering Conference, Amman, Jordan, 2004.

Reference to a chapter in an edited book:

[4] Mettam GR, Adams LB. How to prepare an electronic version of your article. In: Jones BS, Smith RZ, editors. Introduction to the electronic age, New York: E-Publishing Inc; 1999, p. 281-304

Free Online Color : If, together with your accepted article, you submit usable color and black/white figures then the journal will ensure that these figures will appear in color on the journal website electronic version.

Tables: Tables should be numbered consecutively and given suitable captions and each table should begin on a new page. No vertical rules should be used. Tables should not unnecessarily duplicate results presented elsewhere in the manuscript (for example, in graphs). Footnotes to tables should be typed below the table and should be referred to by superscript lowercase letters.

Notification: Authors will be notified of the acceptance of their paper by the editor. The Publisher will also send a notification of receipt of the paper in production.

Copyright: All authors must sign the Transfer of Copyright agreement before the article can be published. This transfer agreement enables Jordan Journal of Mechanical and Industrial Engineering to protect the copyrighted material for the authors, but does not relinquish the authors' proprietary rights. The copyright transfer covers the exclusive rights to reproduce and distribute the article, including reprints, photographic reproductions, microfilm or any other reproductions of similar nature and translations.

Proof Reading: One set of page proofs in MS Word 2010 format will be sent by e-mail to the corresponding author, to be checked for typesetting/editing. The corrections should be returned within **48 hours**. No changes in, or additions to, the accepted (and subsequently edited) manuscript will be allowed at this stage. Proofreading is solely the author's responsibility. Any queries should be answered in full. Please correct factual errors only, or errors introduced by typesetting. Please note that once your paper has been proofed we publish the identical paper online as in print.

Author Benefits:

No page charges: Publication in this journal is free of charge.

Free offprints: One journal issues of which the article appears will be supplied free of charge to the corresponding author and additional offprint for each co-author. Corresponding authors will be given the choice to buy extra offprints before printing of the article.

Preface

The Fifth Global Conference on Renewables and Energy Efficiency for Desert Regions "GCREEDER-V" 2016 is a sequel to successful GCREADER I, GCREEDER II, GCREEDER III and GCREEDER-IV conferences held in Amman, in 2006, 2009, 2011 and 2013. The conference remains faithful to its original idea of providing a platform to discuss renewable energy and energy efficiency issues for desert regions.

The special issue is edited by Mohammad Hamdan, Professor of Mechanical Engineering at the The University of Jordan and his colleague Eng. Eman Abel Hafez- at Al Zaytoonah University of Jordan. We are pleased to see many contributions from various parts of the world, with more than 160 Abstracts were submitted from 25 countries in response to the conference call for papers. About 110 papers were selected for presentation. Selected papers were published in four different international journals among which is the International Journal of Mechanical and Industrial Engineering

The papers reflect the diverse energy issues of interest in developing countries including the need for low cost sustainable solutions to resource constraints particularly energy, water, and environment, These papers include technical issues on various aspects of the conference themes in addition to energy management and policy issues. Selected papers will be published also in a special issue of three peer-reviewed International Journals

The papers showcase research involving laboratory experiments, field trials, simulation, and analysis, and reflect interest in planning, design, construction, operations, and performance of energy systems. The papers range in scope and application. They include the application of recent analysis methods ranging from the application of artificial neural networks to timely problems focus is on novel methods and analysis applied to more traditional infrastructure engineering problems rather than the cross disciplinary papers focused on methodological advances in infrastructure systems.

This special issue also serves another purpose. From the initial proposal for the special issue to the final product, the development of the special issue provided an opportunity to introduce our review processes and procedures to guest editors, authors, and reviewers who we have not historically engaged with. We all have had much to learn from each other as we reviewed, revised, and re-reviewed papers as part of the process. It has been educational for us all. I hope the guest editors, authors, and reviewers have learned something about the rigor of the process. I also hope that this is an initial step in a journey, in which we can share the results of our research and better understand the problems and results that are important to developing countries.

Prof. Mohammad Ahmad Hamdan

Guest Editor

Hashemite University

Zarqa, Jordan

PAGES**PAPERS**

201 - 207

Co-Firing of Petroleum Coke Waste and Kentucky Coal in an Entrained Flow Gasifier*Isam Janajreh , Idowu Adeyemi , Chaouki Ghenai*

209 - 215

Dependency of Forecasting Accuracy for Balancing Power Supply by Weather-Dependent Renewable Energy Sources.*Annika Magdowski , Martin Kaltschmitt*

217– 223

Investigate the Natural Convection Heat Transfer in A PCM Thermal Storage System Using ANSYS/FLUENT*Maier M. Al-Maghalseh*

225– 233

Transevaporative Cooling Performance of a Three-Sided Wind Catcher.*M.N. Khan , I. Janajreh*

235– 243

Modeling and Simulation of Shrouded Horizontal Axis Wind Turbine Using RANS Method*C. Ghenai , T. Salameh , I. Janajreh*

245– 252

Physical and Chemical Analysis of Ultrasonic Transesterification through Numerical Simulation*M. N. Hussain, T. E. Samad, I. Janajreh .*

Co-Firing of Petroleum Coke Waste and Kentucky Coal in an Entrained Flow Gasifier

Isam Janajreh^{a*}, Idowu Adeyemi^a, Chaouki Ghenai^b

^a Mechanical and Materials Engineering Department, Khalifa University of Science and Technology, Masdar Institute, P. O. Box 54224, Abu Dhabi, UAE,

^b Sustainable and Renewable Energy Engineering Department, University of Sharjah, P. O. Box 27272, Sharjah UAE

Abstract

In the present study, a numerical model for the gasification of a mixture of Kentucky Coal and Petroleum Coke inside an oxygen-fed atmospheric Entrained Flow Gasifier (EFG) is developed. Three mixing percentages of petroleum coke (10%, 25% and 50%) are studied. The Kentucky coal was characterized with Thermo-Gravimetric Analyzer (TGA) for the proximate analysis, Flash 2000 for the ultimate analysis and bomb calorimeter (Parr 6100). The model is based on the Lagrangian-Eulerian approach whereby the solid phase particles are tracked with the Lagrangian approach and the surrounding gas phase is tracked by the Eulerian phase. The model takes into account the turbulent flow for the continuous phase (Realizable k- ϵ model), gas phase gasification (Species transport model), devolatilization (Kobayashi two competing rate model), heterogeneous char reaction (Multiple surface reaction model), particle dispersion by turbulent flow (Stochastic discrete random walk model), radiation (P1) and particle distribution (Rosin rammler model). The effect of petcock percentage, wall temperature and the particle size on gas composition and gasification metric has been studied. The present study shows that decreasing the particle size does not lead to the production of more SynGas (CO+H₂). Particle size of 334nm led to the highest SynGas production and lowest exit temperature. Marinating a wall temperature at 1,173 K led to the production of the most SynGas.

© 2017 Jordan Journal of Mechanical and Industrial Engineering. All rights reserved

1. Introduction

Petroleum coke (petcoke) is the byproduct of the refining process. It is characterized with a high heating value and low ash contents. However, it is often difficult to utilize as a stand-alone feedstock because of its low volatile fraction which makes it challenging to ignite additional to its high sulfur contents. It is therefore often blended with coal to compensate the lack of volatility by improve its ignition and reduce its emission. Moreover, petcoke cost offers significant advantages for coal plants as it is quite inexpensive. Although there are various numerical 2-D and 3-D models for the entrained flow gasification of coal particles in the literature [1-4], there is no study which has focused on the numerical modelling of the entrained flow gasification of the mixture of Kentucky coal and Petroleum coke. For example, Hampp [1] developed a 2D model for the gasification of Kentucky coal inside a drop tube reactor (DTR). Chen et al. [2] developed a 3-D simulation model for an air-blown 200 ton/day two-stage entrained flow gasifier, they used numerical methods and sub-models conventionally for pulverized coal combustion. Watanabe *et al.* [3] performed multi-dimensional computational modeling of an entrained flow gasifier for coal gasification with the Langrangian-

Eulerian based approach. Abani and Ghoniem [4] developed a model for a 3-D multiphase reacting flow in a coal fed entrained flow gasifier using Large Eddy Simulation (LES) –with a one-equation eddy viscosity model- and Reynolds-Averaged Navier Stokes (RANS) – that account for gas phase turbulence. Ghenai and Janajreh [5] studied the effect of biomass (wheat straw) addition to bituminous coal on the reactor centerline NO_x and CO₂ concentration. They discovered that the NO_x and CO₂ concentration decreased along the centerline with the addition of wheat straw. The gasification of Kentucky coal and higher volatile woody biomass have been recently carried out by authors under different gasification parameters, i.e., equivalence ratio, pressure and temperature [6]. Additional to the high fidelity simulation, an experimental work was conducted in the air-blown atmospheric DTR experimental facility at the Waste-2-Energy Laboratory at Masdar Institute. The measured centerline temperature, exit gas composition, and SEM images were obtained and used for the model validation and more understanding has been gained in the gasification of these two different feedstock particles. In another work by the present authors, macro algae was used and co-gasified with coal by avoiding the many processes of its lipid extraction and conversion [7]. The gasification done under CO₂ and H₂O moderation following both

* Corresponding author e-mail: ijanajreh@masdar.ac.ae.

equilibrium and high fidelity. The H₂O lead to higher gasification efficiency of nearly eight points compared to CO₂.

Nevertheless, there has been no known study of the numerical modeling of the entrained flow gasification of the mixture of petcoke and coal in the literature. The objective of the present study is to develop a numerical model for the entrained flow gasification of the mixture of petroleum coke and Kentucky coal using the Lagrangian-Eulerian approach. The present work also attempts to optimize the developed model following parametric study of the effect of the petcoke mixture percentage, gasifier's wall temperature and particle size on the gasification of the mixture.

2. Material Characterization

The material characterization of the Kentucky coal was conducted at the Masdar Institute Waste to Energy Laboratory. The Thermo-Gravimetric Analyzer (TGA) and Flash CHNOS-elemental analyzer are used to determine the proximate and ultimate analyses of the Kentucky coal. These were used the basis to determine the characteristics of the Kentucky-coal-petroleum coke mixture. The data for the characterization of the petroleum coke were obtained from the literature [8]. The characterization gives an insight into the composition of feedstock before further analysis. The elemental analysis is necessary to infer the chemical formula of the feedstock, or unit molecular weight, to regulate the stoichiometry of the oxidizer/moderator gases and estimate enthalpy of reaction [9-12]. The proximate analysis help in the proper selection of devolatilization, moisture release and char combustion models. The proximate and ultimate analysis data for the Kentucky coal-petcoke mixture at 10%, 25% and 50% of petcoke are as depicted in Tables 1-2. For the ultimate analysis, samples of the Kentucky coal in tin capsules were placed into an oxidation-reduction reactor of temperature between 900 and 1000 °C. This causes the samples to combust, generating large amount of heat while raising the temperature in the reactor to around 1,800 °C. At this high temperature, all organic and inorganic fractions are converted into elements. These elemental composition are carried to the chromatography column and identified quantitatively via the Thermal Conductivity Detectors (TCD).

Table 1: Ultimate analyses of coal and petroleum coke

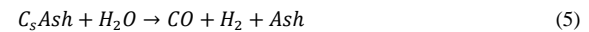
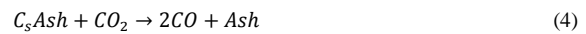
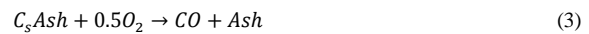
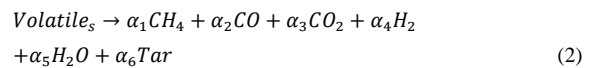
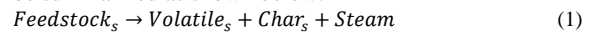
Ultimate (mass %)	Petroleum Coke (10%)	Petroleum Coke (25%)	Petroleum Coke (50%)
C	77.879	79.9775	83.475
H	5.187	5.1075	4.975
N	2.183	1.9775	1.635
O	7.573	6.5275	4.785
S	1.183	1.3675	1.675
A	5.995	5.0425	3.455
Total	100	100	100

Table 2: Proximate analyses and heating value of coal and petroleum coke

Proximate (mass %)	Petroleum Coke (10%)	Petroleum Coke (25%)	Petroleum Coke (50%)
M	2.411	2.0225	1.375
V	37.106	33.395	27.21
FC	54.488	59.54	67.96
A	5.995	5.0425	3.455
Total	100	100	100
LHV (MJ/kg)	30.848	31.49	32.56

3. Model Development

The gasification of the feedstock includes several processes including moisture release, devolatilization, gas phase reactions and char combustion. These processes can be summarized as shown below:



As soon as the feedstock is injected into the gasifier, the moisture is dried out then volatiles is released according to equations 1 and 2. At this stage, several homogenous/volumic reactions take place which follow their own reaction kinetics. Common homogenous coal reactions and their associated kinetics are summarized in Table 3 [13].

Table 3: Kinetic Data for the Homogeneous Reactions

Reaction	Activation Energy (E_a)	Pre-Exponential Factor (A)	Reaction Order (N)
$\text{CH}_4 + \frac{1}{2}\text{O}_2 \rightarrow \text{CO} + 2\text{H}_2$	1.25×10^8	4.4×10^{11}	0
$\text{H}_2 + \frac{1}{2}\text{O}_2 \rightarrow \text{H}_2\text{O}$	1.67×10^8	6.8×10^{15}	-1
$\text{CO} + \frac{1}{2}\text{O}_2 \rightarrow \text{CO}_2$	1.67×10^8	2.24×10^{12}	0
$\text{CH}_4 + \text{H}_2\text{O} \rightarrow \text{CO} + 3\text{H}_2$	1.25×10^8	3×10^8	0
$\text{CO} + \text{H}_2\text{O} \rightarrow \text{CO}_2 + \text{H}_2$	8.37×10^7	2.75×10^9	0

The remaining char then undergoes into a series of heterogeneous/surface gasification reactions (Equations 3-5), namely exothermic char-O₂, the two endothermic char-CO₂ and char-H₂O. They follow 1st order Arrhenius rate as listed in Table 4 [14, 15].

Table 4: Kinetic Data for the Arrhenius heterogeneous reactions

Reaction	Activation Energy, E_a (J/mol)	Pre-Exponential Factor (A)	Reaction Order (n)
$C + \frac{1}{2}O_2 \rightarrow CO$	9.23×10^7	2.3	1
$C + CO_2 \rightarrow 2CO$	1.62×10^8	4.4	1
$C + H_2O \rightarrow CO + H_2$	1.47×10^8	1.33	1

3.1. Modeling Equations

In order to correctly model this phenomenon, mass, momentum, energy and species have to be conserved following the conservation of mass transport equation 6 below:

$$\frac{\partial \rho}{\partial t} + \frac{\partial(\rho v_x)}{\partial t} + \frac{\partial(\rho v_r)}{\partial t} + \frac{\rho v_r}{r} = S_m \quad (6)$$

where ρ is the density and upper case S_m is the source terms due to the dispersed/discrete phase interaction. The transport of density-velocity multiple (ρu_x) and the density-energy multiple (ρE) represent the conservation of momentum and energy, respectively, and these are written in Eqs. 7 and 10 as:

$$\begin{aligned} \frac{\partial(\rho v_x)}{\partial t} + \frac{1}{r} \frac{\partial}{\partial x} (r \rho v_x v_x) + \frac{1}{r} \frac{\partial}{\partial r} (r \rho v_r v_x) = -\frac{\partial p}{\partial x} + \\ \frac{1}{r} \frac{\partial}{\partial x} \left[r \mu \left(2 \frac{\partial v_x}{\partial x} - \frac{2}{3} (\nabla \cdot \vec{v}) \right) \right] \\ + \frac{1}{r} \frac{\partial}{\partial r} \left[r \mu \left(\frac{\partial v_x}{\partial r} + \frac{\partial v_r}{\partial x} \right) \right] + F_x \end{aligned} \quad (7)$$

$$\begin{aligned} \frac{\partial(\rho v_r)}{\partial t} + \frac{1}{r} \frac{\partial}{\partial x} (r \rho v_x v_r) + \frac{1}{r} \frac{\partial}{\partial r} (r \rho v_r v_r) \\ = -\frac{\partial p}{\partial x} + \frac{1}{r} \frac{\partial}{\partial x} \left[r \mu \left(\frac{\partial v_x}{\partial r} + \frac{\partial v_r}{\partial x} \right) \right] \\ + \frac{1}{r} \frac{\partial}{\partial r} \left[r \mu \left(2 \frac{\partial v_r}{\partial r} - \frac{2}{3} (\nabla \cdot \vec{v}) \right) \right] - 2\mu \frac{v_r}{r^2} + \frac{2}{3} \frac{\mu}{r} (\nabla \cdot \vec{v}) + \\ \rho \frac{v_r^2}{r} + F_r \end{aligned} \quad (8)$$

where p is the pressure, μ is the fluid viscosity, and F_x is the present body forces in the form of gravitational force and the divergence of the velocity is expressed as:

$$(\nabla \cdot \vec{v}) = \frac{\partial v_x}{\partial x} + \frac{\partial v_r}{\partial r} + \frac{v_r}{r} \quad (9)$$

$$\begin{aligned} \frac{\partial(\rho E)}{\partial t} + \nabla \cdot (\vec{v}(\rho E + p)) = \nabla \cdot (k_{eff} \nabla T - \sum_j h_j \vec{j}_j + \\ (\vec{\tau}_{eff} \cdot \vec{v})) + S_h \end{aligned} \quad (10)$$

$$E = h - \frac{p}{\rho} + \frac{v^2}{2} \quad (11)$$

$$h = \sum_j Y_j h_j \quad (12)$$

where E is the internal energy, K_{eff} is the effective conductivity, h is the enthalpy and Y_i is the mass fraction. S_h is any external energy source that is unaccounted for.

The conservation of species of the flow is also written according to eq. 13 as:

$$\frac{\partial(\rho Y_i)}{\partial t} + \nabla \cdot (\rho \vec{v} Y_i) = -\nabla \cdot \vec{j}_i + R_i + S_i \quad (13)$$

where S_i is the sources term other than reaction and R_i is the addition or the destruction of the species due to the reaction and is expressed as:

$$R_{j,r} = R_{kin,r} \left(p_n - \frac{R_{j,r}}{D_{0,r}} \right)^N \quad (14)$$

where $R_{kin,r}$ is the Arrhenius reaction rate written as:

$$R_{kin,r} = A_r T_p^{\beta r} e^{-(E_r/RT_p)} \quad (15)$$

$D_{0,r}$ is the effective surface area which is function of the localized temperature and particle diameter and is written as:

$$D_{0,r} = C_{1,r} \frac{[(T_p + T_\infty)/2]^{0.75}}{d_p} \quad (16)$$

The discrete Phase Model Equations that governs the Lagrangian solid particles are expressed as:

$$\frac{du_p}{dt} = F_D(u - u_p) + \frac{g_x(\rho_p - \rho)}{\rho_p} + F_x \quad (17)$$

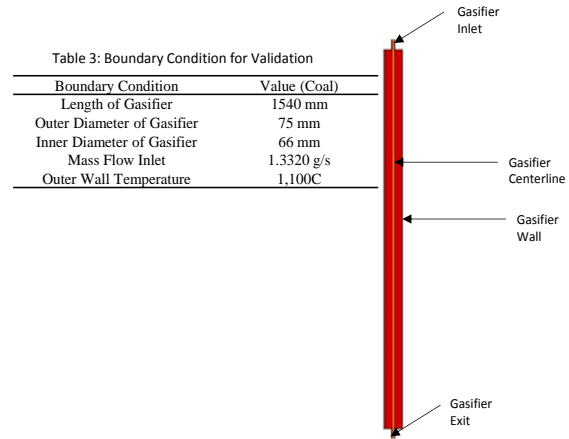
$$F_D = \frac{18\mu}{\rho_p d_p^2} \frac{C_D Re}{24} \quad (18)$$

$$Re = \frac{\rho d_p |u_p - u|}{\mu} \quad (19)$$

where $F_D(u - u_p)$ is the drag force per unit particle mass; u is the fluid phase velocity; u_p is the particle velocity; and ρ is the fluid density, and ρ_p is the density of the particle. Equation (17) incorporates additional forces (F) in the particle force balance that can be important (i.e., thermophoretic and Brownian forces).

3.2. Model Setup and Boundary Conditions

The geometry and baseline mesh of the laboratory scale gasifier is depicted in Fig. 1 and detailed dimension and boundary conditions are summarized in Tables 3-4. This geometry matches the DTR which developed by the author group. It consisted of temperature controlled cylindrical tube of 154 cm length x 6.6 cm diameter and equipped with accurate dosing system. The DTR can be utilized to simulate the desired gasification environment.

**Fig. 1:** Geometry and baseline mesh setup**Table 4:** Boundary Condition for the Reactive Flow

Condition	Mix Pet 10%	Mix Pet 25%	Mix Pet 50%
O2 Inlet (g/s)	0.316	0.324	0.337
Particle Feed Rate (g/s)	0.234		
Wall Temp. (K)	1073-1273		
Equivalence Ratio	1.8		

3.3. Numerical Solution Approach

The numerical model of the gasification processes in an entrained flow gasifier was carried out within Ansys Fluent environment. As depicted in Fig. 2, the model uses Eulerian approach to solve the conservation of mass, species, momentum and energy for the continuous gas phase while uses the Lagrangian approach to discretize the feedstock particles to obtain their position, velocity and temperature. The particle-source-in cell approach was then used to couple the Eulerian and the Lagrangian approaches. Coupling of momentum, heat, and mass transfer between the solid and gas phases is accounted for by the two-way coupling Cloud model, in which Lagrangian-based particle trajectory is tracked as a cloud of particles about a mean trajectory. The mean trajectory is then calculated by solving the ensemble-averaged equations of motion for all particles represented by the cloud. The i^{th} species production/destruction due to the reaction r follows the eddy dissipation concept model used in other combustion/reaction flow work [14]. It uses the limited rate of either the instantaneous eddy-dissipation model that assumes the chemical reaction proceeds as the reactants meet and is faster than the time scale of the turbulence eddies or the Finite Arrhenius Rate model. The remaining solid char particle goes into the three gasification reactions as was detailed in Table 4.

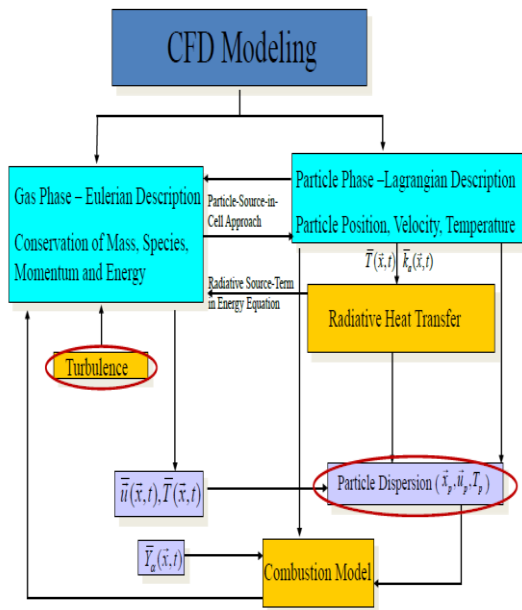


Fig. 2: Numerical solution approach for gasification [10]

4. Results and Discussions

4.1. Model Validation

The validity of the results of the model are tested against the experimental data of the drop tube reactor

(DTR) at Masdar Institute Facilities. This DTR is instrumented with a calibrated dosing system, wall heat flux, and spatially distributed centerline and wall positioned thermocouples. It simulates the actual environment of the gasification within 120-150cm free entraining feedstock particles. The more the model results agree with the experimental values, the further fidelity in the model. Fig. 3 depicts the model results of the centerline temperature distribution and those measured experimentally for reactive flow using only coal as feedstock. The model results predict the experimental values reasonably well as seen in Fig. 3 [14].

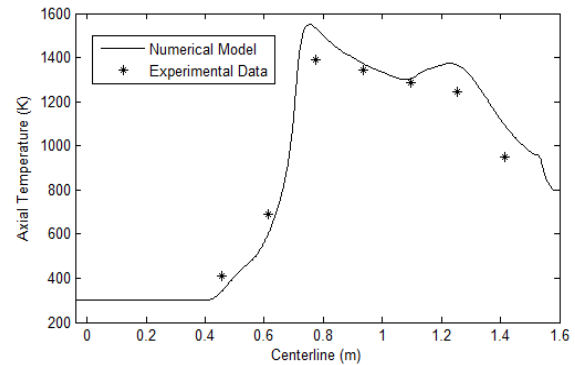


Fig. 3: Axial Temperature Validation with Experimental Data for Reactive Flow

4.2. Coal and Petcoke Co-Gasification

As indicated, co-firing petcoke with coal offers dual advantages, refinery waste management and economical gain. The entrained flow gasifier accommodates fuel flexibility by allowing wider feedstock usage. For instance, an IGCC plant can utilize a combination of high coal quality and lower quality feedstock, like lignite, biomass, and even treated municipal solid waste for power generation. Fig. 4 depicts the temperature contour and the mole fraction of the volatile as well as the O_2 in the gasifier. The high temperature is delayed until the release of the moisture and volatile release, because these reactions are endothermic and despite the oxygen presence the partial combustion is insufficient to maximize the temperature near the top entry zone. As soon as a higher temperature is attained that triggered by the partial combustion, more volatile is released that simultaneously consumes the available O_2 . This zone is coinciding with the highest DTR temperature which is somewhat located downstream the entry. The release of the volatile coincides with the exothermic volatile combustion which leads to the increase in the temperature around this region. The O_2 fraction is quickly reduced along the gasifier and reaches zero mole fraction also slightly downstream the top entry region. The reduction and the potential gas shift starts downstream along the reactor to normalize the production of syngas until the exit.

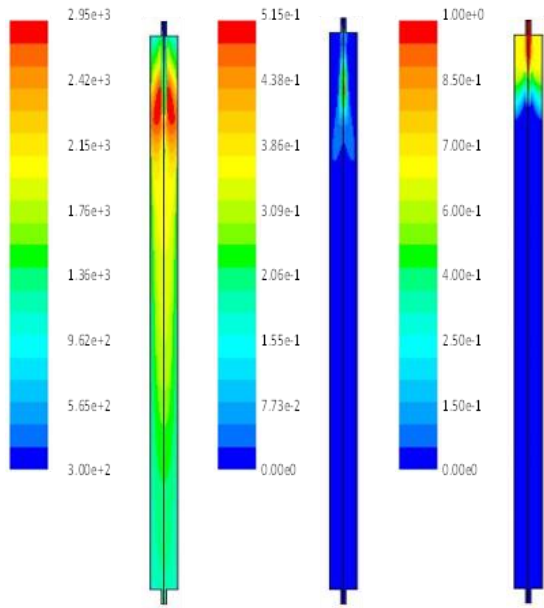


Fig. 4: (a) Temperature Contour (K), Left (b) Mole Fraction of Volatile, Middle (c) Mole Fraction of O₂, Right

Fig. 5 shows the contour of the mole fraction of the CO₂ and CO along the DTR/gasifier. Due to the volatile combustion, the CO₂ mole fraction was observed to increase along the gasifier and then decreased due to its reduction in the char-CO₂ equation according to equation 4. Consequently, this leads to the production of more CO downstream the DTR at the cost of reduction in temperature as was observed in the temperature distribution Fig. 4.

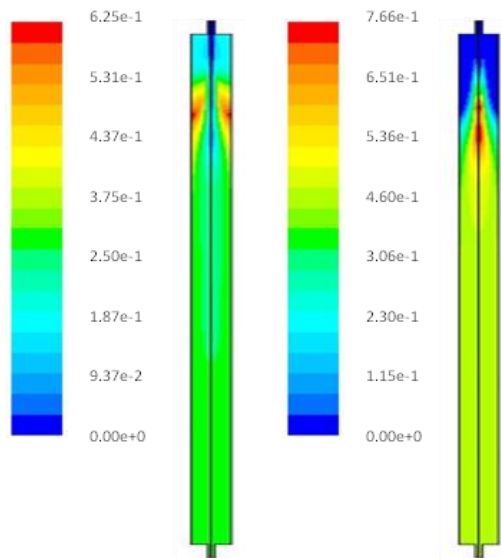


Fig. 5: (a) Mole Fraction of CO₂, Left (b) Mole Fraction of CO, Right

Fig. 6 shows the contour of the mole fraction of the H₂O and H₂ along the gasifier. Due to the volatile combustion, the H₂O mole fraction was observed to increase along the gasifier and then decreased. The first increase due to combustion and its H₂O yield, while the

decrease is attributed to the char-H₂O reaction per equation 5. Consequently, this leads to the production of more H₂ as flow goes down the drop tube and at the cost of reduction in the temperature as shown in Fig. 4.

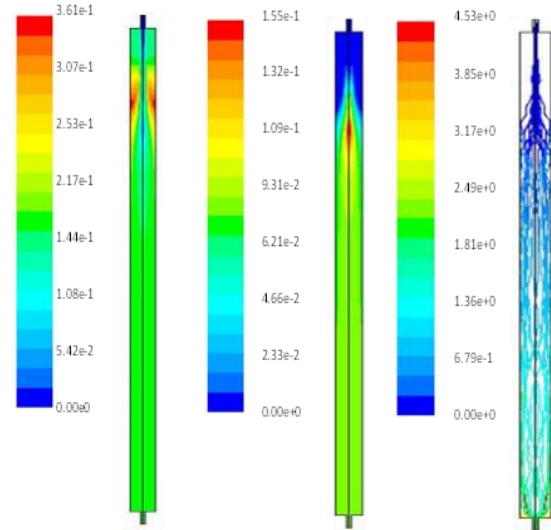


Fig. 6: (a) Mole Fraction of H₂O, Left (b) Mole Fraction of H₂, Middle (c) Particle Residence time (s)

4.3. Effect of Petroleum Coke Composition on Gasification

The effect of petroleum coke composition in the mixture of petroleum and Kentucky coal was studied in order to determine the optimum amount of petroleum coke to be used. It was observed that the syngas (CO+H₂) molar fraction is increased as the amount of petroleum coke in the mixture is increased. This is reasonable because at 50% mixture the amount of fixed carbon is the highest. Larger fixed carbon fraction implies more char reduction and as long as the temperature remains relatively high to do so more syngas production is expected. These results are presented in Fig. 7 and it follows the reactions described in equations 3-5.

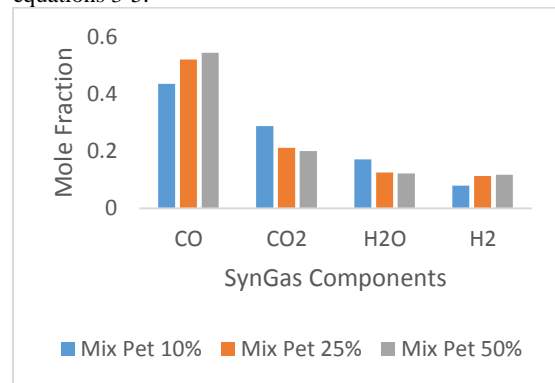


Fig. 7: Mole Fraction of SynGas for the three Mixing Ratios

The exit DTR temperature is accordingly decreased as one injects more petcoke in the mixture. The decrease in exit temperature is due to the high endothermic reaction of the fixed carbon reduction. The exit DTR temperature under different Petcoke/Coal mixing ratio is depicted in Fig. 8.

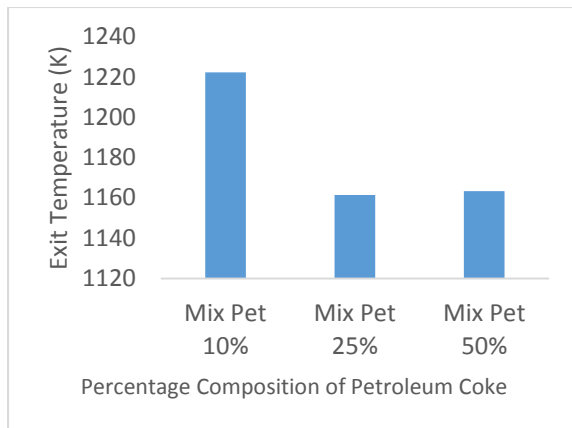


Fig. 8: Exit Temperature for the three Mixing Ratios

The residence time is also evaluated as longer residence time is inversely proportional to the gasifier throughput/capacity and also is a cost metric one needs to consider. In general one desires to use shorter gasifier which attains complete conversion and appropriate syngas production. Longer residence time is obtained at 50% mixture. One reason is the low density of the petroleum coke which was decreased when 50% petroleum coke is utilized as depicted in Fig. 9.

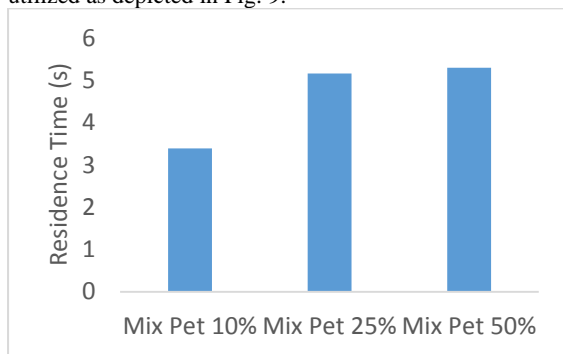


Fig. 9: Residence time for the three Mixing Ratios

4.4. Effect of Particle Size on Gasification

The effect of particle size (134nm, 334nm and 534nm) on the gasification mixture of 25% petroleum coke and -75% Kentucky coal was studied. It was generally observed that as the particle size increases, the yield of syngas (CO and H₂) decreases as depicted in Fig. 10. This is reasonable because smaller particle sizes give high surface area for reaction, thereby faster and more complete reaction as compared to larger particles. However, a new phenomenon was observed between 134 and 334 nm particle size. The syngas composition actually increases as the particle size increased from 134 nm to 334 nm. This may be attributed to other phenomena, such as quick volatile release and the combustion of smaller particle. The general trend, however, was confirmed at larger particle size of 543nm. The particle size of 334 nm gave the optimum syngas production.

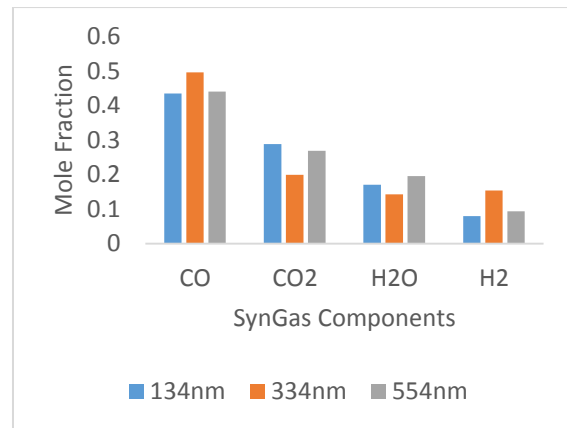


Fig. 10: Mole Fraction of SynGas for the three Particle Sizes

The temperature at the exit of the gasifier was observed to be the also lowest for 334 nm. This is favorable for gasification because the syngas has to be cooled down typically for post cleaning where a lower the exit temperature, the better the process metrics it becomes (Fig. 11).

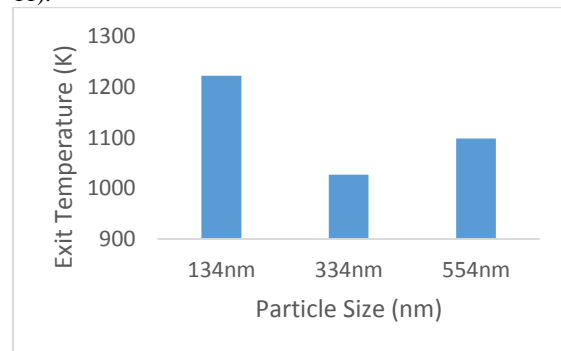


Fig. 11: Exit Temperature of SynGas for the three Particle Sizes

4.5. Effect of Wall Temperature on Gasification

The effect of wall temperature shows that the mole fraction of the syngas (CO+H₂) increases as the wall temperature is increased. The increase in wall temperature leads to a faster and better endothermic char gasification. The mole fraction of the syngas increased more sharply when the wall temperature is increased from 1,073 K to 1,173 K, but more gradual from 1,173 K to 1,273 K wall temperature. This shows that a temperature of 1,173 is the most suitable for the mixture of petroleum coke and Kentucky coal as presented in Fig. 12.

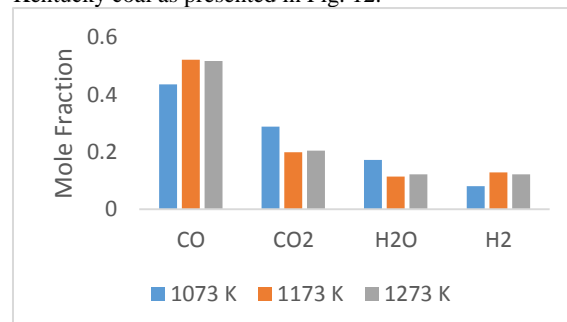


Fig. 12: Mole Fraction of SynGas for the three Wall Temperatures

5. Conclusions and Future Work

A comprehensive, predictive kinetics-based CFD model for the co-gasification of coal and petcoke has been investigated. The oxygen-blown atmospheric drop tube facility at Masdar Institute was used for as baseline for this setup. It was shown that the increases of Petcoke percentage leads to the production of more SynGas (CO+H₂). Decreasing the Particle size does not necessarily lead to the production of more SynGas (CO+H₂). Particle size of 334nm led to the highest SynGas production and lowest exit temperature. Wall temperature of 1,173 K led to the production of the most SynGas. The trend can be verified by examining more feedstock to observe the flexibility of the gasification system and specific adjustment for a particular fuel. Another research path the present work may take is the development of a detailed chemical mechanism for the gasification of feedstock and obtaining more data for the volatile composition during pyrolysis.

Acknowledgments

The support from Masdar Institute, the Waste to Energy group, and the MEG603-2015 class is highly acknowledged. Thanks also are due to Jennah Alonso for helping in preparation of the manuscript.

References

- [1] Hampp F., "Development of experimental and numerical tools to investigate the thermochemical conversion of solid feedstock", Master's Thesis Dissertation, (2011) Masdar Institute.
- [2] Chen, C., Horio, M., & Kojima, T., "Numerical simulation of entrained flow coal gasifiers. Part I: modeling of coal gasification in an entrained flow gasifier. Chemical Engineering Science", Vol.55 (2000) No. 18, 3861-3874.
- [3] Watanabe, H., & Otaka, M., "Numerical simulation of coal gasification in entrained flow coal gasifier", Fuel, Vol. 85 (2006) No. 12, 1935-1943.
- [4] Abani, N., & Ghoniem, A. F., "Large eddy simulations of coal gasification in an entrained flow gasifier", Fuel, Vol. 104 (2013) No. 31, 664-680.
- [5] Ghenai, C., Janajreh, I., "CFD analysis of the effects of co-firing biomass with coal", Energy Conversion and Management, Vol. 51 (2010) No.8, 1694-1701.
- [6] I. Adeyemi, I. Janajreh, T. Arink, C. Ghenai, "Gasification behavior of coal and woody biomass: Validation and parametrical study", Applied Energy 185 (2017) 1007-1018
- [7] I. Janajreh, S. S. Raza, S. Elagroudy, "Co-Firing of Enteromorpha Prolifera Algae and RTC Coal in a Down Draft Gasifier: Material Characterization and Flow Simulation", J. Solid Waste Technology annd Management, Vo. 41, No. 1 (2015) 68-87.
- [8] U.S. Environmental Protection Agency, Screening-Level Hazard Characterization, Petroleum Coke Category, June 2011; and H.W. Nelson, Petroleum Coke Handling Problems, 1970.
- [9] H. Chris, and M. van der Burgt, "Gasification", Amsterdam, Boston: Gulf Professional Pub., 2003. ISBN: 0750677074
- [10] Y. Yun, Y. Don Yoo, and S. Woo Chung, "Selection of IGCC candidate coals by pilot-scale gasifier operation", Fuel Processing Technology, Vol. 88, (2007), 107-116
- [11] M. J. Prins, K. J. Ptasinski, and F. J.J. G. Janssen, "From coal to biomass gasification: Comparison of thermodynamic efficiency", Energy, Vol. 32, (2007), 1248-1259.
- [12] Dhanaplan S, Annamalai K, Daripa P. Turbulent combustion modeling coal: biosolids blends in a swirl burner. Energy week, vol. IV. ETCE, ASME; (1997), 415-23.
- [13] Ajay V. Kolhe, Rajesh E. Shelke, S. S. Khandare, "Combustion Modeling with CFD in Direct Injection CI Engine Fuelled with Biodiesel", JJMIE, Vol. 9 (2015) No. 1, 61- 66

Dependency of Forecasting Accuracy for Balancing Power Supply by Weather-Dependent Renewable Energy Sources

Annika Magdowski ^a, Martin Kaltschmitt ^b

^a *Hamburg University of Technology (TUHH), Institute of Environmental Technology and Energy Economics (IUE), Eissendorfer Strasse 40, 21073 Hamburg, Germany, E-mail: magdowski@tuhh.de*

^b *Hamburg University of Technology (TUHH), Institute of Environmental Technology and Energy*

Abstract

The share of renewable energies in the national electricity generation systems is increasing worldwide, recently especially weather-dependent wind and solar power plays a substantial role. These energy sources are characterized by a fluctuating and imprecise predictable power generation, which increase the need of flexibilities within the remaining electricity systems (e.g., conventional power plants) to guarantee a high security of supply. Nowadays, these flexibilities are primarily provided by power plants based on fossil fuel energy. In future, these conventional power plants will increasingly be displaced by an increasing renewable power supply. Thus, also weather-dependent renewable energy systems like windmills and PV systems need to contribute to the provision of balancing energy. Therefore, the aim of this paper is to analyse technical and energy economic conditions allowing weather-dependent renewable energy sources to contribute in markets for balancing energy and to estimate the scale of this contribution in a given energy system. As a basis, the day-ahead forecasting quality of the feed-in from wind park systems in Germany is analysed, to estimate the share of the wind power generation, which can be safely predicted for the following day. Based on probabilistic methods and the investigated results the theoretical potential of balancing energy delivered by wind mill systems can be calculated for a given supply area as well as for a defined degree of the security of electricity supply.

© 2017 Jordan Journal of Mechanical and Industrial Engineering. All rights reserved

Keywords: *wind energy, prognosis accuracy, balancing power.*

1. Introduction

The share of renewable energies is increasing worldwide; in 2014, more than 23 % of the global electricity production was produced by these sustainable energy sources [1]. This development is expected to continue in the future, because at least 144 countries around the world have implemented expansion targets for renewable energies [1]. Especially, the weather-dependent electricity generation from windmills and PV power plants play a substantial role within this renewable energy mix. However, their integration in electricity networks causes advanced system requirements due to their fluctuating and imprecise predictable power generation. Additionally, their feed-in prognosis and its reliability contribute to scheduling the generation of conventional power plants. These typically fossil fuel driven power plants guarantee a sufficient energy generation and a satisfactory provision of balancing energy to compensate forecast errors and high feed-in gradients of the renewable power supply. In future, with an increased share of wind and solar power supply, these conventional power plants will be increasingly displaced and thus weather-dependent renewable energy systems need to contribute to the secure provision of balancing energy. But so far, due to the current market

regulations in Germany, these renewable energy systems do not make any contribution to the stability of the electric power system. The balancing power is mainly supplied by conventional power plants and pumped-storage hydro power stations. As a conclusion, even in the hours of high feed-in from wind and solar systems, conventional power plants must remain in the network in order to provide the necessary control power.

Against this background, the aim of the present paper is to analyse technical and energy economic conditions allowing weather-dependent renewable energy sources to contribute in markets for balancing energy. Subsequently, the scale of this contribution within a given energy system should be estimated. For an estimation of the capability of windmills and solar systems to provide balancing energy, the most limiting factor is their imprecise predictable power output. Therefore, the present paper gives an overview of the day-ahead forecasting quality of the feed-in from wind systems in Germany, to show which various constraints affect the forecast accuracy so far. Based on probabilistic methods, the share of the wind power generation, which can be predicted for the following day with a high probability, is estimated. Subsequently, the theoretical potential of balancing energy delivered by wind systems can be calculated for a given supply area as well as for a defined security of electricity supply. The results

allow an evaluation of the impact of weather-dependent power supply on the electricity system balance, both for current and future time horizons.

The methodology explained above will be applied to wind energy systems and it is related to the German electricity network. Nevertheless, the methodology can be transferred to other electricity supply systems with, for example, different generation portfolios, other geographical conditions or varying levels of security of supply.

To provide positive control power, wind turbines have to operate on a throttled power level. This mode causes energetic and thus financial losses through the reduced power output, especially under consideration of forecasting inaccuracies and required reliabilities for balancing energy supply. Therefore, the present paper only assesses the potential of negative balancing energy provided by wind turbines.

2. 2. Methodology and Database

First, the forecasting accuracy of wind power has to be assessed to subsequently estimate the balancing energy potential by wind turbines. This is discussed below.

2.1. Assessment of Forecasting Accuracy

The day-ahead power forecasting is delivered by current regulations at 8 am for every quarter of an hour for the entire following day [2]. This yields to a forecast horizon from 16 to 40 h. This short-term forecasting is based on meteorological parameters predicted by numerical weather models, which are associated with the regionally distributed installed wind capacity and its measured feed-in. Deductive, the selection of the weather prediction model, and, thus, its regional and timely resolution, objective and adaptation to specific local conditions has a significant impact on the prognosis quality [3].

2.1.1. Mathematical Description

The forecast error X is the difference between the predicted value for the wind electricity generation to be feed into the grid Pr and the actual wind feed-in I ($X = Pr - I$). Positive forecast errors reflect an overestimation, negative an underestimation of the electricity supply from wind power. The prediction accuracy is characterized by the following parameters.

Arithmetic mean M . This value represents the systematic error of the power prediction, which identifies an average over- or underestimation of the wind supply.

Maximum and minimum forecast errors X_{min}/X_{max} . These parameters provide a first impression of the prediction accuracy. But they refer just to a singular event. Therefore, they have only limited significance [3].

Root Mean Square Error RMSE. The RMSE indicates the scattering of the forecast error. Thus, this is an appropriate parameter for the assessment of power estimations. Due to the quadratic approach, larger errors are weighted with more significance and thus the economic impact on the electricity system is approximated in more detail [3].

Empirical probability distribution f . The distribution of the occurrence of forecast errors can be expressed by probability density functions. Discrete frequency distributions are converted in a continuous function using a kernel density estimation, e.g., with a Gaussian core [4]. The probability P that errors X only occur between the interval boundaries a and b can be calculated with a probability density function f according equation (1). In the same way, interval limits for defined probabilities can be determined. Thus, the previously described parameters can be specified for various confidence intervals:

$$P(X \in [a, b]) = \int_a^b f(X) dX \quad (1)$$

2.1.2. Scaling Factors for a Comparable Evaluation

A normalization of forecast errors allows a better comparability of the parameters described above for different boundary conditions. The applied scaling factors are listed below. Compared to previous studies (e.g., [5–7]) using mostly constant scaling factors, in the present paper variable time and yield dependent reference values have been selected.

Installed capacity of the generating plants P_{inst} . This reference creates comparable conditions within different years and investigation area despite expansion of renewable energies.

Predicted wind feed-in Pr_{wind} . The normalization to the predicted feed-in, being variable in time, enables a comparability of errors at different yield levels. Thus, the effect of higher absolute errors during periods with a high feed-in can be eliminated.

2.1.3. Time Dependence of Prediction Accuracy

The prediction accuracy of the wind power supply is evaluated with characteristics described above, but with a special focus on its time dependence. To evaluate the influence of the increasing forecast horizon, all data have been ranged according to their forecast horizon from 16 to 40 h and normalized to the predicted wind feed-in. Consequently, the results represent constraints, which significantly affect the prediction accuracy and identify development potential in meteorological, respectively, power forecasting models. Furthermore, the forecasting accuracy can be quantified in more detail, as a function of forecast horizon and predicted wind supply.

2.1.4. Reliability of the Prediction

Based on the cumulative probability distribution of the error, the "safe" predictable feed-in is determined for defined reliabilities. "Safe" in this respect describes power available with a certain (high) probability. Therefore, positive errors should be avoided, because by convention these errors cause an overestimation of the supply. The reliable forecast Pr_{safe} results from the expected feed-in I under a certain reliability S normalised to the current predicted feed-in Pr (equation (2)):

$$Pr_{safe}(S) = \frac{I(S)}{Pr} \quad (2)$$

Fig. 1 shows on the basis of an exemplary distribution that negative errors occur with a probability $P(X \in [-\infty, 0]) = P(X \leq 0) = 60\%$ and therefore positive error can be excluded with the same probability. A normalization to the predicted feed-in exemplify ranges on the abscissa $X \leq -100\%$ and $X \geq 100\%$, in which errors

are larger than the forecasted feed-in. With the objective of avoiding positive errors, above the limit $X = 100\%$ no share of the prognosis may be considered as safe. With a reliability $= P(X \leq 0) = 60\%$, an overestimation of predicted feed-in can be avoided and thus at least 100% of the predicted feed-in can be considered as "safe" under this level of reliability (equation (3)):

$$P(X \leq 0) = 60\% \rightarrow X = \frac{Pr - I}{Pr} \leq 0 \rightarrow I \geq Pr \rightarrow Pr_{\text{safe}} = \frac{\geq Pr}{Pr} \geq 1 \quad (3)$$

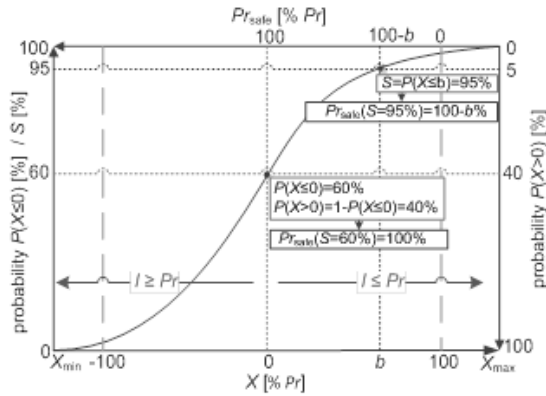


Figure 1: Methodology for estimating the safe predictable feed-in (X : forecast error; Pr_{safe} : safe prognosis; Pr : predicted wind feed-in; S : reliability).

To increase this reliability, S more errors – also negatives – has to be excluded. If $S = 95\%$, all errors $X \in [-\infty, b] = X \leq b$ are included in the forecast with $P = 95\%$ and the safe share of the forecast reduces dependent on the probability distribution of the error (equation (4)):

$$P(X \leq b) = 95\% \rightarrow X \leq b \rightarrow I \geq Pr(1 - b) \rightarrow Pr_{\text{safe}} = \frac{\geq Pr(1-b)}{Pr} = 1 - b \quad (4)$$

This reliability of the forecasting accuracy represents similarly the required security of the balancing energy provision. Therefore, this analysed "safe" predictable part of the forecast is a precondition for the estimation of the negative balancing energy potential.

For the assessment of the forecasting accuracy day-ahead forecast errors of the wind power feed-in in Germany for every quarter of an hour from 2010 to 2015 have been analysed [2], [8], [9], [10]. The installed capacity, as one of the reference values, has been calculated using the Renewable Energy Law database [11].

2.2. Assessment of Balancing Energy Potential

To participate in the balancing power market, actors must provide offers with a defined product length and handling time. Depending on this submission date, respective forecast errors and its prognosis reliability have to be considered for determining the wind power supply and thus the control power potential. Consequently, balancing energy potential of wind turbines is mainly dependent from the following two factors.

- **Yield-dependent influences** like meteorological conditions, installed capacity of the generation portfolio, and regional distribution of wind turbines.

- **Market-regulating factors** like length of the control power products, submission date of the control power bid, and reliability of the balancing energy provision.

The German electricity system distinguishes primary, secondary and tertiary reserve, according to the engaging speed and the capacity of the control power [12]. Due to currently valid regulations for the German balancing energy market (e.g., weekly submissions, product lengths of at least 8 h, and a required reliability of 99%), the market access for supply dependent renewable electricity generation from wind mills or PV systems is almost impossible [4], [13], [14]. Therefore, the control power potential is determined independent of the currently valid tender periods and product lengths of balancing energy offers and will be assessed according to the following factors:

- Dependency on different reliabilities of the forecast, respectively, balancing energy provision;
- dependency on different product length of balancing energy bids;
- dependency on regional resolution of wind parks; and
- dependency on size of wind parks.

The upper aspects represent market-regulating factors, the lower yield-dependent influences. The assessment follows the summarized methodology:

1. Determination of the feed-in by wind turbines on the basis of meteorological data [15] and regional distributed installed capacity [11]. The feed-in has been calculated for different regions in Germany, and various sized wind parks within the years 2012 to 2014.
2. Adjustment of (1) concerning the date of submission of the control power bid through consideration of the forecasting inaccuracy with particular reliabilities (within the following analysis only a day-ahead bidding is analysed; the day-ahead prognosis is integrated using results from the previous assessment (section 3)).
3. Adjustment of (2) concerning different product lengths of control power bids (within the following analysis product lengths of 1, 4, 12, and 24 h will be considered).

A comparison between calculated control power potential and need of control power in Germany shows to what extent wind power, despite fluctuating feed-in, can contribute to the system stability.

3. Assessment of Forecasting Accuracy

The development of the predictive quality of the German wide wind power supply in recent years is shown in Fig. 2. Maximum errors of the wind feed could be reduced despite increasing installed plant capacity. Comparably, forecasting accuracy of wind feed-in improves up to 18% between 2010 and 2015. Also in the years 2007 to 2010, the accuracy increased [5]. Fig. 2 also shows that the mean of the forecast errors are predominantly positive. This means that the average wind supply is overestimated, which increases the need of positive balancing energy demand within the system.

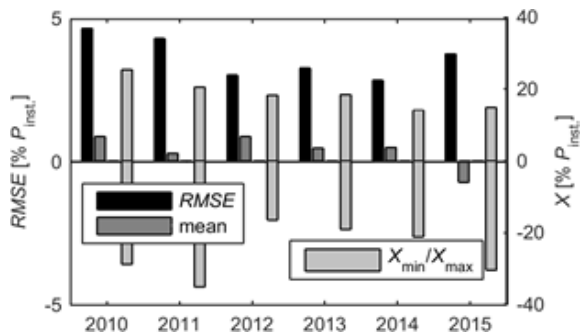


Figure 2: *RMSE*, arithmetic mean and maximum values of the forecast errors of wind power supply in Germany (X : forecast error; Pr_{safe} : safe prognosis; P_{inst} : installed wind capacity).

3.1. Time Dependence on Forecast Horizon

Fig. 3 shows the *RMSE* of the wind forecast errors, normalized to the predicted wind power, as a function of the forecast horizon. As expected, the quality decreases with increasing time horizon. The average forecast errors rise significantly in the range between 6 to 10 o'clock. From a forecast horizon of 26 h the forecast accuracy remains almost constant. Between different times of the day, the average forecasting quality differs up to 25 %.

Additionally, Fig. 3 shows the improvement of the prognosis accuracy in recent years. This reflects the development of the predictive quality shown in Fig. 2.

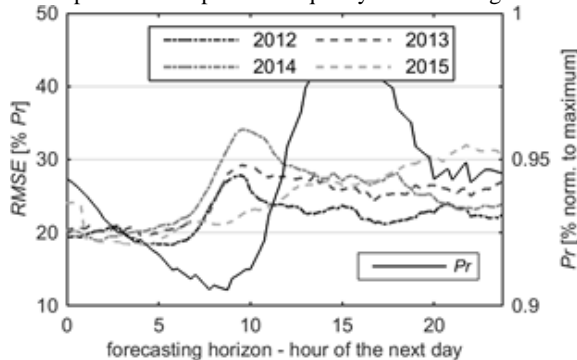


Figure 3: *RMSE* of the prognosis of the wind power feed-in and averaged predicted feed-in as a function of the forecast horizon (Pr : predicted wind feed-in).

To further differentiate whether the worse prognosis quality in the morning of the following day primary depends on the increasing forecast horizon or on feed-in volumes, the correlation between predicted power volume and forecasting accuracy has been investigated. Therefore, the data have been ranked in terms of their predicted feed-in volume and divided into three equal parts, summarizing small, medium and high forecast values [6]. The results shown in Table 1 indicate that the prediction accuracy significantly depends on the predicted feed-in volume. In details, it improves with higher predicted wind power volume; although absolute errors in the upper volume are almost three times higher and thus require a larger demand of the energy balance. Therefore, it can be concluded that

the worse forecast quality in the morning hours of the following day can be predominantly justified by decreasing quality of the forecasting methods with increasing forecast horizon and by relatively small feed-in volumes during this time.

Table 1: Boundary limits and forecasting accuracy of categories with small, medium and high predicted feed-in values.

	small volumes	medium volumes	high volumes
boundary limits [% installed capacity P_{inst}]	0,7 – 6,8	6,8 – 15,6	15,6 – 92,7
<i>RMSE</i> [% predicted feed-in Pr]	38,4	24,4	16,2

Summing up the analysis shows that the predictive accuracy of the day-ahead supply of wind energy systems significantly depends on the forecast horizon as well as on the amount of the predicted feed-in. Therefore, for the following analysis the forecasting accuracy will be considered in different levels of detail:

1. Constant over the entire forecasting horizon;
2. variable in the prediction horizon; and
3. variable in the prediction horizon and amount of predicted feed-in.

3.2. Reliable Day-Ahead Prediction

The assessment of "safe" predictable feed-in is a precondition for the estimation of the balancing energy potential. Applying distribution functions of forecast errors, the share of the day-ahead wind forecast, which can be predicted with certain reliability, can be calculated (section 2.1.4). This share has been calculated using forecast accuracies with different levels of detail (section 3.1). Table 2 shows these safe shares of predictable day-ahead wind feed-in, averaged over the investigation period (2012 to 2014), for reliabilities from 90 to 99.99 %. For instance, using forecast errors subdivided in their forecasting horizon and the particular predicted feed-in volume, up to 58 % higher shares can be reliable predicted for the following day. This tendency increases with increasing reliability of the forecast. As an example, Fig. 4 shows the respective "safe" prediction for reliabilities of 90.00 and 99.99 % differentiated in forecast horizon and in different predicted feed-in volumes. The decrease of the "safe" day-ahead prediction with increasing forecasting horizon and with smaller feed-in volumes is obvious.

For an assessment of the reliable day-ahead wind energy prediction, the application of forecast accuracies variable in forecast horizon and predicted feed-in volume enables to guarantee higher shares of wind energy supply. Consequently, for the following assessment of the balancing energy potential by wind turbines, the high level of detail of the forecast accuracy is maintained.

Table 2: Safe predictable day-ahead wind power feed-in [% of the predicted feed-in volume Pr] for forecast accuracies according method (a), (b), and (c) and different reliabilities.

reliability S	(a) constant over the entire forecasting horizon	(b) variable in prediction horizon	(c) variable in horizon and amount of predicted feed-in
[%]	[%]	[%]	[%]
90,00	63	63	69
95,00	52	52	61
99,00	33	35	46
99,90	19	20	30
99,99	10	10	23

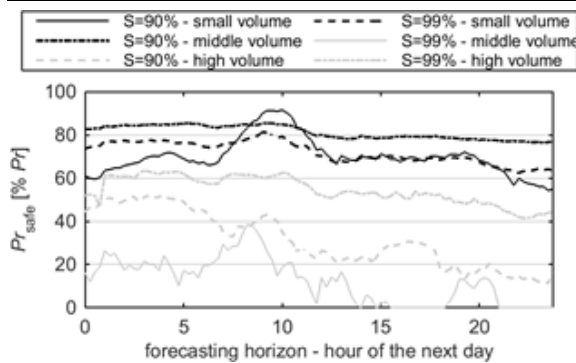


Figure 4: Safe predictable day-ahead wind power feed-in in % of the predicted feed-in. (Pr_{safe} : safe prognosis, Pr : predicted wind feed-in).

4. Assessment of Balancing Energy Potential

From a technical perspective, modern wind turbines can comply with the requirements of balancing markets [4], [16]. The prerequisite for this is a variable speed drive with simultaneous use of the pitch control concept. A model of the control concepts of a modern wind turbine shows that in a restricted operation a significant increase respectively decrease in power output can be realized within a maximum of 30 s [16], [17], and [18]. Irrespective of this technical operation scheme, meteorological conditions are a core requirement for the supply of wind-dependent balancing energy. Based on the methodology described in section 2.2, the balancing energy potential is estimated for the following dependencies.

4.1. Dependency on Different Reliabilities of the Prediction

Fig. 5 (left column in each section) shows the theoretical balancing energy potential (product length 4 h, normalized to the installed wind power) for a wind park pool with an installed capacity of 1 GW under average meteorological conditions (wind speed at 3.6 m/s in a height of 10 m) and without consideration of wind power forecast errors. The other columns represent the decrease of balancing energy potential under consideration of forecasting errors and their particular forecast, respectively, supply reliability between 90 and 99.99 %. The several sections reflect the different levels of detail to

quantify the forecasting accuracy (section 3.2). With increasing level of reliability, decreasing shares of the wind power can be securely predicted and thus the control power potential decreases significantly. This tendency is more distinctive for forecast accuracies with a lower level of detail. Using forecast accuracies variable in time and predicted feed-in volume, the average balancing power potential at a required safety level of 99.99 % increases up to 67 % compared to constant forecast accuracy over the entire time of the day. Therefore, within the following assessments of balancing energy potentials the forecasting accuracy according to method (c) is applied.

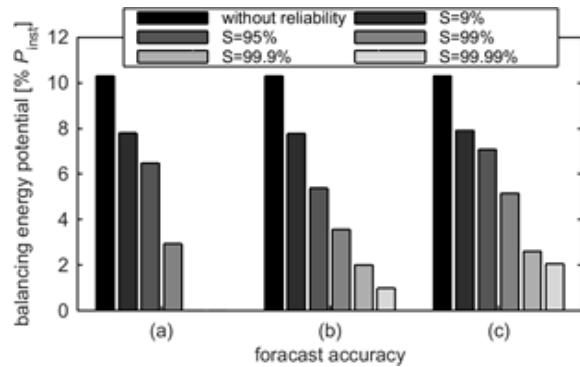


Figure 5: Balancing energy potential for different levels of detail of forecast accuracy and different reliabilities (P_{inst} : installed wind capacity).

4.2. Dependency on Different Product Length

Fig. 6 (left column in each section) shows the impact of different product length of balancing energy offers for the same wind park as in the previous investigation. The prediction accuracy of methodology (c) and a reliability of supply of 99.99 % is applied. Due to the fluctuating wind energy feed-in, the theoretical provided potential of balancing energy decreases significantly with increasing length of the product.

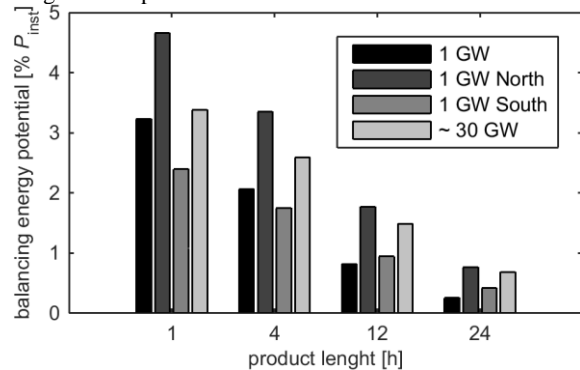


Figure 6: Balancing energy potential for different product length, regions, and sized wind parks (P_{inst} : installed wind capacity).

4.3. Dependency on Regional Resolution

In addition to market regulating factors, yield-dependent conditions influence the potential of balancing energy by wind turbines. Therefore, Fig. 6 (second and third column) shows the importance of sufficient meteorological conditions by comparing two further 1 GW wind parks. The values of these exemplary wind parks are an average of three wind parks located in the North,

respectively, South of Germany. Compared to the South the North of Germany is characterized by higher and less fluctuating wind speeds. Deductively, the average wind park located in the North has an around 50 % higher potential of balancing energy compared to the wind park located in the Southern part of Germany.

4.4. Dependency on Size of Wind Parks

Furthermore, Fig. 6 represents the impact of regional equalization effects within wind supply. With increasing distance between wind measurement stations, the correlation between their particular wind speeds decrease [16]. This effect can be transferred to the superposition of short-term fluctuations in the wind generation of distant wind farms, particularly between wind parks in areas with different weather conditions. Additionally, increased forecast accuracy in expanded areas is directly linked to this effect. The described impact of regional equalization effects on the balancing energy potential is assessed by comparing the 1 GW wind park from the previous investigation (Section 4.1) (Fig. 6, left column) and the exemplary German wind turbine portfolio, with around 30 GW (Fig. 6, right column). This investigation shows exemplary that a vast regional distributed and a more powerful wind farm has an increased relative balancing energy potential of around 30 %.

5. Conclusion and Future Prospects

The future energy supply will be characterized by further increasing integration of weather-dependent energy sources. To guarantee an efficient and safe operation of these sustainable electricity systems, feed-in prognosis will continue to be an indispensable part of the daily energy management and trading.

Therefore, the present paper provides an overview of the current prediction accuracy of wind supply in Germany. In this context, significant dependencies of the forecast errors could be identified. Decreasing prediction accuracy with lower predicted feed-in volume and increasing forecast horizon is characteristic. The results on one hand identify factors of influence for a further development of meteorological, respectively, power forecasting models, and on the other hand enable a detailed quantification of the day-ahead forecast accuracy variable in time and feed-in volume. By means of probabilistic classifications of the forecast errors, the day-ahead predicted wind feed-in could be subdivided in a reliable and non-reliable prognosis. This safe predictable day-ahead supply increases with decreasing reliabilities of the forecast quality and is basis for the assessment of the theoretical balancing energy potential by wind turbines for the following day. This potential is influenced by market-regulating and yield-dependent factors. It increases with shorter product lengths of bids, improved forecast accuracy of wind power feed-in, respectively, short-term tendering periods, and lower reliability levels of balancing power supply. Furthermore, an increased potential can be offered by bundling regional distributed wind farms. The whole wind energy portfolio in Germany could provide a maximum system capacity of 1.5 GW under a required level of security of 99.99 % as an annual average. The

averaged need of tertiary balancing energy in Germany between the years 2013 and 2015 was in a range of 2.5 GW [12]. Therefore, already today wind turbines could significantly contribute to the system stability. According to [19], the demand for balancing energy is expected to increase due to integration of higher shares of weather-dependent renewable energy systems. This increase counteracts with improving forecast accuracies through advancement of prognosis models, and the equalization of wind power feed-in through increased installation of offshore wind turbines [20]. Nevertheless, through a possible integration of wind turbines in the balancing energy market, the Must-Run base of conventional power plants in the system could be reduced. But for this economically and environmentally efficient use of wind turbines in the German active and balancing power market, the regulatory and market-economic conditions have to be adjusted. For the provision of control power by a regionally distributed wind parks, the capacity of the electrical network must be examined separately, in order to reduce additional network loads. Moreover, the control power potential of wind turbines could be increased through combinations with solar systems and storage opportunities. A temporal analysis of the need of control power and theoretical balancing energy potentials by renewables specifies the impact of weather-dependent renewable energy systems on active and control power supply system in temporal and spatial resolution.

References

- [1] REN21-Renewable Energy Policy Network for the 21st Century, "Renewables 2015 - Global Status Report". 2015.
- [2] 50Hertz Transmission GmbH, Netzkennzahlen. Available: www.50hertz.com (2016, Feb. 25).
- [3] D. R. Graeber, A. Kleine, Handel mit Strom aus erneuerbaren Energien: Kombination von Prognosen, 2014.
- [4] Fraunhofer IWES, "Regelenergie durch Windkraftanlagen: Abschlussbericht". 2014.
- [5] S. von Roon, "Auswirkungen von Prognosefehlern auf die Vermarktung von Windstrom", 2012.
- [6] A. Maaz, T. Drees, J. Sprey, A. Moser, "Simulation von Leistungsungleichgewichten resultierend aus Prognoseabweichungen erneuerbarer Energien". 2015.
- [7] P. Mathiesen, J. Kleissl, "Evaluation of Numerical Weather Prediction for Solar Forecasting". 2012.
- [8] TransnetBW GmbH, Netzkennzahlen. Available: www.transnetbw.de (2016, Feb. 25).
- [9] Amprion GmbH, Netzkennzahlen. Available: www.amprion.de (2016, Feb. 25).
- [10] TenneT TSO GmbH, Netzkennzahlen. Available: www.tennetso.de (2016, Feb. 25).
- [11] Informationsplattform der deutschen Übertragungsnetzbetreiber, EEG-Anlagenstammdaten. Available: www.netztransparenz.de (2016, Feb. 25).
- [12] 50Hertz Transmission GmbH, Amprion GmbH, TransnetBW GmbH, and TenneT TSO GmbH, regelleistung.net: Internetplattform zur Vergabe von Regelleistung. Available: www.regelleistung.net (2016, Feb. 25).
- [13] Deutsche Energie-Agentur GmbH (dena), "dena-Netzstudie II: Integration erneuerbarer Energien in die deutsche Stromversorgung im Zeitraum 2015 - 2020 mit Ausblick 2025". 2010.
- [14] Consentec GmbH, R2B Energy Consulting GmbH, "Voraussetzungen einer optimalen Integration erneuerbarer Energien in das Stromversorgungssystem: Studie im Auftrag

- des Bundesministeriums für Wirtschaft und Technologie (BMWi)". 2010.
- [15] Deutschen Wetterdienstes, Climate Data Center. Available: www.dwd.de (2016, Feb. 25).
- [16] A. Magdowski, M. Kaltschmitt, "Regelleistungspotenzial durch wetterabhängige erneuerbare Energieanlagen unter Einfluss regionaler Vergleichmäßigungseffekte". Nachhaltige Energieversorgung und Integration von Speichern - Tagungsband zur NEIS 2015.
- [17] A. K. Al-Awaad, "Beitrag von Windenergieanlagen zu den Systemdienstleistungen in Hoch- und Höchstspannungsnetzen". 2009.
- [18] S. Heier, "Windkraftanlagen; Systemauslegung, Netzintegration und Regelung". 2008.
- [19] O. Brückl, "Wahrscheinlichkeitstheoretische Bestimmung des Regel- und Reserveleistungsbedarfs in der Elektrizitätswirtschaft". 2006.
- [20] K. Rohrig, C. Richts, S. Bofinger, "Energiewirtschaftliche Bedeutung der Offshore-Windenergie für die Energiewende". 2014

Investigate the Natural Convection Heat Transfer in A PCM Thermal Storage System Using ANSYS/FLUENT

Maher M. Al-Maghalseh^{a, b, *}

^a College of Engineering, Palestine Polytechnic University, Hebron, Palestine

^b Faculty of Engineering and Environment, Northumbria University, Newcastle, UK

Abstract

The present paper presents four dimensional models for simulation of a Latent Heat Thermal Energy Storage System (LHTESS). The LHTESS is in the form of a rectangular container with a central horizontal pipe surrounded by a Phase Change Material (PCM). Paraffin wax with melting temperature of 60 oC is used as a PCM whilst water is used as a Heat Transfer Fluid (HTF). Thermo physical properties of paraffin wax are assumed to be constant in the modelling process, whereas the density variation is handled by using Boussinesq model. ANSYS/FLUENT software was used in simulating four dimensional models of temperature distribution, melting fraction, and flow fields during the melting process. Simulations performed provide information on the instantaneous temperature distribution, solidification/melting dynamics and the velocities field in the storage unit during the melting process. The effects of the natural convection on the charging (melting) process were also investigated.

© 2017 Jordan Journal of Mechanical and Industrial Engineering. All rights reserved

Keywords: PCM; thermal storage system; paraffin; solar energy, natural convection, CFD, ANSYS/FLUENT.

1. Introduction

Recently, solid-liquid phase change of PCM, for various geometric arrangements with natural convection in the liquid phase, has been investigated theoretically and experimentally. The thermal energy is stored in the PCM as latent heat and it is reutilized when it is needed. Therefore, understanding the natural convection inside the liquid PCM plays important rules in the design of thermal storage system. PCM is stored by different ways in LHTESS, for example, using cylinder enclosed with or without fins, cans, plates or sphere enclosure [1]. In the following study, the storage unit consists of a rectangular container with a horizontal pipe and PCM filled around the pipe. During the period of storage, a working fluid flows inside the horizontal pipe and the heat is transferred through the pipe walls to the PCM. Later, PCM reaches its fusion temperature and melting is started and then, natural convection motion appears. Consequently, the bouncy driven become strong enough to drive the melting process.

Many authors have tackled the natural convection during melting of PCM. Tan [2], experimentally investigated the buoyancy and natural convection phenomena during the melting process of PCM inside a spherical capsule. Indeed, validate these results with a numerical solution obtained with the CFD FLUENT. The most interesting finding was that the conduction heat transfer dominates during the early stage, whereas the buoyancy driven convection becomes more sufficient as the liquid fraction volume is increased. However, the

molten PCM ascends upward to the upper regions of the sphere because of natural convection phenomena. Consequently, the upper region of the sphere melts first and then the other regions. Another interesting finding from the computational results was that some chaotic fluctuation of the temperature distribution in some points inside the sphere and this is due to the unstable fluid layer in these points. However, the findings of the this study support the previous researches by the author [1, 3].

Nsofor [4] also experimentally investigated the heat transfer and natural convection phenomena in packed bed thermal storage system for high temperature. However, positive correlations were found in terms of Nusselt number, Prandtl number as well as Reynolds number and comparisons were made with existing correlations developed with similar storage media. Wu and Lacroix [5] analysed numerically the natural convection of melting PCM in a vertical cylindrical capsule heated from below. The model was solved using finite-difference method and compared the numerical prediction results with the numerical and experimental results of other authors [6-8]. It was reported that the heat transfer rate at the top surface was dominated by conduction, while it was decreased to zero when melting progressed and natural convection was fully developed. It was also observed that the highest heat transfer was at the bottom surface of the capsule. Rieger and Beer [9] examined the effect of natural convection flow on heat transfer during melting process of ice inside an isothermal horizontal cylinder. They predicted numerically the overall and local heat transfer coefficients, temperature fields, interface positions and flow pattern and

* Corresponding author e-mail: maherm@ppu.edu.

compared their numerical prediction results with the experimental results. It was reported that the heat transfer was enhanced at the lower part of the ice body when the wall temperature less than 8°C because of the density effect, while the ice body move downward when the wall temperature exceed 8°C . The same procedures have been applied by Rieger et al. [10] to investigate the heat transfer during melting n-octadecane as a PCM inside horizontal tube. Saitoh and Hirose [11] numerically investigated the natural convection inside a horizontal circulator cylinder capsule packed with PCM during melting and solidification process in the case of high Rayleigh numbers. The model obtained the transient solid-liquid interface, solid-liquid temperature, streamlines, isotherms, and heat stored. The numerical results was validated through comparison with results of Pannu [12]. In general, there was quite different from theirs both quantitatively and qualitatively. It is interesting to note that the natural convection controlled the melting heat transfer inside the capsule as well as the thermal instability happened at the bottom portion of the capsule.

Trp [13, 14] studied the transient heat transfer in the shell-and-tube thermal storage system in an experimental and numerical study. He developed a mathematical model based on non-isothermal phase transition and it has been implemented with a FORTRAN computer code. The numerical results were validated through a comparison with experiment data. He concluded that heat transferred from HTF to the PCM was slow; this is because of the large Prandtl numbers of the HTF. Therefore, a large amount of heat was carried out downstream with the HTF, while a small amount of heat was transferred to the PCM upstream. The same author [15] numerically investigated the effect of several geometric parameters and different HTF operation conditions on the heat transfer during both melting and solidification processes. They measured the transient temperature distribution of the HTF, PCM and tube wall.

The objective of this study is to investigate numerically the natural convection dominated melting of PCM filled around horizontal pipe within a rectangular container. Four different models are investigated (Fig. 1). First, the centre of the horizontal pipe is located at the centre of the rectangular container (Fig. 1.A). Second, the centre of the horizontal pipe is located by 5mm down from the centre of the rectangular container (Fig.1.B). Third, the centre of the horizontal pipe is located by 10mm down from the centre of the rectangular container (Fig.1.C). Last, the centre of the horizontal pipe is located by 15mm down from the centre of the rectangular container (Fig.1.D). The CFD findings are presented and discussed in the present study.

2. Simulation Model

Fig. 1 shows the cross section of the four different rectangular thermal storage configurations with horizontal pipe. The test unit has dimensions 75mm (width) \times 50mm (height) \times 500mm (depth). The rectangular container is filled with Paraffin wax which has a melting point of 60°C , latent heat storage capacity of 200 kJ/kg, density of 800 kg/m³, specific heat of 2050J/kg K, dynamic viscosity of 0.035 kg/m-s, and thermal conductivity of 0.25 W/m K. The horizontal pipe was 10mm of inner diameter with a thickness of 1mm. The HTF is circulated inside the pipe with inlet temperature of 353 K in order to charge the PCM storage unit. The mass flow rate of water is 0.0037 Kg/s. The computational grid of the system was built using ICEM CFD 13.0 software by ANSYS. Meshing of the model was generated by using hexahedral elements and boundary layers were created around the pipe. Upon several trials it was found that the hexahedral computational grid with 636768 elements would be sufficient for accurate 3D modelling of the heat transfer in the PCM system.

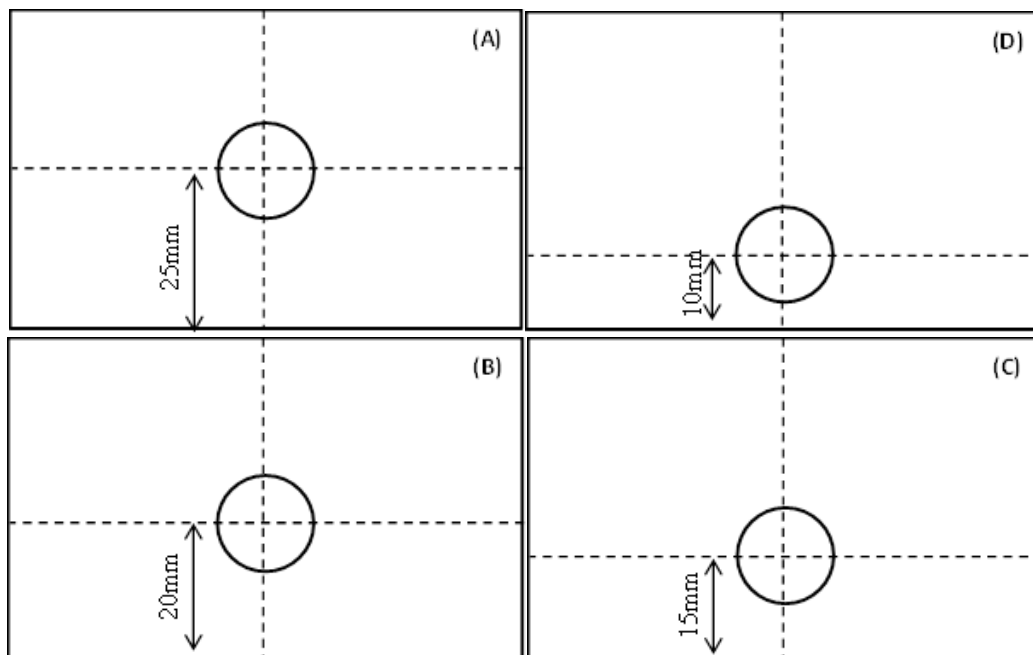


Figure 1: Schematic view of the four different models, (A) case 1, (B) case2, (C) case3, and (D) case4

The flow inside the pipe was described using transient simulations with *k-epsilon* turbulence model deployed. The solidification/melting model was used in order to examine the phase change phenomena in paraffin wax. The time step used in calculations was set to 0.1 second. To obtain numerical results the first-order upwind spatial discretization and the pressure solver with PRESTO algorithm for pressure-velocity coupling were used. Convergence criteria were defined by setting the absolute residual value at 10⁻⁶ for energy and at 10⁻³ for all other variables. The mathematical formulations for solving PCM related problems have been categorized [16] as fixed grid, variable grid, front-fixing, adaptive grid generation, and enthalpy methods. Two methods are used to analyse the heat transfer in solid-liquid PCMs. These are the temperature-based and enthalpy-based methods. In the former, temperature is considered to be a single dependent variable. The energy equations for both solid and liquid are formulated separately; and thus the solid-liquid interface positions can be tracked easily to achieve an accurate solution for the problem [17]:

$$\frac{\partial T_s}{\partial n} k_s = \frac{\partial T_l}{\partial n} k_l + \rho L v_n \quad (1)$$

where T_s denotes the temperature in the solid phase; T_l is the temperature in the liquid phase. k_s , and k_l are the thermal conductivity of the solid phase and liquid phase, respectively; n is the unit normal vector to the interface; L is the latent heat of the freezing; and v_n is the normal component of the velocity of the interface.

However, an enthalpy-porosity method is used for modelling the solidification/melting process [18]. This technique is described in detail by Voller and Prakash [19].

The energy conservation equation for this case is written as:

$$\frac{\partial}{\partial t} (\rho H) + \nabla \cdot (\rho \mathbf{v} H) = \nabla \cdot (k \nabla T) + S \quad (2)$$

where H , is the enthalpy, ρ is the density, \mathbf{v} is fluid velocity and S is the source term.

The enthalpy of the material is calculated as the sum of the sensible heat, h , and latent heat, ΔH :

$$H = h + \Delta H \quad (3)$$

The sensible heat is calculated as:

$$h = h_{ref} + \int_{T_{ref}}^T c_p dT \quad (4)$$

where, h_{ref} is the reference enthalpy, T_{ref} is the reference temperature and c_p is the specific heat at constant temperature.

The latent heat is also calculated as:

$$\Delta H = \beta_l L \quad (5)$$

The liquid fraction, β_l , can be calculated as:

$$\beta_l = 0, \text{ when } T < T_{solid} \\ \beta_l = 1, \text{ when } T > T_{solid} \quad (6)$$

$$\beta_l = \frac{T - T_{solid}}{T_{liquid} - T_{solid}} \text{ if } T_{solid} < T < T_{liquid}$$

The solid and liquid temperatures are also calculated as:

$$T_{solid} = T_{melt} + \sum_{solutes} K_i m_i Y_i \quad (7)$$

$$T_{liquid} = T_{melt} + \sum_{solutes} m_i Y_i \quad (8)$$

where, K_i is the partition coefficient of solute i , which is the ratio of the concentration solid to that in the liquid at the interface; Y_i is the mass fraction of solute i , and m_i is the slope of the liquid surface with respect to Y_i [18].

The source term in the momentum equation can be written as [18]:

$$S = \frac{(1 - \beta)}{(\beta_l^3 + \epsilon)} A_{mush} (\mathbf{v} - \mathbf{v}_p) \quad (9)$$

3. Result and Discussion

Numerical simulation is carried out for cyclic melting process of Paraffin wax filled in rectangular thermal storage unit involving horizontal pipe and the results are presented and evaluated in this section. Numerical simulations investigate the natural convection dominated melting of PCM for different model geometries (Fig.1). At the start of the melting cycle, the inlet temperature of HTF inside the pipe is maintained at fixed temperature of 353 K and the initial temperate of PCM is 300 K. Further, mass flow rate of HTF is maintained at 0.0037 Kg/s. Figs. 2-3 distinctly show temperature distribution and melting/solidification fields along the four different geometries after 10000sec.

The results show that the temperature starts to rise gradually in the region of the storage container close to the pipe wall and then ascends upward to the upper region at the centre of the container. In this stage, sensible heat was transferred from the pipe wall to the PCM solid by pure conduction, and then a thin liquid layer was created between the pipe and the solid PCM. The solid-liquid interface expanded gradually over the axial and radial directions with respect to time. Thereafter, the melting fronts were dominated by natural convection heat transfer in the melted regions of PCM. Consequently, the convection heat transfer drives circulation in the melted PCM due to the buoyancy force. The molten PCM ascends upward from the bottom to the upper regions at the center of the container and returns downward to complete the natural convection circle, since the molten PCM has the lower density and viscosity. The convection circle became more sufficient as the liquid fraction volume is increased.

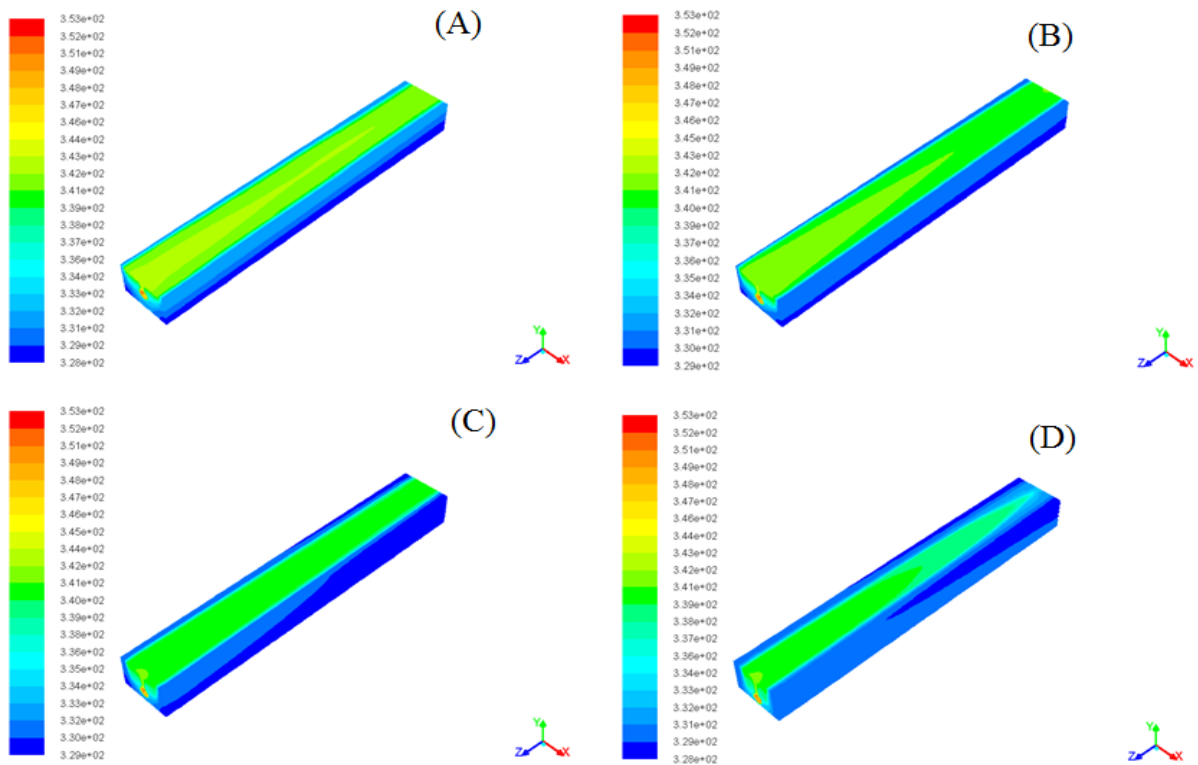


Figure 2: Temperature distribution process in the domain, (A) case 1, (B) case2, (C) case3, and (D) case4. Elapsed time is 10000 s.

Two factors affected the natural convection in the melted PCM; these are the temperature difference as well as the distance between the pipe wall and solid-liquid interface. This is clearly explained in Figs. 4-5. It can be

also deduced that the molten regions of PCM is remarkably bigger in case 4, and then in cases 3 & 2 with respect to that of case 1.

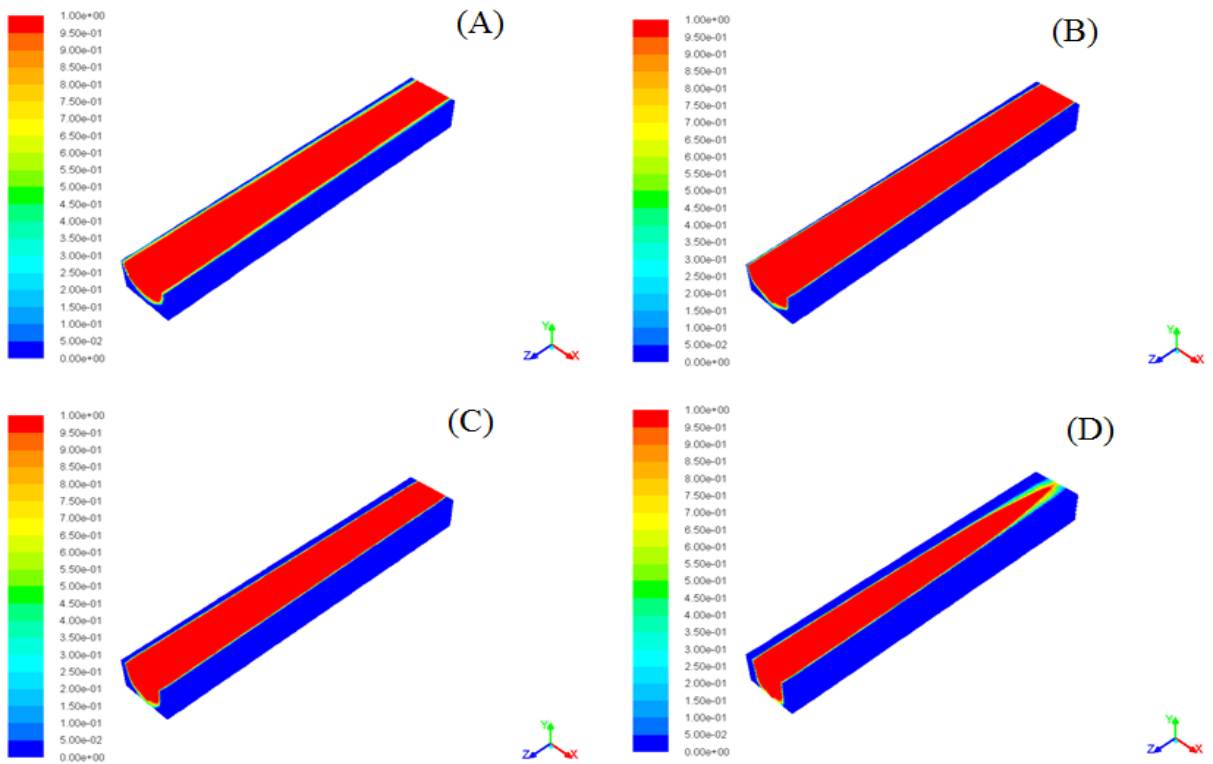


Figure 3: Solidification/Melting process in the domain, (A) case 1, (B) case2, (C) case3, and (D) case4. Elapsed time is 10000 s

This is because the natural convection in the PCM is affected by the temperature difference as well as the distance between the pipe wall and the solid PCM. This therefore increases the amount of PCM, resulting of increase the distance between the pipe wall and solid PCM, and so increases the natural convection mechanism.

In order to evaluate the performance of the thermal storage unit 132 monitoring points were set inside the

domain with PCM to record the variation of the temperature as a function of time. These points are located in 11 measurement planes perpendicular to the axis of the domain (see Fig. 6). Each plane contains 12 monitoring points, as shown in Fig. 7. All monitoring points are divided into three groups. The first group of 44 points was set in the upper part of the computational domain (u1-u44).

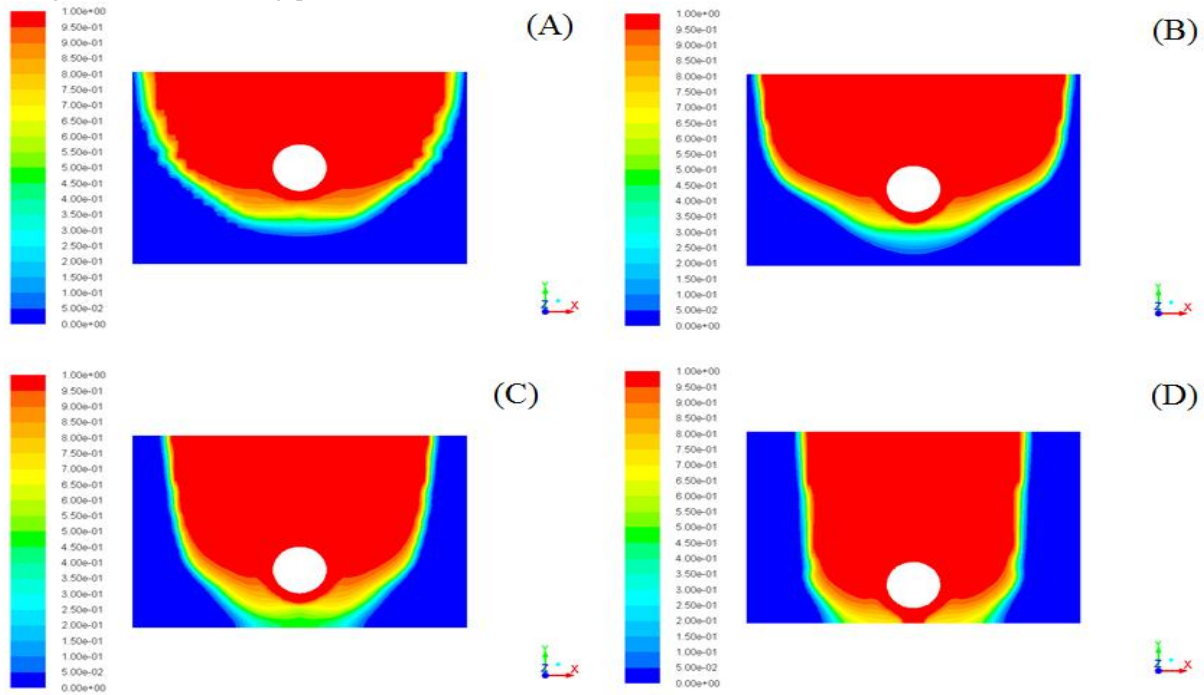


Figure 4: Melting process in the front section of the domain, (A) case 1, (B) case2, (C) case3, and (D) case4. Elapsed time is 10000 s.

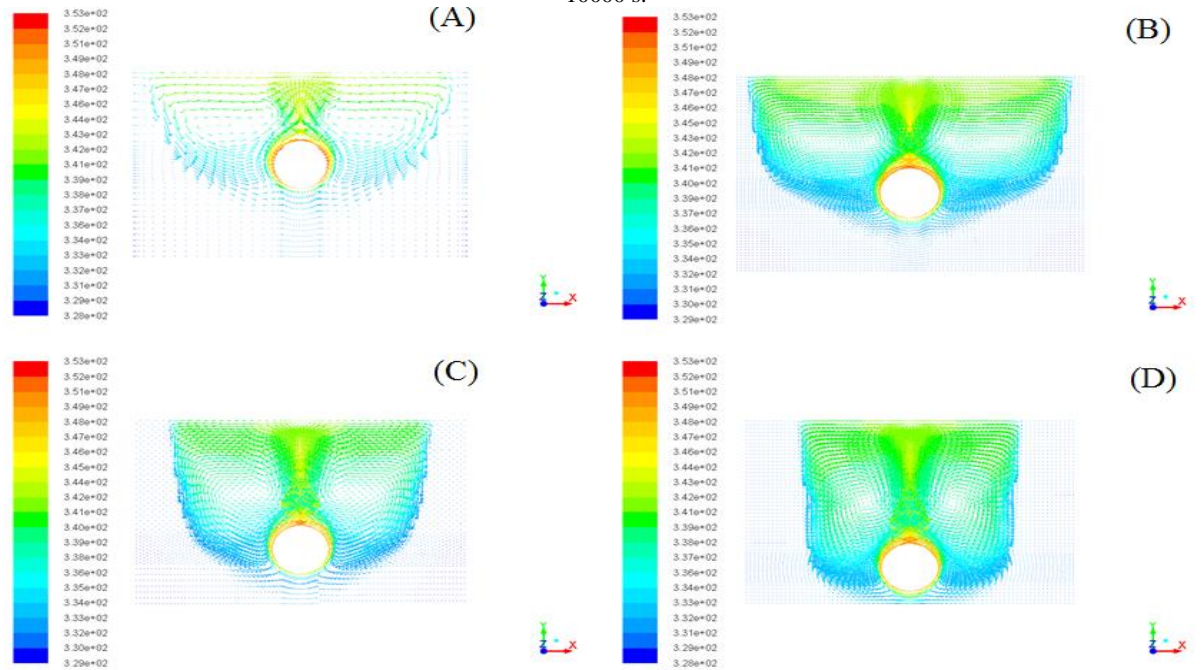


Figure 5: Velocity profile in the front section of the domain, (A) case 1, (B) case2, (C) case3, and (D) case4. Elapsed time is 10000 s.

The second groups of 44 points are located in the bottom part of the domain (b1-b44), and the last groups of 44 points are located at the side of the domain (e1-e44). Figs. 4-6 show the temperature variations monitoring points in the first section of the computational domain (the measurement plane 1). Fig. 3 shows the temperature variation at u4, which located at the upper part of the domain. It can be seen that the temperature in case1 is the highest compared to that in cases 2, 3 and 4. The reason behind this is that the distance between the point u4 at the upper part (Fig. 8) and the outer surface of the pipe is less than those in cases 2, 3 and 4.

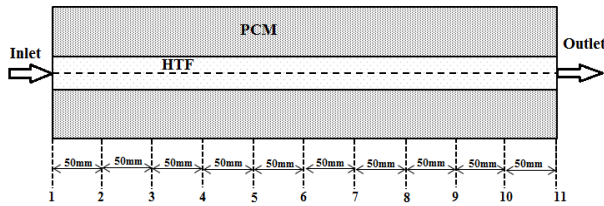


Figure 6: Measurement planes along the tube.

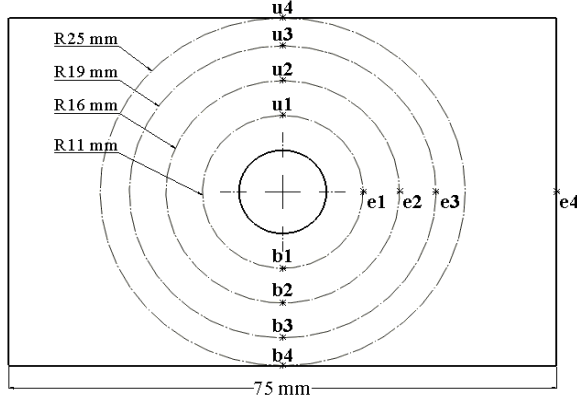


Figure 7: The location of 12 monitoring points in the measurement plane 1.

It can be contributed to the conduction heat transfer from the pipe wall to the PCM is maintained constant due to the same inlet parameters and boundary conditions in all cases. However, the temperature distribution in case1 is more significant on the points at the upper part of the storage unit due to the effect of natural convection. On the contrary, the temperature at the points at the bottom parts in is significantly increased as the distance between the PCM and the HTF decreased. It can be seen in Fig. 9 that the temperature variation at the bottom parts in case 4 is higher with respect to that of other cases.

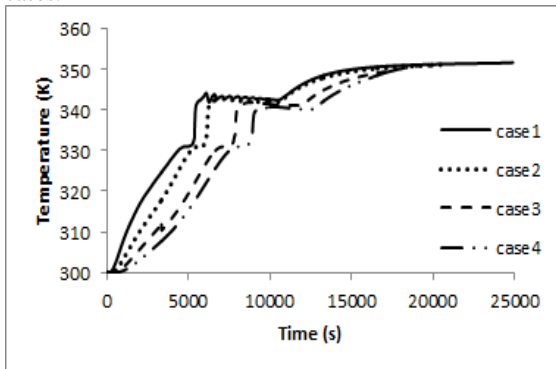


Figure 8: The temperature variation at point u4 (the top of the domain, first measurement plane).

Figs. 11 and 12 show the liquid fraction on PCM against time variation and total melting time. It can be deduced from this figures that the total melting time was reduced by approximately by 16.57% with case2, 31.83% with case3 and 41.3% with case 4, compared to that of case1. As mentioned above, the average heat is transferred to the PCM by conduction heat transfer from the pipe wall to solid PCM and convection heat transfer in the melted PCM. Indeed, conduction heat transfer was maintained by using the same operation and boundary conditions on the pipe and HTF in all cases. Thus, total melting time was significantly reduced in cases 3&4 due to the natural convection in melted PCM. The analysis further indicated that the appropriate configuration and height for the tube as in case 4 which provides the shorter melting time of the PCM.

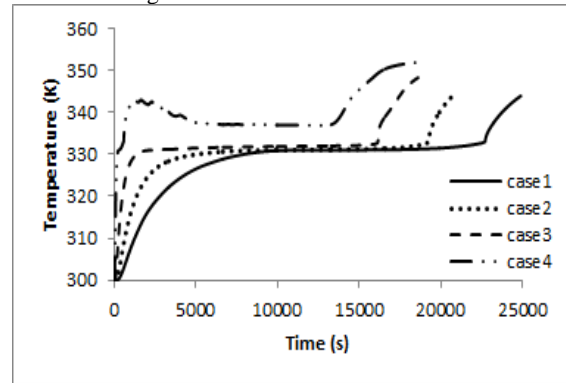


Figure 9: The temperature variation at point b4 (the bottom of the domain, first measurement plane).

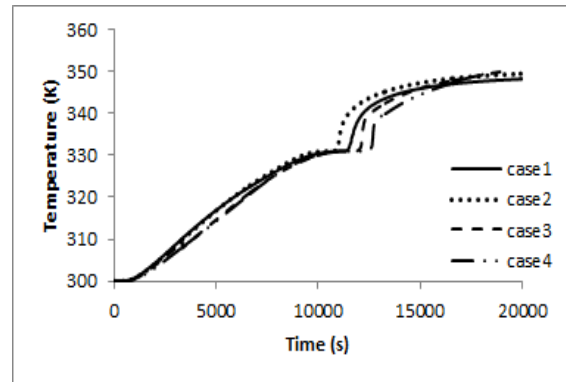


Figure 10: The temperature variation at point e4 (the side of the domain, first measurement plane).

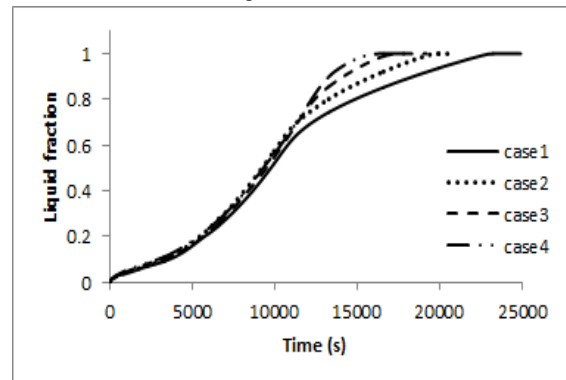


Figure 11: Melting fraction on PCM.

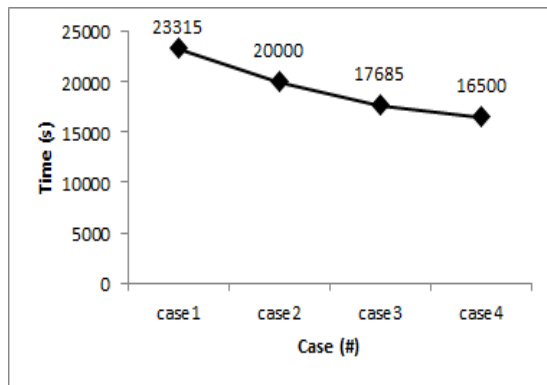


Figure 12: Total melting time of PCM.

4. Conclusion

In the present study, a numerical simulation has been carried out to determine the effect of natural convection dominated melting of PCM filled around horizontal pipe within a rectangular thermal storage unit. The most obvious finding to emerge from this study is that the natural convection heat transfer has a considerable effect on both axial and radial temperature distribution along the storage unit, and so reducing the temperature difference between the pipe walls and solid-liquid interface, therefore, reducing the total melting time of PCM. The tests for investigating four different thermal storage configurations were carried out. The results indicate that the total melting time was approximately reduced 16.57% with case2, 31.83% with case3 and 41.3% with case 4, compared to that of case1. Indeed, heat transfer rate enhanced is significantly more pronounced in natural convection in melted PCM, while the conduction heat transfer was maintained constant in all cases by using the same operation and boundary conditions on the pipe and HTF.

References

- [1] F. L. Tan and C. W. Chan, "Solidification inside a sphere—an experimental study," *International Communications in Heat and Mass Transfer*, vol. 33, pp. 335-341, 2006.
- [2] F. L. Tan, S. F. Hosseinizadeh, J. M. Khodadadi, and L. Fan, "Experimental and computational study of constrained melting of phase change materials (PCM) inside a spherical capsule," *International Journal of Heat and Mass Transfer*, vol. 52, pp. 3464-3472, 2009.
- [3] F. L. Tan., "Constrained and unconstrained melting inside a sphere," *International Communications in Heat and Mass Transfer*, vol. 35, pp. 466-475, 2008.
- [4] E. C. Nsofor and G. A. Adebisi, "Measurements of the gas-particle convective heat transfer coefficient in a packed bed for high-temperature energy storage," *Experimental Thermal and Fluid Science*, vol. 24, pp. 1-9, 2001.
- [5] Y. K. Wu and M. Lacroix, "Melting of a PCM inside a vertical cylindrical capsule," *International Journal for Numerical Methods in Fluids*, vol. 20, pp. 559-572, 1995.
- [6] Y. K. Wu, "Numerical Studies of Melting Process in a Cylindrical Enclosure," Ph.D., École Polytechnique de Montréal, 1990.
- [7] M. Prud'homme, T. H. Nguyen, and Y. K. Wu, "Simulation numérique de la fusion à l'intérieur d'un cylindre adiabatique chauffé par le bas," *International Journal of Heat and Mass Transfer*, vol. 34, pp. 2275-2286, 1991.
- [8] Y. K. Wu, M. Prud'homme, and T. H. Nguyen, "Étude numérique de la fusion autour d'un cylindre vertical soumis à deux types de conditions limites," *International Journal of Heat and Mass Transfer*, vol. 32, pp. 1927-1938, 1989.
- [9] H. Rieger and H. Beer, "The Melting Process of Ice Inside a Horizontal Cylinder: Effects of Density Anomaly," *Journal of Heat Transfer*, vol. 108, pp. 166-173, 1986.
- [10] H. Rieger, U. Projahn, M. Bareiss, and H. Beer, "Heat Transfer During Melting Inside a Horizontal Tube," *Journal of Heat Transfer*, vol. 105, pp. 226-234, 1983.
- [11] T. Saitoh and K. Hirose, "High Rayleigh Number Solutions to Problems of Latent Heat Thermal Energy Storage in a Horizontal Cylinder Capsule," *Journal of Heat Transfer*, vol. 104, pp. 545-553, 1982.
- [12] J. Pannu, G. Joglekar, and P. A. Rice, "Natural convection heat transfer to cylinders of phase change material used for thermal storage," *American Institute of Chemical Engineers*, vol. 76, pp. 47-55, 1980.
- [13] A. Trp, "A numerical and experimental study of transient heat transfer in a shell-and-tube latent heat storage unit with paraffin as a phase change material," presented at the Energy and the Environment, 2002.
- [14] A. Trp, "An experimental and numerical investigation of heat transfer during technical grade paraffin melting and solidification in a shell-and-tube latent thermal energy storage unit," *Solar Energy*, vol. 79, pp. 648-660, 2005.
- [15] A. Trp, K. Lenic, and B. Frankovic, "Analysis of the influence of operating conditions and geometric parameters on heat transfer in water-paraffin shell-and-tube latent thermal energy storage unit," *Applied Thermal Engineering*, vol. 26, pp. 1830-1839, 2006.
- [16] N. Özışık, *Finite Difference Methods in Heat Transfer*,: Taylor & Francis, 1994.
- [17] A. A. Al-abidi, S. Bin Mat, K. Sopian, M. Y. Sulaiman, and A. T. Mohammed, "CFD applications for latent heat thermal energy storage: a review," *Renewable and Sustainable Energy Reviews*, vol. 20, pp. 353-363, 2013.
- [18] *ANSYS FLUENT 14.0 Theory Guide*, : ANSYS, Inc, 2011.
- [19] V. R. Voller and C. Prakash, "A fixed grid numerical modelling methodology for convection-diffusion mushy region phase-change problems," *International Journal of Heat and Mass Transfer*, vol. 30, pp. 1709-1719, 1987.

Transevaporative Cooling Performance of a Three-Sided Wind Catcher

M.N. Khan ^a, I. Janajreh ^{*b}

^a Dept. of Mechanical and Materials Engineering, Masdar Institute of Science and Technology, Abu Dhabi, United Arab Emirates

^b Dept. of Mechanical and Materials Engineering, Khalifa University of Science and Technology, Abu Dhabi, United Arab Emirates,

Abstract

A wind catcher is a structure used for capturing wind at higher elevations and directing it to the desired locations for cooling. A down-draft evaporative wind catcher uses the principle of evaporative cooling to provide passive cooling as well as natural ventilation. The present paper presents the performance of a three-sided wind catcher at Masdar city, subjected to mist injection. The 45 m tall wind catcher is modelled for different wind speeds ranging from 1-5 m/s using computational fluid dynamics. The numerical model accounts for Eulerian-Lagrangian formulation. Equations of continuity, momentum and energy along with realizable k- ϵ turbulence model are employed to calculate the flow field. Droplet evaporation in discrete phase model is used for tracking the liquid water mists. The results demonstrate that the wind catcher performance is greatly influenced by the external wind speed. Higher wind speed resulted in higher rate of evaporation and lower air temperatures. The density, water vapour mass fraction and the relative humidity increases as the air flow travel downwards to the wind catcher exit. While the temperature decreases significantly in the downward direction of the wind catcher. The present study shows the promise of using the computational models in analysing and optimizing the design and performance of the wind catcher.

© 2017 Jordan Journal of Mechanical and Industrial Engineering. All rights reserved

1. Introduction

Refrigeration and cooling techniques, like the free cooling technique [1] and evaporative cooling, are used for energy efficiency. Evaporative cooling method for passive cooling and air conditioning of the buildings has been in practice since olden days in dry climatic regions, such as Middle Eastern countries. Various types of designs and configurations have been used, such as spraying the walls with water or building a special structure to capture the wind and passing through moist surfaces for cooling [2-3]. Detailed description can be found elsewhere [4]. Wind catcher structures have been given different names in different regions. They are called Badinge in Syria, Baudgeers in Iran and Burjeel in gulf region. Wind catchers are the structures which have been used to provide passive cooling and natural ventilation. These towers are designed to catch the wind at higher elevations and direct them to the desired spaces [4]. The simplest form of the tower provides sensible cooling while evaporative cooling occurs when water is introduced into the system [5]. Evaporative cooling results in reduction in temperature from evaporation of a liquid. It is due to the removal of latent heat from the hot incoming air. This could be integrated in the wind catcher system by using different techniques, such as the mist spray, wetted clay columns, wetter mats etc. Good ventilation along with cooling is desired for

indoor spaces. The wind speeds greatly influence the ventilation since high wind speeds provide high air flow rate. The air flow inside the wind catcher is greatly influenced by the wind speed, ambient temperature, atmospheric relative humidity, amount of water added when evaporative cooling is desired and the geometry of the wind catcher (cross-sectional area, height of the tower etc.) All these parameters have to be studied in detail in order to obtain an optimized performance of the wind catcher.

Several experimental evaluations have been performed on various kinds of wind catcher designs. Elmualim [6] conducted an experimental investigation of the performance of square and circular cross-section wind catchers in a wind tunnel. Pressure coefficients, air speed and volumetric flow rates were measured. A Computational Fluid Dynamic (CFD) investigation based on the experiments has also been performed to obtain the pressure distribution and air flow pattern in and around wind catcher. It was observed that the performance of the wind catcher depends mainly on the speed and the wind direction. It was also reported that ventilation rate increases as the velocity of air increases.

Kirk and Kolokotroni [7] conducted air-exchange tests and reported that both wind and stack-effect influences air exchange rate through the buildings. Su and Riffat [8] conducted the flow rate measurements for various wind speeds in a mono-draught wind catchers. The effect of

* Corresponding author e-mail: ijanajreh@masdar.ac.ae.

varying the room pressure on the supply and extract flow rate from the openings of the room had also been studied and the effect is found to be quite large at low wind speeds. Bahadori *et al.* [9] measured pressure coefficients in the wind catchers to evaluate the air flow pattern. Wind catchers are ongoing topic of interests for the reduction and implementation of efficient air conditioning at lower energy penalty for building. Designing an efficient wind catcher system for different climatic conditions is a difficult task. A study was conducted by Dehghani-sanij *et al.* [10]. A new efficient wind catcher system has been designed and tested in real conditions. The advantages of the wind catcher system were demonstrated. However, the experimental studies of wind catcher systems are costly and very difficult. The assessment of wind catcher using CFD is very important for performance evaluation and improvements in the system design.

CFD has been widely used to study the air flow in and around buildings [11], since it can provide detailed distribution of airflow velocity, temperature, pressure and humidity. The results obtained have been approved useful for applications of cooling, ventilation and low rise structural loading [12] as well permeable screen structural loading and for building code revisions [13]. Significant literature is available on such studies based on different climatic conditions and design of the wind catcher system. Kalantar [14] conducted a numerical study of the cooling performance of a wind catcher in a hot and dry region of Yazd in Iran. The results obtained complement the promise of evaporative cooling in a hot and dry region particularly when wind catcher is equipped with the water spray system. Saffari and Hosseinnia [15] used a two-phase Euler-Lagrange model to investigate the performance of a new wind catcher design. The design consists of wetted columns with wetted curtains hung in the tower. The effect of water droplet temperature and its diameter, wind velocity, temperature and relative humidity had been investigated. It was reported that wetted columns with 10 m height decreases the ambient air temperature significantly by 12° C and increases its relative humidity by 22%.

The present authors, in a recent work, numerically assessed trans-evaporative cooling in providing occupants comfort in two-level simple dwelling in arid region [16]. Limited studies have addressed the three sided wind catcher in hot and humid climatic conditions. In the present study, the performance of the three sided wind catcher at the Masdar City, Abu Dhabi has been investigated numerically (see Fig. 1). The wind catcher is situated in the middle of an open top court connected with narrow corridors. The wind catcher helps in lowering the temperature down to reasonable range during hot summer. Temperatures and relative humidity in Abu Dhabi can reach as high as 45 °C and 27-80%, respectively. Hence, it is a challenge to use a wind catcher that can lower the air temperature while maintaining the relative humidity in comfort zone. On the other hand, wind speeds range from 4-7 m/s which is a favorable point. The column of the wind catcher is in the form of slightly converging-diverging tube in which the added evaporative fluid mass helps in accelerating the incoming air velocity at the exit of the wind catcher providing excellent air flow pattern in the court. The cooling output from the wind catcher is

heavily dependent on the wind speed as it affects the heat and mass transfer characteristics. Hence, the performance of the wind catcher under different wind speeds has been evaluated.

2. Description of the Wind Catcher

Generally, wind catchers are installed on the roof top of the buildings, but they also used in providing the cooling effect to the semi-enclosed spaces. The 45 m long Masdar City wind tower is a three-sided wind catcher with a circular cross-section and is used to provide cooling in an open-top court yard of nearly 20m × 20m. The schematic of the wind tower is shown in Fig. 1. The diameter of the tower varies from top to bottom with a mean diameter of 4.9 m. It is mounted in steel frame structure at the top of which there are nine louvers on each side, which opens in the direction of the prevailing wind and closes or adjusted in other directions to trap the maximum amount of wind. The wind then flows down into an impermeable column made of Polytetrafluoroethylene (PTFE) membrane that directs the wind down to the court yard. For evaporative cooling, mist generators are employed at the tower top entry. Depending on the temperature, humidity and wind speed, the mist generators can add evaporative cooling to the air.

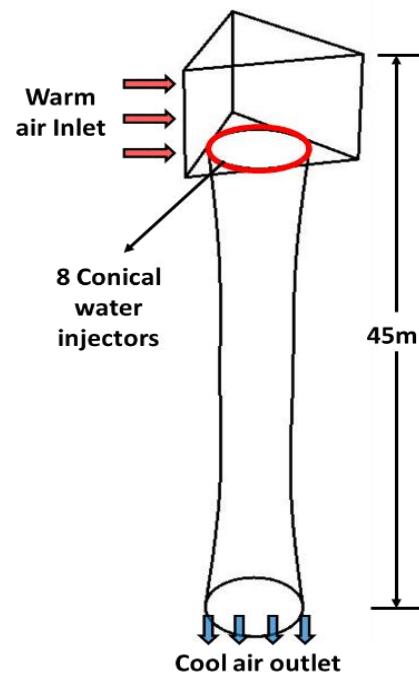


Fig. 1: Schematic of the three sided wind catcher at Masdar City

3. Computational Fluid Dynamic Modeling

3.1. Geometry

The three-dimensional geometrical model, based on the aforementioned dimensions, is presented in Fig. 2. The overall numerical domain size is 110m × 60m × 40m and bounded by two sided far fields, incoming velocity (S1) and exit pressure (S4), ground (represented by black

surface) and top symmetry. The air flows through the velocity inlet (S1) and exit the domain through the pressure outlet (S4). It is assumed that air is entering the wind catcher from only one fully open side (S2) louvers and the other two side louvers are closed. The outlet of the wind catcher is about 3m above the ground. The ground is made of concrete and is represented as no-slip wall in Fig. 2. The water injectors are introduced at the very top entrance of the converging-diverging section of the wind catcher before it is driven in the downward direction. This will ensure that the water droplets experience higher residence time in contact with the air and eventually reducing the air temperature.

3.2. Governing Equations

In the Eulerian-Lagrangian approach, the air flow is considered a continuous phase using the Eulerian formulation whereas the water droplets and their trajectories are considered a discrete phase using the Lagrangian formulation. Flow field is three dimensional, turbulent, non-isothermal and incompressible in nature.

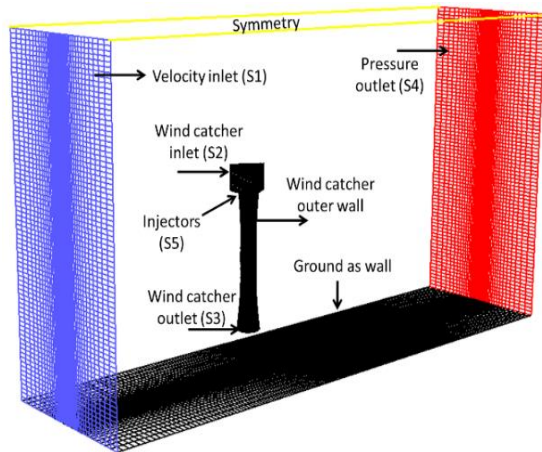


Fig. 2: Geometry and computational domain

The following are the governing equations for continuous (air) and discrete (water) phases and their sub-modeling scalar transport equations.

3.2.1. Continuous Phase (Air)

Continuity Equation

$$\frac{\partial(\rho u_i)}{\partial x_i} = S_m \quad (1)$$

where ρ is the moist air density (kg/m^3), u_i is the velocity vector (m/s) and S_m is the mass source term ($\text{kg/s}\cdot\text{m}^3$) which is added or removed from the continuous phase due to evaporation or condensation of the water droplets.

Momentum Equation

$$\frac{\partial}{\partial x_i}(\rho u_i u_j) = \frac{\partial p}{\partial x_j} + \frac{\partial}{\partial x_j} \left[\mu \left(\frac{\partial u_i}{\partial x_j} + \frac{\partial u_j}{\partial x_i} \right) \right] + \frac{\partial}{\partial x_j} (-\rho \overline{u'_i u'_j}) + f_i \quad (2)$$

Booussinesq hypothesis has been employed to relate the Reynolds stresses ($\rho \overline{u'_i u'_j}$) to the mean velocity gradient, p

is the static pressure (Pa), μ is the dynamic viscosity (Pa·s) and f_i is the external body force in j^{th} direction (N/m^3).

Energy Equation

$$\frac{\partial}{\partial x_j} u_i (\rho E + p) = \frac{\partial}{\partial x_j} \left[\left(\gamma + \frac{c_{pa} \mu_t}{Pr_t} \right) \frac{\partial T}{\partial x_j} - \sum_j h_j J_j \right] + S_h \quad (3)$$

where γ is the thermal conductivity of the fluid ($\text{W/m}\cdot\text{K}$), c_{pa} is the specific heat of air at constant pressure ($\text{J/kg}\cdot\text{K}$), μ_t is the turbulent viscosity (Pa·s), Pr_t is the turbulent Prandtl number, T is the temperature (K), h_j is the enthalpy of the species (J/kg), J_j is the diffusion flux of species j ($\text{kg/m}^2\cdot\text{s}$) and S_h is any volumetric source. The term E is defined as follows:

$$E = \sum h_j Y_j + \frac{u^2}{2} \quad (4)$$

where Y is the species mass fraction

Species Transport Equation

Species transport equation of water vapor mass fraction (Y_{H_2O}) into air can be defined as follows:

$$\frac{\partial}{\partial x_j} (\rho Y_{H_2O} u_i) = \frac{\partial}{\partial x_j} \left[\left(\rho D_{H_2O} + \frac{\mu_t}{Sc_t} \right) \frac{\partial Y_{H_2O}}{\partial x_j} \right] + S_{H_2O} \quad (5)$$

where D_{H_2O} is the diffusion coefficient of water vapor into air (2.88×10^{-5}), Sc_t is the turbulent Schmidt number (0.7) and S_{H_2O} is the water vapor added to or removed from the air due to evaporation or condensation.

Turbulent Scalar Equations

The turbulent kinetic energy is written as:

$$\frac{\partial}{\partial x_i} (\rho k u_i) = \frac{\partial}{\partial x_j} \left[\left(\mu + \frac{\mu_t}{\sigma_k} \right) \frac{\partial k}{\partial x_j} \right] + G_k + G_b - \rho \varepsilon - Y_M + S_k \quad (6)$$

and the turbulent dissipation rate is expressed as:

$$\frac{\partial}{\partial x_i} (\rho \varepsilon u_i) = \frac{\partial}{\partial x_j} \left[\left(\mu + \frac{\mu_t}{\sigma_\varepsilon} \right) \frac{\partial \varepsilon}{\partial x_j} \right] + \rho C_1 S_\varepsilon - \rho C_2 \frac{\varepsilon^2}{k + \sqrt{\nu \varepsilon}} + C_{1\varepsilon} \frac{\varepsilon}{k} C_{3\varepsilon} G_b \quad (7)$$

where k is the turbulent kinetic energy (m^2/s^2), ε is the turbulent dissipation rate (m^2/s^3), σ_k and σ_ε are the turbulent Prandtl numbers for k and ε , respectively, G_k and G_b represents the generation of turbulent kinetic energy due to the mean velocity gradients and buoyancy, respectively, Y_m here is the contribution of the fluctuating dilation in compressible turbulence to the overall dissipation rate, C_s are the constants and S is the source term.

The species transport equation and the turbulent scalar equations are applied to the continuous phase only. On the other hand, the liquid droplets are formulated as discrete particles. The species transport equation is used for the air and the water mass fraction within the air after evaporation takes place. As the velocity is significantly high, the Reynolds number for the continuous phase falls in turbulent region. Better mixing, high heat and mass transfer occurs during turbulence and hence, it should be taken into account in order to accurately predict the wind

catcher performance. Therefore, the realizable k-epsilon turbulent model is employed that takes care of turbulence.

3.2.2. Discrete Phase (Water)

Water Droplet Trajectory Calculations

In the Lagrangian formulation, the water droplet velocity is related to the rate of change of droplet position. The trajectory is predicted by using the force balance on the droplet which equates the particle inertia with the forces acting on the particle and can be written as:

$$\frac{du_p}{dt} = F_D(u - u_p) + \frac{g(\rho_p - \rho)}{\rho_p} + F_x \quad (8)$$

here u is the moist air velocity (m/s), u_p is the droplet velocity (m/s), $F_D(u - u_p)$ is the drag force per unit droplet mass, g is the gravitational acceleration (m/s²), ρ_p is the droplet density (kg/m³), ρ is the moist air density (kg/m³) and F_x is the additional forces added as the source terms:

$$F_D = \frac{18\mu}{\rho_p d_p^2} \frac{C_D Re}{24} \quad (9)$$

$$C_D = a_1 + \frac{a_2}{Re} + \frac{a_3}{Re^2} \quad (10)$$

$$Re = \frac{\rho d_p |u_p - u|}{\mu} \quad (11)$$

where d_p is the droplet diameter (m), C_D is the drag coefficient, Re is the Reynolds number and a_1 , a_2 and a_3 are constants.

Heat and Mass Transfer Calculations

Inside the wind catcher, the heat is transferred from the hot surrounding air into the water droplet by convection and evaporation. The heat transfer due to radiation is neglected in this study. The heat balance relating the droplet temperature to the convective heat transfer is given as:

$$m_p c_{pw} \frac{dT_p}{dt} = h A_p (T_\infty - T_p) \quad (12)$$

where m_p is the droplet mass (kg), c_{pw} is the water droplet heat capacity (J/kg·K), A_p is the droplet surface area (m²), T_∞ is the local temperature of the continuous phase (K), h is the convective heat transfer coefficient (W/m²·K) and T_p is the droplet temperature (K).

The droplet temperature at the next time step is calculated by integrating the above equation and is as follows:

$$T_p(t + \Delta t) = T_\infty + (T_p(t) - T_\infty) e^{(-A_p h / m_p c_p) \Delta t} \quad (13)$$

where Δt is the integration time step

The heat transfer coefficient (h) is calculated using the correlation of Ranz and Marshall [17]:

$$Nu = \frac{h d_p}{k_\infty} = 2.0 + 0.6 Re_d^{1/2} Pr^{1/3} \quad (14)$$

where Nu is the Nusselt number, k_∞ is the thermal conductivity of the continuous phase (W/m·K), Re_d is the Reynolds number based on the droplet diameter and the relative velocity and Pr is the Prandtl number of the continuous phase.

The rate of vaporization of water by air is related to the gradient of the vapor pressure between the droplet surface and the main air stream and is given as follows:

$$\frac{dm_p}{dt} = A_p \frac{h_m}{R} \left(\frac{P_{sat}(T_p)}{T_p} - C \frac{p}{T_\infty} \right) \quad (15)$$

where h_m is the mass transfer coefficient (m/s), R is the universal gas constant (J/mol·K), P_{sat} is the saturated vapor pressure and C is the vapor concentration (kmol/m³).

The mass transfer coefficient is calculated from Sherwood number (Sh) correlation:

$$Sh = \frac{h_m d_p}{D_{va}} = 2.0 + 0.6 Re_d^{1/2} Sc^{1/3} \quad (16)$$

where D_{va} is the diffusion coefficient of vapor in the bulk (m²/s), Sc is the Schmidt number.

Therefore, the droplet mass is reduced according to the relation:

$$m_p(t + \Delta t) = m_p(t) - A_p \frac{h_m}{R} \left(\frac{P_{sat}(T_p)}{T_p} - C \frac{p}{T_\infty} \right) \Delta t \quad (17)$$

Now, the droplet temperature is updated based on the heat balance relation between the sensible heat change in the droplet and the convective and evaporative heat transfer between the droplet and the air:

$$m_p c_{pw} \frac{dT_p}{dt} = h A_p (T_\infty - T_p) + \frac{dm_p}{dt} h_{fg} \quad (18)$$

where h_{fg} is the latent heat of vaporization (J/kg).

3.2.3. Coupling between Air and Water Phases

Along with the droplet trajectory calculations, the heat, mass and momentum gained or lost by the droplet that follows the trajectory are also calculated and these quantities are incorporated as the source terms in the respective equations in the subsequent continuous phase calculations. The momentum, mass and heat exchanges are given as:

$$F = \sum \left(\frac{18\mu}{\rho_p d_p^2} \frac{C_D Re}{24} (u - u_p) + F_{other} \right) \frac{dm_p}{dt} \Delta t \quad (19)$$

$$M = \frac{\Delta m_p}{m_{p,0}} \dot{m}_{p,0} \quad (20)$$

$$Q = \left[\frac{m_{p,av}}{m_{p,0}} c_{pw} \Delta T_p + \frac{\Delta m_p}{m_{p,0}} \left(-h_{fg} + \int_{T_{ref}}^{T_p} c_{pv} dT \right) \right] \dot{m}_{p,0} \quad (21)$$

where F_{other} are other interaction forces, c_{pw} is the heat capacity of the water droplet (J/kg·K), c_{pv} is the heat capacity of the water vapor (J/kg·K), $\dot{m}_{p,0}$ is the initial mass flow rate of the droplet injection (kg/s), $m_{p,0}$ is the initial mass of the droplet (kg), $m_{p,av}$ is the average mass of the droplet in the cell (kg), T_{ref} is the reference temperature (K), ΔT_p is the change in temperature (K) and Δm_p is the change in mass of the droplet (kg).

3.3. Boundary Conditions

The flow is considered as incompressible [11] since the wind speed is varied from 1-5 m/s and is specified at the velocity inlet (S1). As this speed is not constant at every height, a power law for wind speed is adopted to create a velocity gradient. The wind profile power law [17] is a relationship between the wind speeds at one height, and

those at another. In order to estimate the wind speed at a certain height x , the relationship would be rearranged to:

$$u_x = u_r \left(\frac{z_x}{z_r} \right)^\alpha \quad (22)$$

where u_x is the wind speed (m/s) at height z_x (m), and u_r is the known wind speed at a reference height z_r . The exponent (α) is an empirically derived coefficient that varies dependent upon the stability of the atmosphere. For neutral stability conditions or terrain category, α is approximately 0.11 [19].

The outflow of the computational domain is specified as pressure outlet (S4) and is set at a reasonable distance to ensure that the solution near the wind catcher is not affected by the backflow conditions. The openings S2 and S3 in Fig. 2 are the inlet and outlet of the wind catcher, respectively.

Mist is introduced through eight conical injections which are defined and equally distributed circumferentially at position S5. Droplet evaporation has been considered with uniform droplet diameter distribution. The droplet diameter is assumed as 40 μm with a cone angle of 60°. The water is sprayed at a rate of 0.1 kg/s with a velocity of 45 m/s and temperature 298 K. The water droplets have been assumed to have inelastic collisions with the walls of the wind catcher. Hence, the reflected water droplet will have only tangential component of the momentum.

3.4. Domain Discretization and Solution

The grid consists of an unstructured volume mesh with rectangular meshes on the surface of the geometry. The total number of cells in the grid is 959,306 with 1,975,876 faces and 197,041 nodes. The maximum and minimum grid volumes are 0.000126 m^3 and 3.99 m^3 , respectively.

This solution was carried using the commercial CFD code FLUENT based on finite volume approach. Segregated solver which provides good robustness has been used. Reynold-Averaged Navier-Stokes (RANS) equations with the constitutive eddy viscosity realizable $k-\epsilon$ turbulence model is solved with Boussinesq hypothesis and discrete phase injections. The Semi-Implicit Method for Pressure-Linked Equations (SIMPLE) algorithm is chosen for pressure-velocity coupling and second order upwind discretization scheme is employed for spatial derivatives. The convergence criterion is set at 0.00001 residual for the continuity, and three momentums and energy scalar equations.

4. Results and Discussions

The simulations are performed for three wind velocities, ranging from 1 m/s to 5 m/s. The wind catcher is assumed to be situated in an open space in the present study. In summer, the weather in Abu Dhabi is extremely hot and humid. The ambient temperature may reach as high as 323K whereas the relative humidity can vary anywhere between 40-50%. The wind speed also can vary between 2 m/s to about 7 m/s. This presents a challenge in utilizing the evaporative cooling technique using a wind

catcher. The results at the wind speed of 3 m/s are discussed here as it is the average wind speed in summer. Fig. 3 shows the contour of velocity at a central plane parallel to the direction of the wind. It can be seen in Fig. 3 that the air velocity increases to about 7 m/s inside the column of the wind catcher. It is due to the additional evaporated mist that changes phase and expands within the wind catcher duct. At the exit, the air velocity reduces to about 4 m/s which is suitable for a semi-enclosed space. Fig. 4 represents the distribution of temperature in and around the wind catcher. It can be observed that due to the evaporative cooling, the hot air inside the wind catcher cools down to about 300 K. The reduction in temperature takes place near the walls in line with the liquid water injectors in the downward direction. The air at the center of the column takes relatively longer to cool down. The obtained average temperature at the exit of the wind catcher is about 303 K which means that a reduction of 10 K in the air temperature is achieved. This temperature of the air is considered comfortable in the semi-enclosed spaces. Fig. 5 shows the relative humidity distribution. An average relative humidity of about 44% is considered initially. As can be seen in the contour, the relative humidity reaches over 100% along the walls, implying that the air is fully saturated near the walls. The average relative humidity at the wind catcher exit is about 80% which is very high and beyond the comfort zone. However, as the air travels out of the wind catcher, the relative humidity further reduces after mixing with the less humid surrounding air. To avoid high humid conditions, there should be a provision to condense the water vapor which eventually reduces the relative humidity to the comfortable range. The most appropriate solution to the above problem would be to place a fine mesh made of hydrophilic material at the wind catcher exit which would help in condensing the excess water vapor from the air.

From the above results, it is evident that the behavior of the humid air inside the wind catcher column is highly non-uniform in both radial and axial directions. In the present study, the changes in humid air behavior at the center line of the wind catcher column are studied. Figs. 6-12 depicts the humid air behavior in terms of air velocity, static pressure, density, evaporated water mass, water mass fraction, relative humidity and temperature.

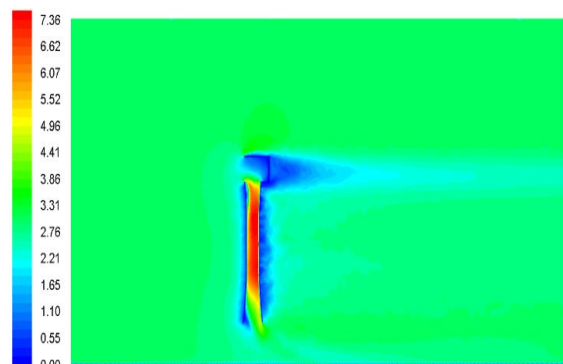


Fig. 3: Velocity contour at a wind speed of 3 m/s

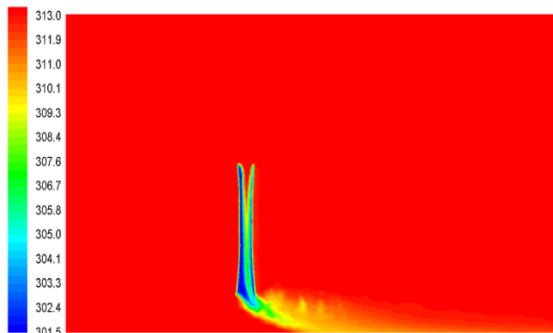


Fig. 4: Temperature contour at a wind speed of 3 m/s

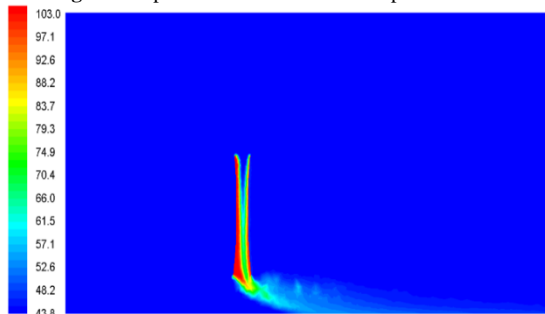


Fig. 5: Relative humidity contour at a wind speed of 3 m/s

Fig. 6 shows the variation of velocity from the entrance to the exit of the wind catcher for three inlet wind speeds ranging from 1-3 m/s. The trend in all the three cases is similar. Injection water through mist sprays result in absorption of water by the hot air making it heavier, denser and more humid. Consequently, the velocity increases due to the increase in negative buoyancy force. In addition, the converging-diverging design will also have an effect on the fluid velocity. The decrease in cross-sectional area at the middle also aids in velocity increase to satisfy the mass conservation. The velocities, then decrease as the dense air moves towards the wind catcher exit. As expected, the high inlet wind speeds resulted in high air velocities inside the wind catcher.

Fig. 7 shows the change of pressure from the entrance to the exit of the wind catcher column. The trend is opposite to that followed by the velocity in Fig. 6. An increase in velocity of the fluid particle would result in decrease in its pressure. High wind speeds produces lower static pressures inside the wind catcher. Nevertheless, the difference in pressure at the wind catcher exit is very small and can be considered negligible.

The fluctuation in density along the center line of the wind catcher is shown in Fig. 8. As water is sprayed in the incoming air, the air will become heavier due to absorption of liquid water droplets. Therefore, the density increases as the air flows towards the exit. High wind speeds bring in large volumes of air inside the wind catcher. Hence, as a result, more and more water can be absorbed resulting in high densities as shown in Fig. 8. The fluctuations are observed due to the fact that the absorption of water is not

uniform throughout the wind catcher column. The water is sprayed in the downward direction near the wall and has less pronounced effect at the center line. Hence, the variation in center line density is not smooth. Another thing to be noticed is that the density at the exit for inlet wind speeds higher than 3 m/s is similar.

Fig. 9 represents the mass flow rate of water that is evaporated along the center line. It can be seen that for low wind speeds, the rate of evaporation is more in the bottom half of the column. This is due to the increase in fluid velocities. On the other hand, the rate of evaporation is high in the upper half of the column for high wind speeds and it reduces as the flow travel towards the exit. This is due to the fact that significant absorption has already occurred which, consequently, cools down the air and reduces its temperature significantly and hence, the rate of evaporation is low. High wind speeds create a forced convection situation which ultimately affects the rate of evaporation, relative humidity and the air temperature.

In Fig. 10, the axial mass fraction of water vapor in the air at the center line of the wind catcher column is presented. The results show that mass fraction increases as the air flow reaches the wind catcher exit. High wind speeds capture more water vapor and hence, get saturated very quickly. Again, the fluctuations are due to the non-uniform behavior of the fluid particles inside the column.

Fig. 11 shows the axial relative humidity at the center line of the wind catcher column. The relative humidity reaches almost 100% for high wind speeds and about 70% for the lowest wind speed (1 m/s) as shown in the figure. These high values of relative humidity are out of comfortable criteria. Hence, as mentioned earlier, provisions have to be made in order to capture the water vapor from the air without increasing the air temperature. A mesh made of hydrophilic material can be used at the wind catcher exit to capture the water vapor from the air.

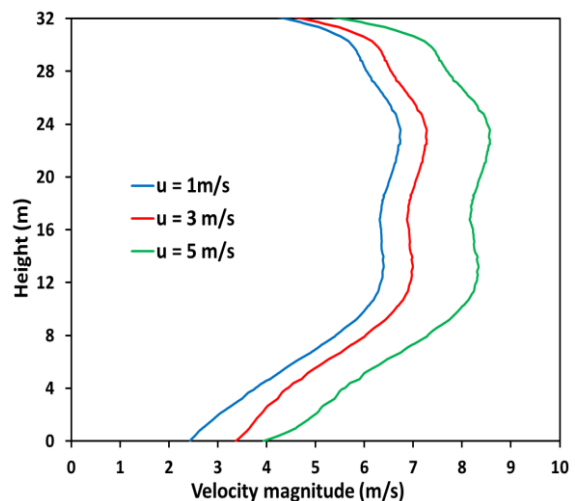


Fig. 6: Variation of air velocity from entrance to exit

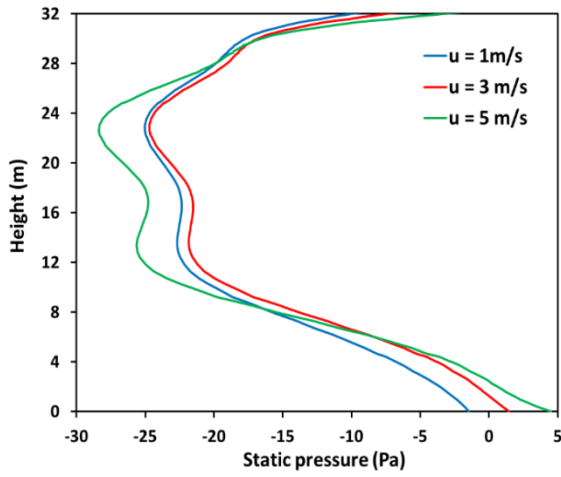


Fig. 7: Variation of pressure from entrance to exit

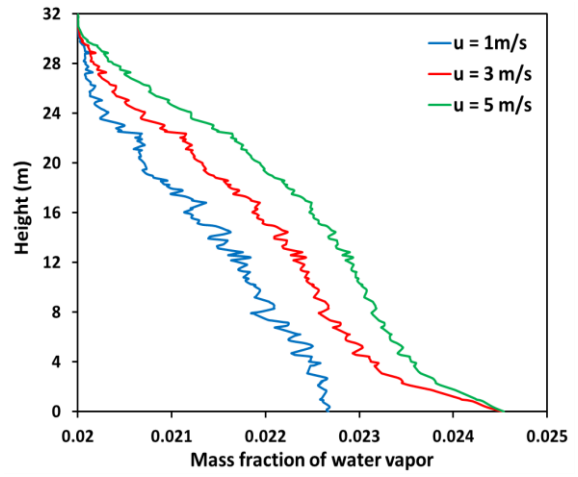


Fig. 10: Variation of water mass fraction from entrance to exit

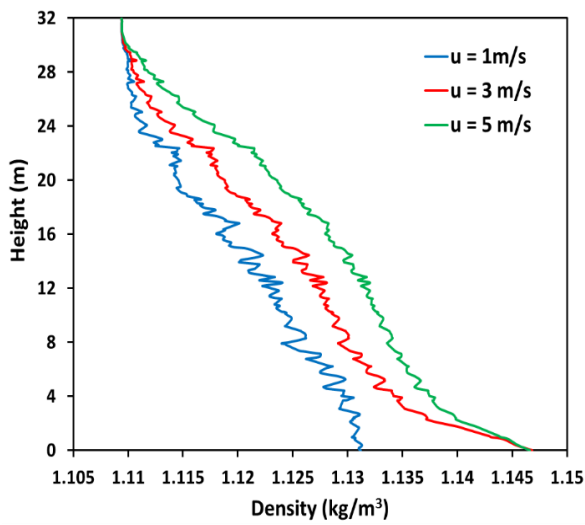


Fig. 8: Variation of density from entrance to exit

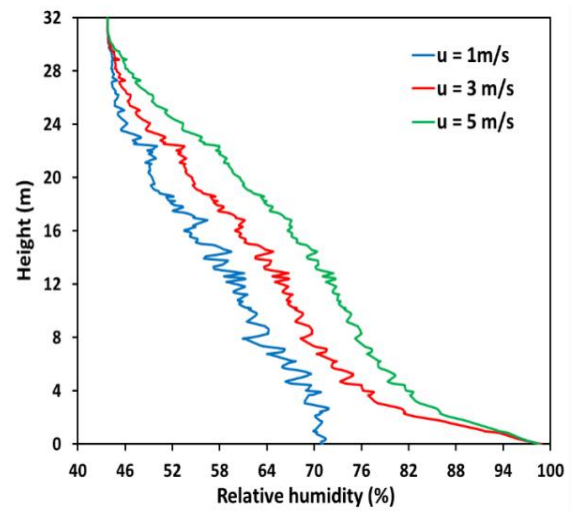


Fig. 11: Variation of relative humidity from entrance to exit

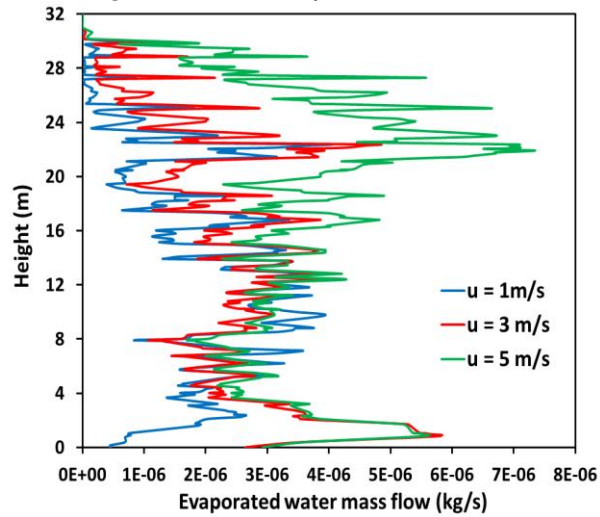


Fig. 9: Variation of evaporated water mass from entrance to exit

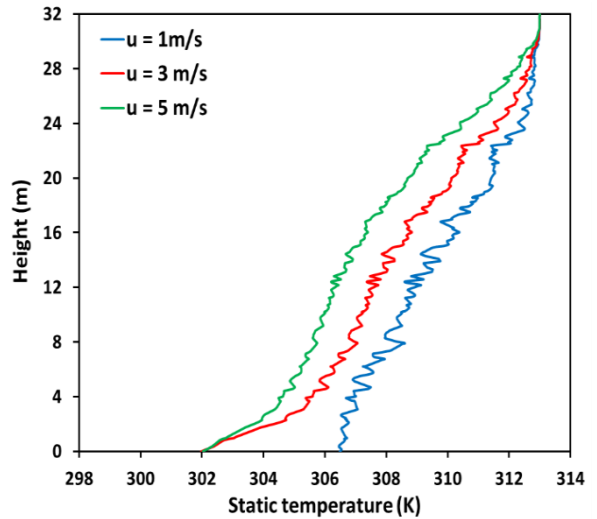


Fig. 12: Variation of temperature from entrance to exit

Table 1: Parameters at various wind speeds

Wind speed (m/s)	1	3	5
Pressure (Pa)	-1.138	-0.122	1.228
Density (kg/m ³)	1.136	1.142	1.143
Velocity (m/s)	2.86	3.357	3.81
Temperature (K)	304.83	303.28	302.9
Water mass fraction	0.0233	0.0241	0.0242
Relative humidity (%)	81.61	91.18	93.02

The variation in the air temperature for different velocities is shown in Fig. 12. The results show that high wind speeds resulted in low exit temperatures. The temperature is reduced significantly to 302K, which is about 11K reduction. This can be attributed to the absorption of heat during evaporative cooling process.

In addition to the humid air behaviour along the centre line of the wind catcher column, the state of the humid air at the exit is critical to the overall performance of the wind catcher. The parameters discussed above are averaged over the cross-sectional area at the wind catcher exit and are listed in Table 1. It can be observed that the pressure, density, velocity, water mass fraction and relative humidity increase with increasing inlet wind speeds. On the other hand, the air temperature decreases with increasing inlet wind speeds. This emphasizes the fact that the performance of the wind catcher is greatly influenced by the ambient wind speeds.

The main parameters that are to be controlled in order to achieve desirable outlet temperature are mass flow rate of water, the cone angle, velocity of the spray, diameter of the liquid droplet etc. In the current study, the mass flow rate of water is chosen as 0.1 kg/s such that the temperature is reduced by 10 K. The spray angle of 60° is chosen since results in good distribution of water droplets. The water jet velocity is assumed as 45 m/s since at this velocity fine mist droplets are formed. All the aforementioned parameters are important. However, in order to correctly predict the outlet temperature further simulations is required by varying the above parameters individually.

5. Conclusions

In the present study, a numerical model has been developed to simulate the three sided wind catcher at the Masdar City, Abu Dhabi. The performance of the wind catcher at different wind speeds is analyzed quantitatively. The effect of wind speeds on the velocity, pressure, density, rate of evaporation, water mass fraction, relative humidity and temperature has been studied. The results obtained showed that spraying of liquid water in hot air has significant effect on the aforementioned parameters. The wind catcher is capable of reducing the temperature by 10-12 K at the peak of its performance while keeping the air velocity in comfort range. However, the relative humidity obtained is very high and out of comfortable zone. This is because of the ambient relative humidity which is already high in summer.

The results shows that the higher wind speeds show better performance as they create a forced convection condition resulting in high evaporative cooling. The air

velocities inside the wind catcher column increases first due to absorption of the water and then decreases as the air flow proceeds toward the exit as opposed to pressure which increases as the flow moves toward the exit. Due to water absorption, the air becomes moist and heavier and hence, the density increases. Mass fraction of water in the air and consequently, the relative humidity are increased with decrease in the height of the column. The air temperature decreases significantly due to the heat absorption in evaporative cooling.

The only problem associated with the current wind catcher is the exit relative humidity which is beyond the comfort criteria. The most appropriate solution would be to use a mesh made of hydrophilic material that can adsorb the water vapour from the air without increasing its temperature. It is just an idea and more work is needed in order to determine its usefulness and the additional costs it incurs. It is also important to consider the annual weather data of Masdar City. Some of these data are found elsewhere of the authors work [20]. Additionally, validated atmospheric boundary layer wind tunnel flow simulations commensurated with density-, pressure-, temperature-, and humidity-velocity correlation renders the establishment of better guidelines for wind catcher development [21]. This is a research study on its own that will be considered in a future development of the present work. Further investigations based on various other parameters, like the inlet air temperature, relative humidity, the spray water temperature, droplet diameter, spray velocity and liquid water mass flow rate are required in order to assess and optimize the performance of the wind catcher for the climatic conditions of Abu Dhabi.

Acknowledgments

The present study was supported by the Government of Abu Dhabi to help fulfil the vision of the late President Sheikh Zayed Bin Sultan Al Nahyan for sustainable development and empowerment of the UAE and humankind.

References

- [1] A. Al-Salaymeh and M.R. Abdelkader, "Efficiency of free cooling technique in air refrigeration systems," *Jordan Journal of Mechanical and Industrial Engineering*, vol. 4(6), pp. 711-724, December 2010.
- [2] M. Younis, K. Ghali, and N. Ghaddar, "Performance evaluation of the displacement ventilation combined with evaporative cooled ceiling for a typical office in Beirut," *Energy Conversion and Management*, vol. 15(105), pp. 655-664, November 2015.
- [3] M. Ali, V. Vukovic, N.A. Sheikh, and H.M. Ali, "Performance investigation of solid desiccant evaporative cooling system configurations in different climatic zones," *Energy Conversion and Management*, vol. 30(97), pp. 323-339, June 2015.
- [4] C. Karakatsanis, M.N. Bahadori, and B.J. Vickery, "Evaluation of pressure coefficients and estimation of air flow rates in buildings employing wind towers," *Solar Energy*, vol. 37(5), pp. 363-374, December 1986.
- [5] A.A. Badran, "Performance of cool towers under various climates in Jordan," *Energy and Buildings*, vol. 35(10), pp. 1031-1035, November 2003.

- [6] A.A. Elmualim, and H.B. Awbi, "Wind tunnel and CFD investigation of the performance of "Windcatcher" ventilation systems," *International Journal of ventilation*, vol. 1(1), pp. 53-64, June 2002.
- [7] S. Kirk, and M. Kolokotroni, "Windcatchers in modern UK buildings: experimental study," *International Journal of ventilation*, vol. 3(1), pp. 67-78, June 2004.
- [8] Y. Su, S.B. Riffat, Y.L. Lin, and N. Khan, "Experimental and CFD study of ventilation flow rate of a Monodraught™ windcatcher," *Energy and Buildings*, vol. 40(6), pp. 1110-1116, December 2008.
- [9] M.N. Bahadori, "Pressure coefficients to evaluate air flow pattern in wind towers," In *International Passive and Hybrid Cooling Conference*, American Section of the International Solar Energy Society, Miami Beach, Florida, pp. 206-210, November 1981.
- [10] A.R. Dehghani-sanij, M. Soltani, and K. Raahemifar, "A new design of wind tower for passive ventilation in buildings to reduce energy consumption in windy regions," *Renewable and Sustainable Energy Review*, vol. 42, pp. 182-195, February 2015.
- [11] L. Li, and C.M. Mak, "The assessment of the performance of a windcatcher system using computational fluid dynamics," *Building and environment*, vol. 42(3), pp. 1135-1141, March 2007.
- [12] I. Janajreh and S. Emil, "Large eddy simulation of wind loads on a low-rise structure and comparison with wind tunnel results," *Applied Mechanics and Materials*, vol. 152, pp. 1806-1813, January 2012.
- [13] I. Janajreh, "CFD Analysis of Wind Loads on Permeable Low-Rise Structures," *Applied Mechanics and Materials*, vol. 152, pp. 1814-1820, January 2012.
- [14] V. Kalantar, "Numerical simulation of cooling performance of wind tower (Baud-Geer) in hot and arid region," *Renewable Energy*, vol. 34(1), pp. 246-254, January 2009.
- [15] H. Saffari, and S.M. Hosseinnia, "Two-phase Euler-Lagrange CFD simulation of evaporative cooling in a Wind Tower," *Energy and Buildings*, vol. 41(9), pp. 991-1000, September 2009.
- [16] I. Janajreh, K. Adouane and M. Hussain, "Wind Catcher and Trans-evaporative Cooling Residential Integration in Arid Region," *Int. J. of Thermal & Environmental Engineering*, Issue 1, vol. 14(1), 2017.
- [17] W.E. Ranz, and W.R. Marshall, "Evaporation from drops," *Chemical Engineering Progress*, vol. 48(3), pp. 141-146, March 1952.
- [18] E.W. Peterson, and J.P. Hennessey Jr., "On the use of power laws for estimates of wind power potential," *Journal of Applied Meteorology*, vol. 17(3), pp. 390-394, March 1978.
- [19] S.A. Hsu, E.A. Meindl, and D.B. Gilhousen, "Determining the power-law wind-profile exponent under near-neutral stability conditions at sea," *Journal of Applied Meteorology*, vol. 33(6), pp. 757-765, June 1994.
- [20] I. Janajreh, I. Talab, "Wind data collection and analyses at Masdar City for wind turbine assessment," *Int J. Ther Envi. Eng.*, vol. 1, 2010
- [21] MR Hajj, IM Janajreh, HW Tieleman, TA Reinhold, "On frequency-domain analysis of the relation between incident turbulence and fluctuating pressures," *Journal of wind engineering and industrial aerodynamics*, vol 69, 1997

Modeling and Simulation of Shrouded Horizontal Axis Wind Turbine Using RANS Method

C. Ghenai^{a*}, T. Salameh^b, I. Janajreh^b

^a Sustainable and Renewable Energy Engineering Department, College of Engineering- University of Sharjah, Sharjah 27272, United Arab Emirates

^b Mecanical Engineering Program, Khalifa University of Science and Technology, Masdar Institute- Abu Dhabi, 54224, United Arab Emirates

Abstract

The vast deployment of wind energy leads to its technical maturity and cost reduction that compete with natural gas. Low wind regions can be also targeted when shrouded or optimally designed turbine is utilized. The objective of the present study is to assess the performance of the shrouded Horizontal Axis Wind Turbine (HAWT) numerically subjected to low wind speed. The goal is to develop wind energy technologies that can maximize the power extracted from the turbine under low wind conditions. Three blades horizontal axis wind turbine surrounded with a shroud was tested in the present study. The Reynolds Averaged Navies-Stokes (RANS) modeling approach and finite volume numerical method was used to solve the governing equations. These equations are based on the equations of conservation of mass, momentum and turbulence scalars ($k-\epsilon$). The flow field around the wind turbine and inside the shroud was resolved. The induction factor was obtained from the computed velocity profiles. The turbine power coefficient (C_p) was determined using the induction factor. A comparison between the C_p with and without shroud at different tip speed ratios is presented in the present paper. The results show that the shrouded turbines can generate quadruple of the power of the non-shrouded baseline HAWT.

© 2017 Jordan Journal of Mechanical and Industrial Engineering. All rights reserved

1. Introduction

Nearly eighty two percent of the world energy demand (electricity generation, transportation, buildings, and industrial applications) is provided through the non-renewable and unsustainable fossil fuels, i.e., coal, oil and natural gas. Renewable and clean energy systems continue to evolve and deploy to mitigate the problems of climate change (high GHS emissions from combustion of fossil fuels), energy security, the raising future energy demand, and the depletion of fossil fuel resources (oil, natural gas and coal) [1]. A comparison between the resource intensities (material, area, energy, CO_2 and capital intensities related to the construction of renewable energy systems) and operational parameters (system efficiency, capacity factor, and lifetime) of fossil fuel, renewable and nuclear power systems has been presented by Ghenai and Janajreh [1]. Among these renewable energy technologies, wind energy will continue to play an important role in the future. According to the World Wind Energy Association, the world has seen a new record (63.69 GW) in its installations in 2015 and nearly covering 3% of the global electricity supply in 2012 [2]. It also observed global growth rate of 17.2 % in 2015. The world total wind capacity reached 435 GW in 2015, with 46.2%, 33%, 29%, and 25.45 increases in Brazil, Poland, China, and Turkey, respectively (most dynamic countries with the strongest

growth rates in 2015). This growth can be accelerated in the future should renewable energy policies continue to emerge from countries around the world [3].

While wind intermittency and low speed reduce turbine capacity factor, shrouded wind turbine can mitigate this loss and help in increasing wind energy deployment. This technology can be adopted to generate higher power in regions characterized with low speed conditions. The turbine is enclosed in shroud or duct that will allow the turbine to operate at higher efficiencies and thereby capacity compared to non-shrouded turbine. The shroud is used to increase the flow velocity or the volume of airflow around the turbine. More power is then generated with greater return in investment.

Hjort and Larsen [4] investigated the design requirement for Diffuser Augmented Wind Turbine (DAWT) rotor to efficiently convert the available energy shaft energy. Three different configurations were studied: bare propeller (HAWT), classical diffuser augmenter wind turbine (DAWT) and high performance multi element DAWT. The results showed that the DAWT rotors can successfully convert the available energy to shaft energy if the swirl and axial loading distribution were selected correctly.

Bala [5] performed experimental and numerical study of diffuser augmented wind turbine. The wind turbine power performance was evaluated using the power coefficient values. The experimental date showed

* Corresponding author e-mail: cghenai@sharjah.ac.ae.

improvements for the electrical power values, resulting in an average of 90% in the power coefficient and the more pronounced enhancement was obtained at low wind speed values [5].

A shrouded wind turbine generating high output power with wind lens technology was investigated by Yuji Ohya and Takahi Karasudani [6]. They showed that the shrouded wind turbine with brimmed diffuser augmented the power by 2-5 compared to bare wind turbine for given wind speed and rotor diameter. This is due to low-pressure region, due to the strong vortex formation behind the broad brim leading to draw more mass flow to the wind turbine inside the diffuser shroud.

Kosasih and Tondelli [7] focused, in their study, on the effects of diffuser shape and geometries, and blade airfoils on the wind turbine performance enhancement. Three different geometrical features: straight diffuser, nozzle-diffuser combination, and brimmed diffuser combination have been investigated. The tests confirmed that placing the micro turbine model inside a shroud can substantially improve its performance. The results showed that the diffuser shroud improves the performance by 60% compared to the bare turbine. The nozzle-diffuser enhancement was 63% slightly better than diffuser only. The findings from their work suggested that shrouding micro wind turbine not only improves its performance, but also provide guidelines on the design of the diffuser geometrical parameters (L/D) and/or (H/D) with a customized performance curve.

Hu and Wang [8] used a self-adaptive flange for the wind turbine shroud. The self-adaptive flange can maintain the advantages of the flanged diffuser at wind velocities lower than the rated velocity and reduce the wind loads acting on the diffuser and blades at higher wind velocities. Numerical results show that the wind load acting on the total flanged diffuser can be reduced by about 35% at 60 m/s due to the reconfiguration of the self-adaptive flange.

Aniket *et al.* [9] investigated the flow and performance of shrouded turbines using Reynolds Averaged Navier-Stokes (RANS) equations. Different shroud geometries were evaluated for their augmentation of mass flow through the turbine. The results showed an augmentation ratios of up to 1.9 can be achieved with shrouded turbines.

El-Zahaby *et al.* [9-10] used 2D axisymmetric CFD model of flanged diffuser as a casing for small wind turbines to increase the generated power. The numerical simulation shows the creation of vortices behind flange that cause pressure drop which increases mass flow rate through the diffuser leading to an increase in the generated power.

The main objective of the present study is to perform numerical simulations to test the performance of shrouded horizontal axis wind turbine under the low speed wind conditions of the Arabian Peninsula eastern coastline as indicated elsewhere with an average annual wind at the borderline cut-in wind turbine speed of 4.5 m/s [11]. The goal is to develop wind energy technologies that can maximize the power extracted from the turbine under low wind conditions and to accelerate the penetration of wind energy technologies in the Arabian Peninsula.

2. Governing Equations

A steady state solution is sought for the rotating turbine. This can be achieved through a "rotating reference frame" formulation in which the turbine rotor rotation is assigned a specific rotating speed without need to temporally trace its time advancement. This can drastically reduce the computational time and remove the burden in carrying sensitivity studies. Although the details of the flow due to the rotating blade against the outer domain and there interaction in generated vorticity trails will be undermined, nevertheless an average of these phenomena is captured at lower cost than the lengthy real time transient calculation. These latter real time calculations follow transient arbitrary Lagrangian Formulation, which involves domain movement and mesh sliding as appears in a previous work by the present authors [12], are limited to smaller flow domain to bring more flow insight or its physics validation. The equations of conservation of mass, momentum, and the two scale turbulence equations (turbulent kinetic energy k and the dissipation of the kinetic energy ϵ) are solved to predict the flow field around the wind turbine [13-14]. The time averaged gas phase equations for steady turbulent flow are:

$$\frac{\partial}{\partial x_j} (\rho u_i \Phi) = - \frac{\partial}{\partial x_i} \left(\Gamma_\Phi \frac{\partial \Phi}{\partial x_i} \right) + S_\Phi \quad (1)$$

where Φ is the dependent variable that can represent the velocity u_i , the turbulent kinetic energy k , and the dissipation rate of the turbulent kinetic energy ϵ . The governing equations in steady state form are given such that, the conservation of energy is written as:

$$\frac{\partial \rho u_i}{\partial x_i} = 0 \quad (2)$$

where ρ is the density, u_i are the three velocity components. The momentum equation is written as:

$$\frac{\partial (\rho u_i u_j)}{\partial x_j} = - \frac{\partial \bar{P}}{\partial x_i} + \frac{\partial (\bar{t}_{ij} + \tau_{ij})}{\partial x_j} \quad (3)$$

where \bar{p} is the static pressure and \bar{t}_{ij} is the viscous stress tensor defined as:

$$\bar{t}_{ij} = \mu \left[\left(\frac{\partial \bar{u}_i}{\partial x_j} + \frac{\partial \bar{u}_j}{\partial x_i} \right) - \frac{2}{3} \frac{\partial \bar{u}_k}{\partial x_k} \delta_{ij} \right]$$

$$\delta_{ij} = 1 \text{ if } i = j \text{ and } \delta_{ij} = 0 \text{ if } i \neq j$$

τ_{ij} is the average Reynolds stress tensor defined and modeled using the eddy viscosity turbulence model as:

$$\tau_{ij} = -\rho \overline{u_i u_j}$$

$$\tau_{ij} = \mu_t \left[\left(\frac{\partial \bar{u}_i}{\partial x_j} + \frac{\partial \bar{u}_j}{\partial x_i} \right) - \frac{2}{3} \frac{\partial \bar{u}_k}{\partial x_k} \delta_{ij} \right] - \frac{2}{3} (\overline{\rho k} \delta_{ij})$$

where k is the average turbulent kinetic energy defined as:

$$\bar{k} = \frac{1}{2} \overline{u_i u_i}$$

and μ_t is the turbulent eddy viscosity expressed in terms of k and the dissipation rate (ϵ) as:

$$\mu_t = c_\mu \frac{\rho \overline{k^2}}{\overline{\varepsilon}}$$

where C_μ is constant ($C_\mu = 0.09$) and $\overline{\varepsilon}$ is the average dissipation rate of the turbulent kinetic energy and defined as:

$$\overline{\varepsilon} = \nu \frac{\partial \overline{u_i} \partial \overline{u_i}}{\partial x_j \partial x_j}$$

where ν is the kinematic viscosity. The two scalar transport equations for each of the Turbulence Kinetic Energy (k) and its dissipation are written as (ε):

$$\frac{\partial(\overline{\rho k u_i})}{\partial x_i} = \frac{\partial \left[\left(\mu + \frac{\mu_t}{\sigma_k} \right) \frac{\partial \overline{k}}{\partial x_j} \right]}{\partial x_j} + G_k - \overline{\rho \varepsilon} \tag{4}$$

where $\sigma_k = 1$ and G_k is the production of the turbulent kinetic energy defined as:

$$G_k = \mu_t \left[\left(\frac{\partial \overline{u_i}}{\partial x_j} + \frac{\partial \overline{u_j}}{\partial x_i} \right) \frac{\partial \overline{u_i}}{\partial x_j} - \frac{2}{3} \frac{\partial \overline{u_i}}{\partial x_j} \delta_{ij} \left[\mu_t \frac{\partial \overline{u_k}}{\partial x_i} + \overline{\rho k} \right] \right]$$

$$\frac{\partial(\overline{\rho \varepsilon u_j})}{\partial x_j} = C_{\varepsilon 1} \frac{\overline{\varepsilon}}{k} G_k + \frac{\partial \left[\left(\mu + \frac{\mu_t}{\sigma_\varepsilon} \right) \left(\frac{\partial \overline{\varepsilon}}{\partial x_j} \right) \right]}{\partial x_j} \tag{5}$$

$$C_{\varepsilon 2} \overline{\rho} \frac{\rho_2}{k}$$

where $C_{\varepsilon 1}=1.44$, $C_{\varepsilon 2}=1.92$, and $\sigma_\varepsilon=1.3$ are the tuning model constants.

3. Geometry, Bounadar Conditions, Mesh and Numerical Method

Fig. 1 shows a schematic of the three dimensional wind turbine. The wind turbine blade characteristics are summarized in Table 1. For the boundary conditions, the air enters from the left boundary at a velocity U_{wu} (Inlet flow – velocity inlet). The computational domain has a cylindrical shape as shown in Fig. 1 (symmetry). The air exits the computational domain from the right side (Outflow). The rotor is modeled as rotating immersed frame with an angular velocity ω [rad/s] which remove the hassle of seeking transient analyses. Thus, an averaged steady state solution is sought. The geometry of the shroud is shown in Fig. 2. The shroud characteristics are summarized in Table 1.

A Quality mesh was generated for the shrouded and unshrouded turbines. The number of nodes selected for the wind turbine simulation study was 188,000. A grid independent study was performed with three different meshes (coarse mesh with 94,000 nodes, medium mesh with 188,000 nodes and fine mesh with 365,000 nodes) and the results of the simulation were compared. The difference between the simulations results obtained with medium and fine mesh was less than 1.5%. Based on this grid independent study, the medium mesh was selected for this numerical study. A control volume based finite difference method is used in order to solve a system of partial differential equations governing the conservation of mass, momentum, and turbulent flow. In this CFD analysis, the SIMPLER algorithm is used to solve explicitly for the velocity and pressure fields. SIMPLER (revised version of SIMPLE algorithm) is a semi-implicit method used as a numerical procedure for solving the Navier-Stokes equations [15-17]. The SIMPLE algorithm uses a relationship between velocity and pressure corrections (pressure-velocity coupling algorithm) to enforce the continuity equation (mass conservation) and to obtain the pressure field.

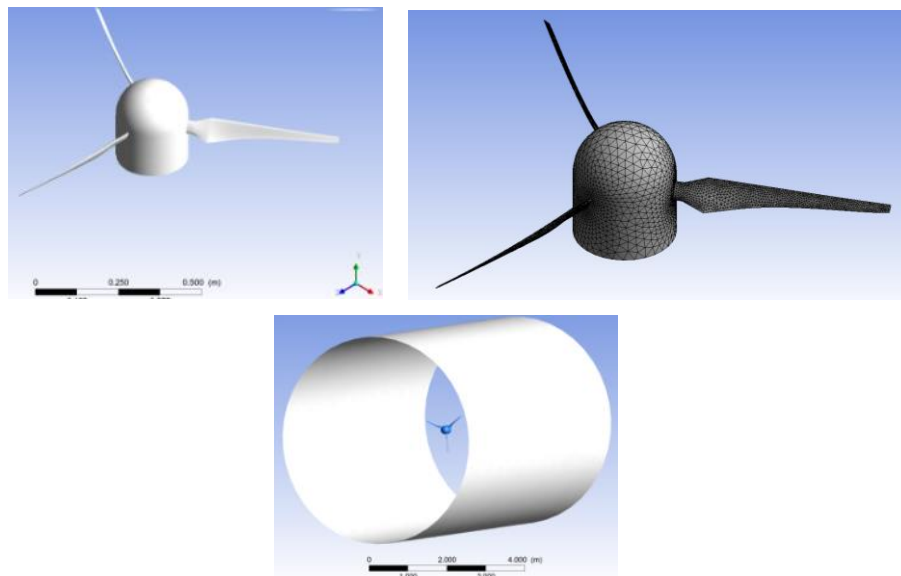


Figure 1: Unshrouded wind turbine geometry, mesh and computational domain

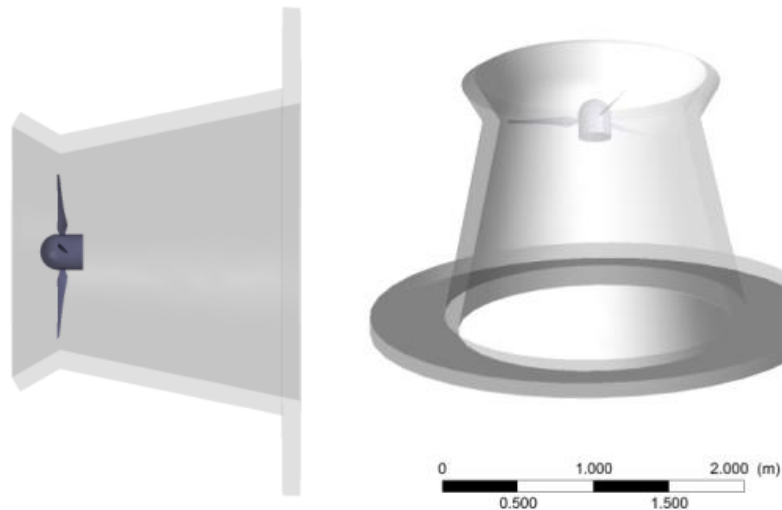


Figure 2: Shrouded Wind Turbine Geometry

Table 1: Wind turbine and shroud characteristics

Blade - airfoil	SG6043
Blade length (m)	0.5
Throat diameter D (m)	1.17
Rotor diameter	1.16
Diffuser Length L (m)	1.46
Diffuser angle	12°

4. Performance Characteristics of the Wind Turbine

4.1. Unshrouded Baseline Wind Turbine

The efficiency of the wind turbine represented by the power coefficient, C_p , and the power extracted from the turbine, P_t , are used as the performance characteristics of the wind turbine. The power coefficient is given by:

$$C_p = \frac{P_t}{P_{wind}} = \frac{T \cdot \omega}{P_{wind}} \quad (6)$$

where T is the torque (N.M), ω is the angular velocity of the turbine (rad/s), and P_{wind} is the maximum available power in the wind (W). The wind power is given by:

$$P_{wind} = 0.5 \rho A U_w^3 \quad (7)$$

where ρ is the air density (kg/m^3), A is the rotor diameter (m^2) and U_w is the wind speed.

The C_p is also given [12] by:

$$C_p = 4 a (1 - a)^2 \quad (8)$$

where the induction factor a is given by:

$$a = 1 - \frac{U_{wrot}}{U_{wu}} \quad (9)$$

$$U_{wrot} = \frac{1}{2} (U_{wu} + U_{wd}) \quad (10)$$

where U_{wrot} , U_{wu} , and U_{wd} are the air velocities at the rotor, up-stream and down-stream of the turbine blades, respectively.

4.2. Shrouded Wind Turbine

The power coefficient of the shrouded wind turbine [6, 18, 19] is given by:

$$C_p = \epsilon_L \mu 4 \bar{a} (1 - \bar{a})^2 \quad (11)$$

$$\epsilon_L = \frac{A_{out}}{A_{rot}} \quad (12)$$

$$\mu = \frac{U_{out}}{U_{wu}} \quad (13)$$

$$\bar{a} = 1 - \frac{U_{wd}}{U_{wu}} \quad (14)$$

$$C_{p)Diffuser} = \mu 4 \bar{a} (1 - \bar{a})^2 \quad (15)$$

where A_{out} and A_{rot} are the surface areas at the exit from the shroud and at the rotor (see Fig. 3), ϵ_L and μ are the area ratio and the back pressure coefficient, and $C_{p)Diffuser}$ is the power coefficient due to the diffuser.

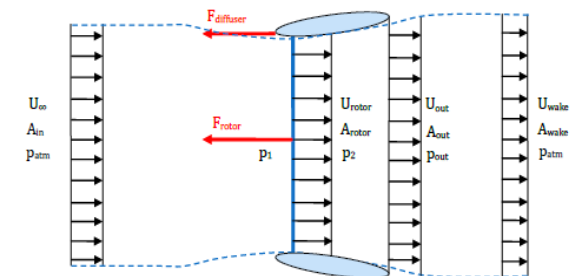


Figure 3: Control volume for shrouded turbine [17-18]

5. Results

The simulation results of the unshrouded and shrouded turbine are evaluated and presented. The effect of turbine tip speed ratio ($\text{TSR} = 4 - 10$) on the power extracted and the C_p is investigated in the present study. The wind speed at the inlet of the computational domain was set to as low as $U_{wu} = 4 \text{ m/s}$ and the corresponding rotational speed ω (rad/s) of the turbine was determined from the tip speed ratio equation ($\text{TSR} = \omega \cdot R / U_{wu}$, where R is the blade length). Fig. 4 shows the velocity magnitude of the air flow at the position of the unshrouded wind turbine ($y = 0$) and behind the wind turbine ($y = 0.1, 0.2, 0.3, 0.4$ and 0.5

m). The wind approached the the turbine with a wind speed of U_{wu} . The wind speed decreases as it approaches the turbine before it passes through the rotor plane. The axial velocity deficit is the amount of decrease in the freestream velocity. The induction factor a given by the equation 9 represents the fraction by which the axial component of the velocity is reduced. The axial component of the velocity reduces further after passing the rotor plane ($y = 0.1, 0.2, 0.3, 0.4$ and 0.5 m) as shown in Fig. 4. There is a pressure drop across the rotor plane when the air passes the rotor plane. Downstream the rotor plane, the pressure is recovered and back to the atmospheric pressure where the average air velocity is U_{wd} as shown in Fig. 5. This average air velocity downstream the wind turbine and where the

pressure is recovered back to the atmospheric pressure is used to calculate the induction factor using the equations 9 and 10. The C_p is then calculated using the equation 8 for the unshrouded turbine. The variation of the C_p and a with the tip speed ratio are show in Fig. 6. The results show a maximum value for C_p of 0.38 at a tip speed ratio between 7 and 8. The value of C_p decreases to 0.2 at low and high tip speed ratio (TSR = 4 and TSR = 10). The induction factor a for the range of TSR tested in the present study was between 0.06 and 0.13. The maximum value for the induction factor $a = 0.13$ was obtained at TSR = 7 and is less than the maximum theoretical value of induction factor of $a = 1/3$ (Betz limit).

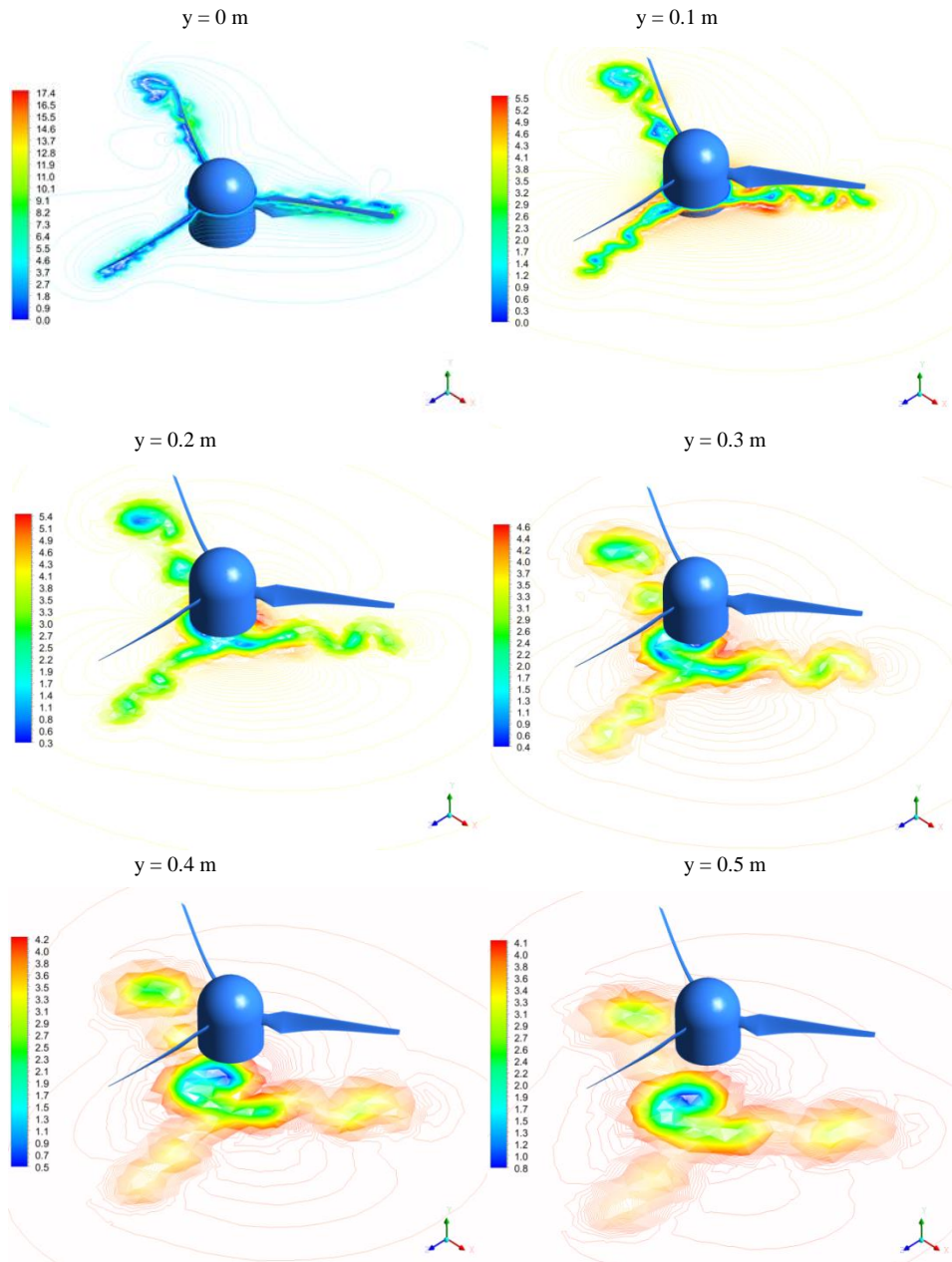


Figure 4: Velocity magnitude at the rotor plane and at different stations behind the wind turbine: Unshrouded Turbine, $U_{wu} = 4$ m/s and TSR = 7

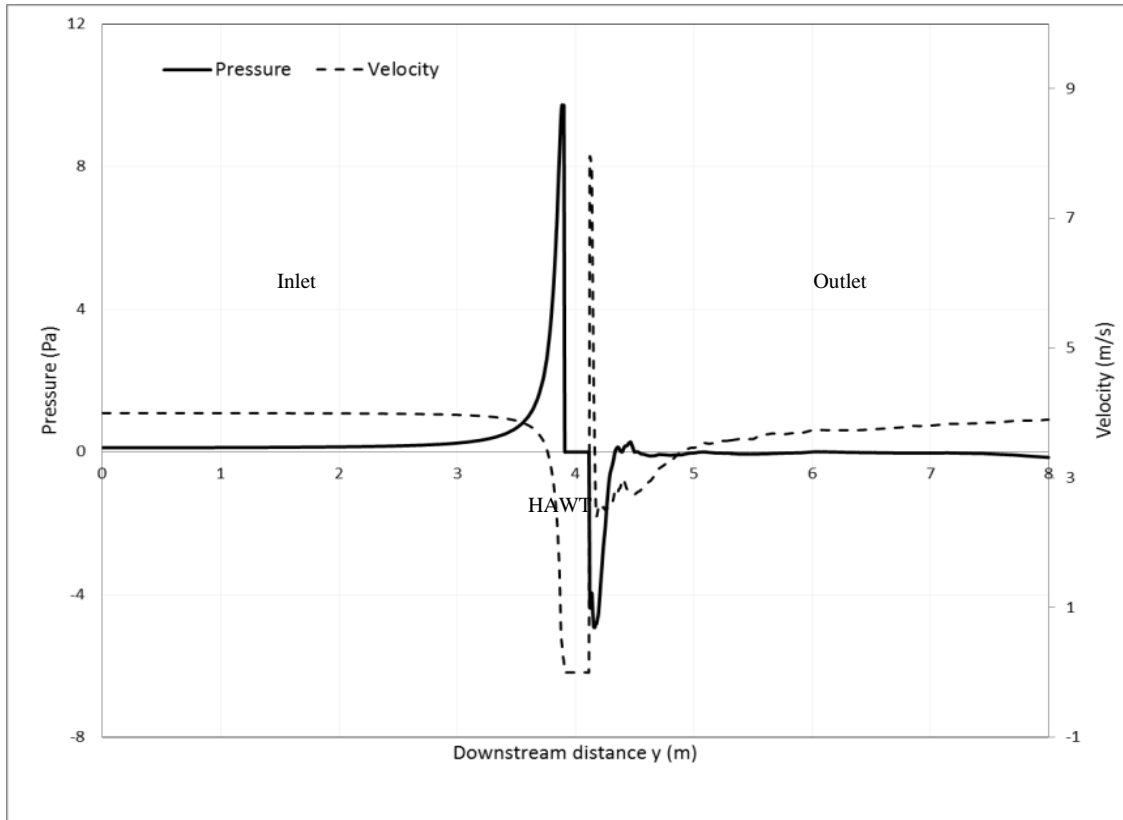


Figure 5: Axial variation of the pressure and velocity magnitude for the Unshrouded Wind Turbine ($U_{wu} = 4$ m/s, and $TSR = 7$)

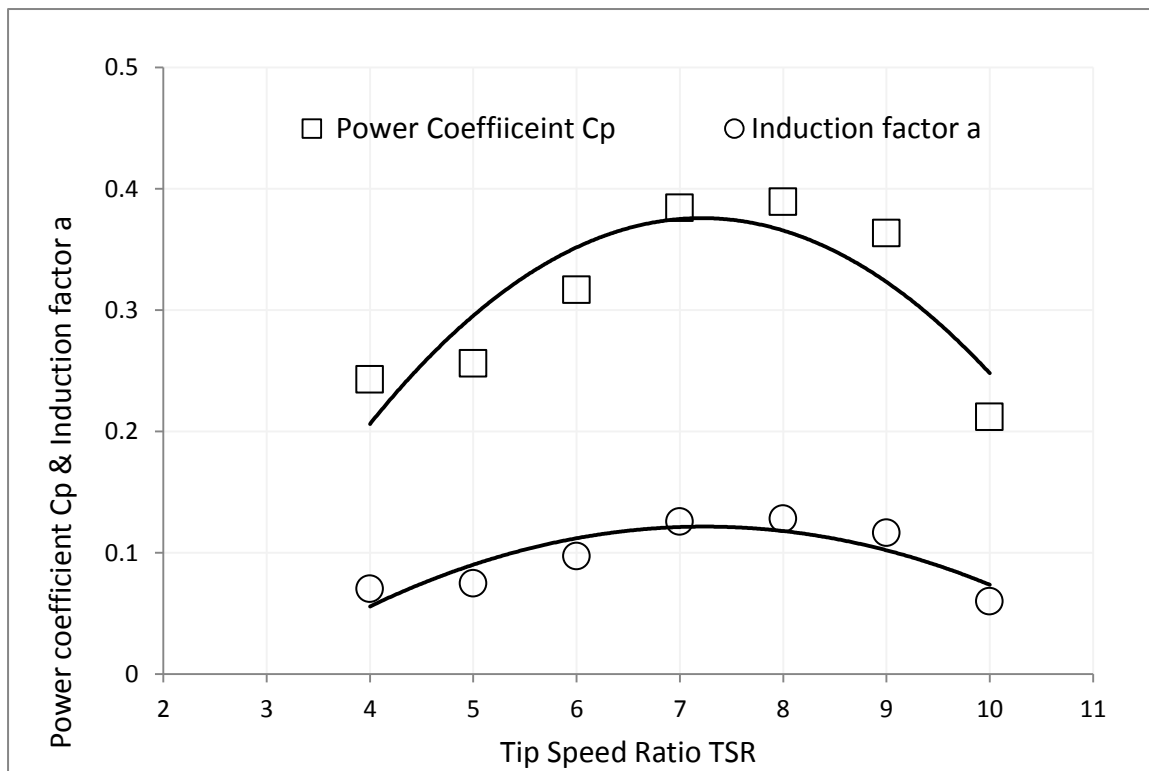


Figure 6: Power coefficient C_p and induction factor a for the unshrouded wind turbine

For the shrouded turbine, the equations 11-14 are used to calculate the C_p . The area ratio, ϵ_L , was calculated using the selected geometry of the shroud (A_{out}/A_{rot}). The back pressure coefficient, μ , was calculated using equation 13 based on the average wind speed at the exit of the shroud U_{out} . Figs. 7 and 8 show the velocity magnitude in the X-Y and X-Z planes respectively; for

the shrouded wind turbine. The velocity contour results show clearly an increase (1.8 times the freestream velocity $U_{wu} = 4 \text{ m/s}$) of the wind speed inside the shrouded turbine. This will draw more mass flow inside the shrouded wind turbine leading to an increase in the shaft power, i.e., the power extracted from the turbine.

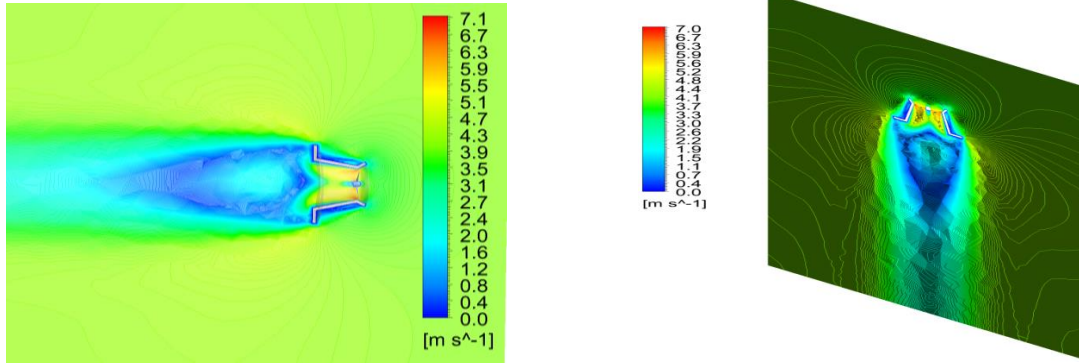


Figure 7: Velocity magnitude contours in the X-Y plane for the shrouded turbine ($U_{wu} = 4 \text{ m/s}$ and $TSR = 7$)
 $y = -0.05 \text{ m}$ $y = 0 \text{ m}$

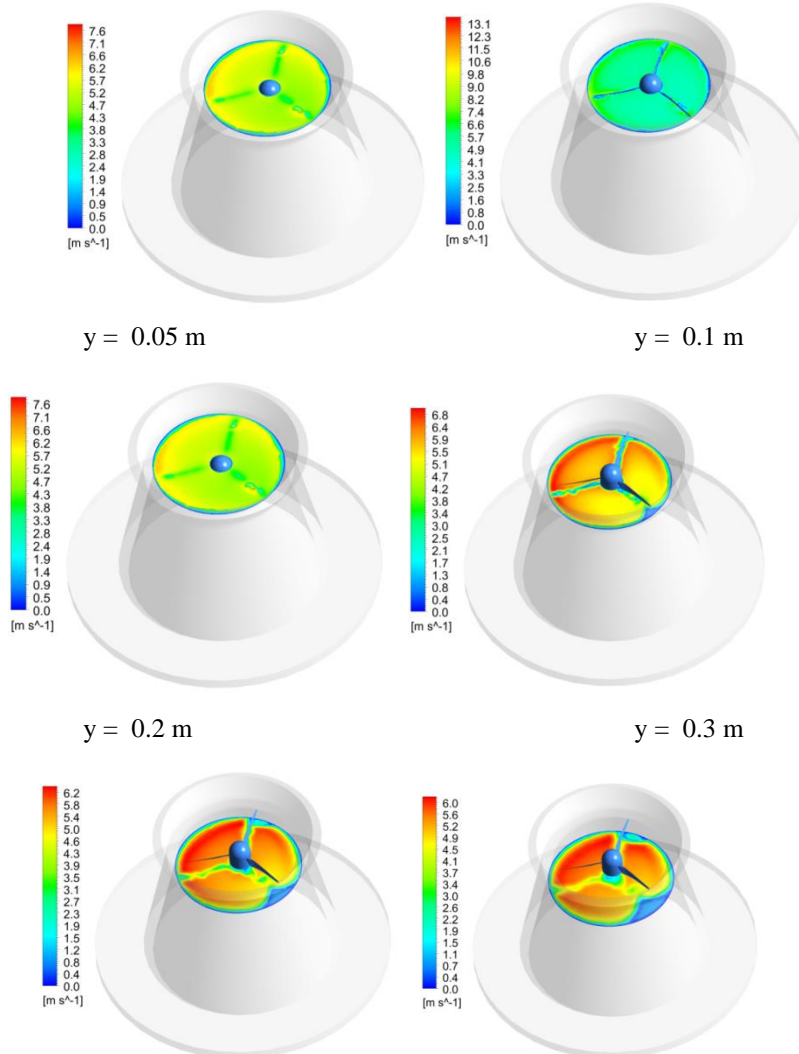


Figure 8: Velocity magnitude contours in the X-Z plane for the shrouded turbine ($U_{wu} = 4 \text{ m/s}$ and $TSR = 7$)

Like the unshrouded turbine, the wind approached the shrouded wind turbine with a wind speed of $U_{wu} = 4$ m/s. The wind speed decreases as it approaches the turbine before it passes through the rotor plane. The axial velocity deficit is the amount of decrease in the freestream velocity, as shown in Fig. 9. The induction factor \bar{a} given by the equation 16 represents the fraction by which the axial component of the velocity is reduced. The average air velocity downstream the wind turbine and where the pressure is recovered back (See Fig. 9) to the atmospheric pressure is used to calculate the induction factor. The back pressure coefficient is calculated from the average wind speed at the shroud exit using equation 13. The power coefficient C_p is then calculated using the equation 11 for the shrouded turbine. The power coefficients versus the TSR were then determined for the shrouded turbines as

shown in Figure 10. The results in Fig. 10 show an increase of the C_p by a factor ranging from 2.46 to 4.33 for the shrouded turbine compared to unshrouded turbine. The numerical results show a net improvement and more pronounced enhancement of the electrical power extracted from the shrouded turbine. These results are in good agreement with the experimental data obtained by Yuji and Takashi [6] for the shrouded wind turbine with a brimmed diffuser. His experimental results show a power augmentation by a factor of about 2–5 compared with a bare wind turbine, for a given turbine diameter and wind speed. The experimental results also show that for long diffuser (Diffuser length $L_t = 1.47 D$), a remarkable increase in the output power of approximately 4-5 times that of a conventional wind turbine is achieved [6].

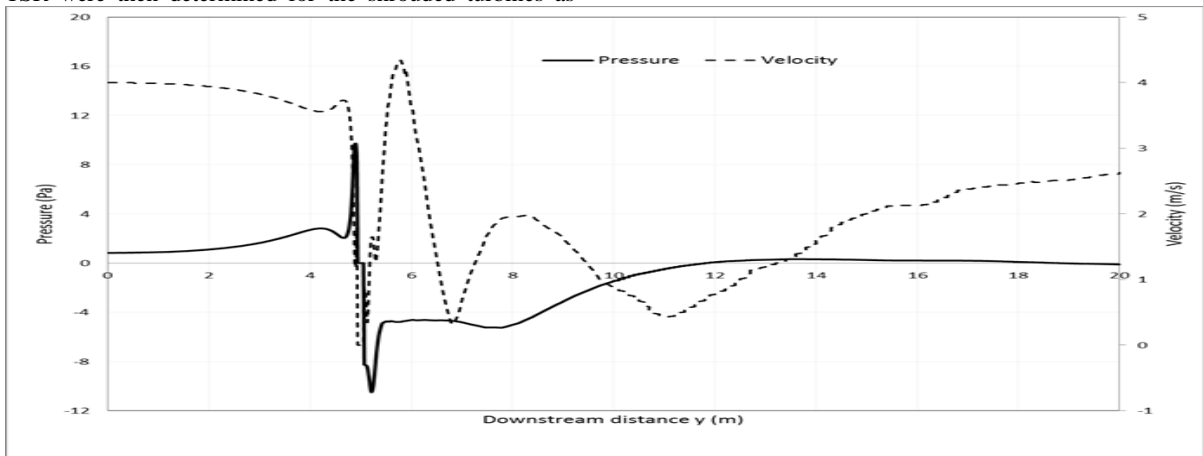


Figure 9: Axial variation of the pressure and velocity magnitude for the shrouded Wind Turbine ($U_{wu} = 4$ m/s, and $TSR = 7$)

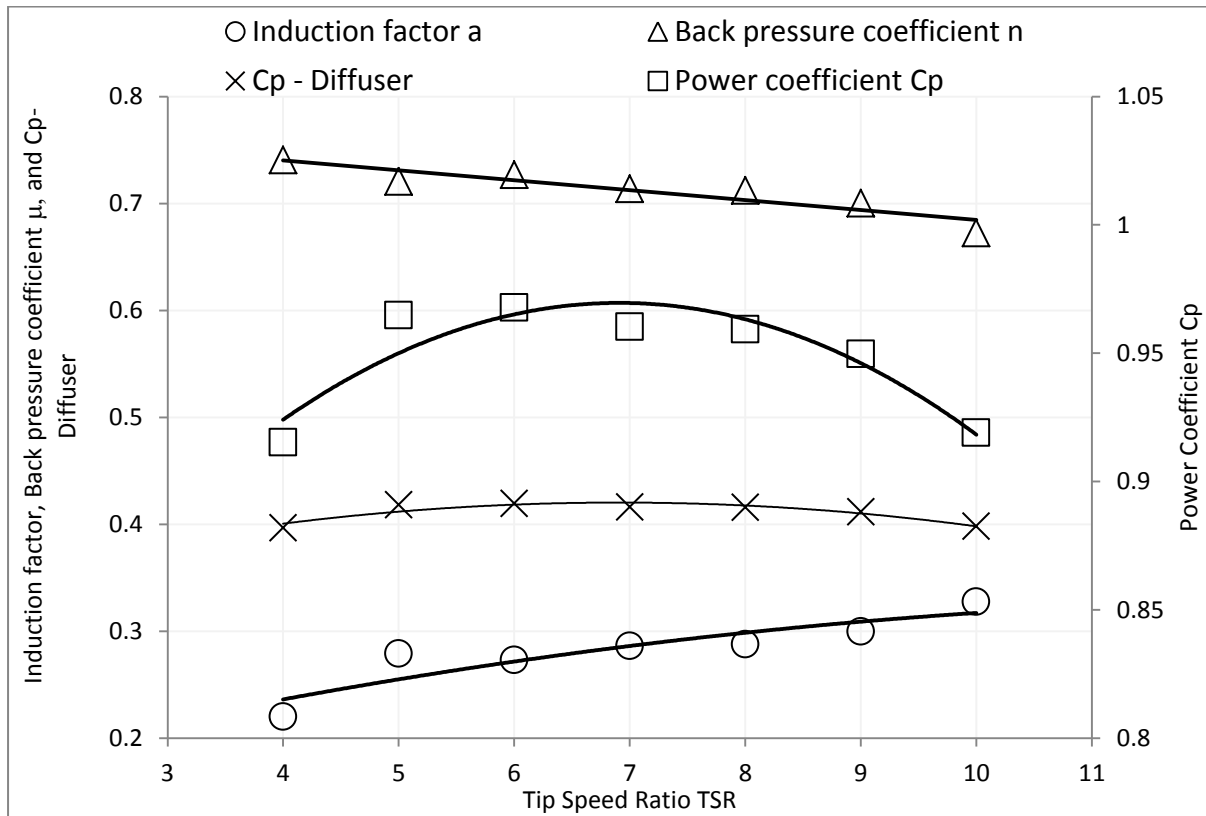


Figure 10: Variation of the power coefficient C_p and induction factor \bar{a} with the tip speed ratio - Shrouded wind turbine ($U_{wu} = 4$ m/s)

6. Conclusions

Computational fluid dynamics analysis was performed in the present study to assess the performance of shrouded HAWT. The governing equations of mass, momentum and turbulence equations were solved using finite volume method to obtain the information about the flow field around the turbine. The induction factor and the power coefficient (C_p) were calculated from the computed velocity profiles. The Computational Fluid Dynamics results and the variation of the C_p versus the tip speed ratio of the unshrouded and shrouded turbines show that the shrouded turbines can generate greater power than the non-shrouded baseline wind turbine; and the variation of the C_p versus the tip speed ratio shows an increase by a four folds compared to the unshrouded turbine. This increase is due to the increase of the air speed inside the shrouded turbines. The present study suggests that shrouded HAWT can be a good solution for energy production in regions with low speed conditions offsetting more fossil fuel usage and reducing their subsequent greenhouse gas emissions.

References

- [1] Chaouki Ghenai, Isam Janajreh, Comparison of resource intensities and operational parameters of renewable, fossil fuel, and nuclear power systems, *International Journal of Thermal and Environmental Engineering*, Volume 5, No2, 95-104, 2013.
- [2] Kanyako F. , Isam Janajreh, Implementation and economical study of HAWT under different wind, *Sustainable Cities and Society*, 15, 2015, 153-160.
- [3] Lew, D. (2000). Alternative to coal and candles: wind power in China. *Energy Policy*, 28, 271-286.
- [4] Hjort S., and Larsen, H., Rotor design for diffuser augmented wind turbines, *Energies*, 8, 10736-10774, 2015.
- [5] Maia, L.A.B, Experimental and Numerical study of diffuser augmented wind turbine, DAWT, Master thesis, December 2014.
- [6] Yuji Ohya and Takahi Krasudani, A Shrouded wind turbine generating high output power with wind lens technology, *Energies*, 3, 634-649, 2010.
- [7] Buyung Kosasih, and Andrea Tondelli, Experimental study of shrouded micro-wind turbine, *Evolving Energy-IEFInternational Energy Congress (IEF-IEC2012)*, *Procedia Engineering* 49 (2012), 92 – 98.
- [8] Jun-Feng Hu, and Wen-Xue Wang, Upgrading a Shrouded Wind Turbine with a Self-Adaptive Flanged Diffuser, *Energies* 8, 2015, 5319-5337.
- [9] Aniket C. Aranake, Vinod K. Lakshminarayan, and Karthik Duraisamy, Computational analysis of shrouded wind turbine configurations using a 3-dimensional RANS solver, *Renewable Energy* 75 (2015) 818-832.
- [10] Aly M. El-Zahaby, A.E. Kabeel, , S.S. Elsayed, M.F. Obiaa, CFD analysis of flow fields for shrouded wind turbine's diffuser model with different flange angles, *Alexandria Engineering Journal*, 56, Issue 1, 2017, 171–179.
- [11] Isam Janajreh, Ilham Talab, Wind Data Collection and Analyses at Masdar City for Wind Turbine Assessment, *Int. J. of Thermal & Environmental Engineering* , Vol. 1, No. 1 (2010) 43-50.
- [12] Isam Janajreh, Ilham Talab, and Jill Macpherson, Numerical Simulation of Tower Rotor Interaction for Downwind Wind Turbine, *Hindawi: Modelling and Simulation in Engineering*, Volume 2010, Article ID 860814, 11 pages, doi:10.1155/2010/860814.
- [13] Ghenai, C., Sargsyan, A., and Janajreh, I., Three dimensional modeling of flow field around a horizontal axis wind turbine (HAWT), *Computational Fluid Dynamics in the Development of Renewable Energy Applications Book*, International Energy and Environment Foundation, 2011.
- [14] I Janajreh, R Qudaih, I Talab, C Ghenai, Aerodynamic flow simulation of wind turbine: downwind versus upwind configuration, *Energy Conversion and Management* 51 (8), 1656-1663.
- [15] Patankar, S. V. (1980). *Numerical Heat Transfer and Fluid Flow*. Taylor & Francis. ISBN 978-0-89116-522-4.
- [16] Ferziger, J. H.; Peric, M. (2001). *Computational Methods for Fluid Dynamics*. Springer-Verlag. ISBN 978-3-540-42074-3.
- [17] Tannehill, J. C.; Anderson, D. A.; Pletcher, R. H. (1997). *Computational Fluid Mechanics and Heat Transfer*. Taylor & Francis.
- [18] Bussel, G.J.W., An assessment of the performance of diffuser augmented wind turbines, Delft University of Technology, *Proceedings of the 3th ASME Joint Fluids Engineering Conference*, San Francisco, California, July 18-23, 1999.
- [19] Bussel, G.J.W., The Science of making more torque from wind: diffuser experiment and theory revisited, Delft University of Technology, *Journal of Physics confer*.

Physical and Chemical Analysis of Ultrasonic Transesterification through Numerical Simulation

M. N. Hussain¹, T. E. Samad² and I. Janajreh^{*3}

¹ Mechanical Engineering Department, Khalifa University of Science and Technology, Masdar Institute, Abu Dhabi 54224, UAE

² Mechanical Engineering Department, Khalifa University of Science and Technology, Masdar Institute, Abu Dhabi 54224, UAE

³ Mechanical Engineering Department, Khalifa University of Science and Technology, Masdar Institute, Abu Dhabi 54224, UAE

Abstract

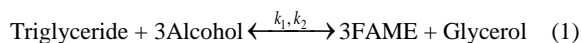
Ultrasound assisted transesterification is increasingly standing out as a highly efficient, reliable and faster way to produce biodiesel from vegetable oil. Applying the same to other feedstock such as used cooking oil, beef tallow or fish oil etc. provides great advantage in terms of yield quality and production time. However, large-scale biodiesel production through ultrasound assisted transesterification is limited by the lack of a continuous sono-chemical reactor, which effectively processes a flow of reactants by simultaneously sonicating them. Design of such a reactor is a complex process since the mechanism is governed by multiple physics such as the ultrasound wave propagation, acoustic cavitation, reactive flow, chemical kinetics etc. In this work a previously designed sono-chemical reactor by the same author is worked upon using numerical simulation to analyze the effectiveness of sonication on the transesterification reaction. The ultrasound mechanism is simulated using the linear wave equation. The acoustic cavitation phenomena which also causes an attenuation of the wave has been accounted for using the complex wave number and impedance. A logical reaction rate coupling model is used to estimate the collective effect of sonication and flow agitation in the reactor. This model system is then applied to study the effect of sonication on the kinetics of reaction and a sensitivity study is carried out. Results show positive effect of alcohol molar ratio in flow agitation case whereas increased molar ratio decreased the sonication rate constant. Biodiesel formation had direct proportionality with applied power and fluid temperature, whereas for frequency sensitivity the results depended on wave number and impedance.

© 2017 Jordan Journal of Mechanical and Industrial Engineering. All rights reserved

Keywords: Biodiesel; Ultrasonic; Sono-chemical; Transesterification; Reactor Design.

1. Introduction

Transesterification is the reaction between triglycerides found in vegetable oil, or used cooking oil and an alcohol such as methanol, which is catalyzed by homogeneous, heterogeneous or enzyme catalysts to produce Fatty Acid Alkyl Esters (FAAE) i.e. biodiesel and a byproduct glycerol. The overall reversible reaction is shown in Eq. 1. It is a slow reaction which needs mechanical agitation to proliferate [1]. Conventionally this can be accomplished by means of a stirrer but such a method is inefficient and needs a relatively long time [2].



Sonication has proved to be a much more efficient option to assist transesterification. The ultrasound wave causes intense cycles of compression and rarefaction at micro levels in the fluid volume which creates cavitation voids or bubbles that contain highly activated vapors of the reactants. The temperature and pressure in these micro bubbles can reach as high as 5,000 K and 1,000 atm [3]. Millions of such bubbles are formed as soon as the sonication is applied. When these bubbles implode they cause tremendous mass transfer in localized zones which intensify the reaction with a localized rate several orders higher than the conventional or stirring flow cases.

There are several works in literature that demonstrate the advantage of sonication over conventional methods of transesterification. Stavarache et al. [4] reported higher yields in shorter time using ultrasonic transesterification under homogeneous catalysts of NaOH and KOH and for the same molar ratio and catalyst amount compared to conventional stirring method. Manickman et al. [5] reported that mechanical agitation takes triple the time to give 78% yield as weighed to ultrasonic transesterification which gives about 93% yield with 1% KOH and 3:1 methanol to oil molar ratio. Apart from the physical effects it is also important to gauge the chemical effects, like free radical formation so as to be reasonable in carrying out kinetic study on sonicated transesterification. Radical chemical specie formation may make such a study highly complex and inaccurate. Extensive work has been carried out in understanding the physical mechanism of ultrasound by some researchers. The results from these works show favorable advantage of physical effects such as formation of fine emulsion, micro mixing etc. over chemical effects. For instance Abhishek et al. [6] studied the prominence of the physical and chemical effects of sonication for the transesterification reaction. Using soybean oil and methanol, they experimented with four molar ratios of 6, 12, 16 and 24 of methanol to 1 mole of oil. They used a 20 KHz frequency ultrasound equipment at moderate input power. Their approach was to couple experimental results with simulation of cavitation bubbles using the Keller-

* Corresponding author e-mail: ijanajreh@masdar.ac.ae.

miksis equation. They found out that the most beneficial aspect of sonication for transesterification reaction is the physical effect like cavitation. Priyanka et al. [7] have also worked on mechanistic investigation of transesterification for soybean oil with methanol and H₂SO₄ using coupled cavitation bubble simulation and determined that physical effects outweigh the chemical effects of ultrasound. Hanif et al. [8] studied the effect of sonication on Jatropha curcas oil at various temperature and molar ratio combinations. They found that the most important physical effect that causes increase in reaction rates pertaining to sonication is the micro level mixing. Design of sonochemical reactors has been carried out by researchers like Sutkar et al. [9]. They simulated the ultrasound wave with modification in the wave number and impedance to predict the cavitation activity in a chemical reactor. They found that the cavitation is high in the zone close to the transducer and then attenuates over the distance away from the transducer due to bubbles.

For a batch process sonication is easily applicable, however, for a continuous process the integration of flow and sonication is crucial and an effective design is tough to achieve. Previously we have worked on studying the chemical effects of sonication [10][11]. In this work, further high fidelity analysis is carried out on a previously designed sono-chemical reactor [12][13]. The goal is to gain a fundamental insight into the localized conversion and species distribution by using numerical simulation and also to analyze the effectiveness of sonication on the transesterification reaction. The ultrasound mechanism is simulated using the linear wave equation. The acoustic cavitation phenomena which also causes an attenuation of the wave has been accounted for using the complex wave number and impedance as per Sutkar et al. [9]. A logical reaction rate coupling model as previously applied in [12][13] and by Jordens et al. [14] is used to estimate the collective effect of sonication and flow agitation in the reactor. This model system is then applied to study the effect of sonication on the kinetics of reaction.

2. Methodology

In this work we have designed a sono-chemical reactor for the transesterification reaction. This reactor has unique sectioning which allows it to utilize all areas of its geometry, and also helps in increasing the throughput of the continuous sono-chemical conversion process. The top section of the reactor is designed for sonication. It uses the sonic energy from the sonotrode and concentrates it in a small section of the reactor such that the maximum volume of the fluid is sonicated. It acts as a pseudo flow cell. The following section is a static mixer section. Having a static mixer helps in further conversion of the unreacted chemicals coming from the sonication section. The design allows the use of different types of static mixers depending on the viscosity of the reacting fluids. The last section is the collection section which helps in initiating the separation of biodiesel and glycerol. The reactor height is 25 cm and diameter is 6 cm. A 2D model is made in COMSOL Multiphysics package for simulating the acoustic, reacting flow and chemical kinetic physics. The reactor geometry is given in Fig. 1.

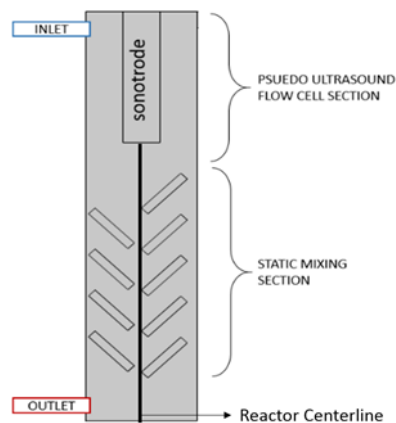


Figure 1: Reactor Geometry

The methodology followed to carry out the intended analysis is illustrated in Fig. 2.

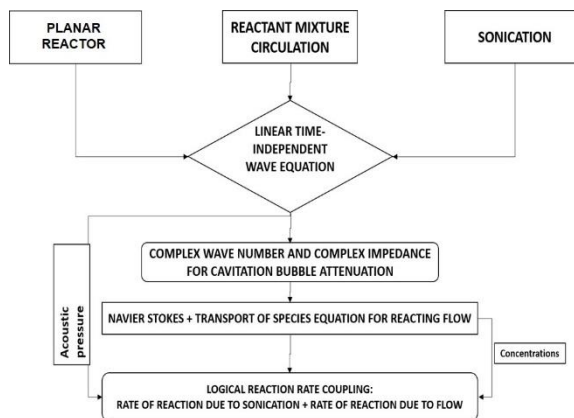


Figure 2: Methodology for analysis

2.1. Linear time-independent wave equation

For simulating the acoustic phenomena, the linear time-independent wave equation was used. In this form of the equation, the pressure is considered as a time-harmonic function, i.e. $P(x, t) = P(x)e^{i\omega t}$. Therefore, the linear wave equation is as in Eq. 2.

$$\frac{1}{\rho} \nabla^2 \mathbf{P} - \frac{k_c^2}{\rho} \mathbf{P} = 0 \quad (2)$$

Where \mathbf{P} is the acoustic pressure and k_c is the attenuated wave. When cavitation bubbles are formed, they allow the reaction to proceed faster, however, they decrease the wave energy by causing attenuation. This restricts the wave from reaching the far ends of the reactor. This has to be accounted for when designing a sono-chemical reactor. In linearized models that appear in literature, this is done by using a complex wave number. As per Sutkar et al. [7], the attenuated wave is simulated using the complex wave number and acoustic impedance as shown in Eq. 3 and 4.

$$k_c = \frac{\omega}{c \sqrt{1 + \frac{i\omega\mu}{\rho c^2}}}, \quad z_c = \frac{\rho c}{c \sqrt{1 + \frac{i\omega\mu}{\rho c^2}}} \quad (3)$$

$$\rho_c = \frac{Z_c k_c}{\omega}, c_c = \frac{\omega}{k_c} \quad (4)$$

Where ρ is the density, c is speed of sound in the medium, Z_c is the complex impedance, ρ_c is the complex density, ω is the angular frequency, μ is the viscosity and C_c is the complex speed of sound.

2.2. Flow simulation

The desired sonicators capacity is between 10 L/hr to 50 L/hr. Therefore, with this in consideration an inlet velocity of 0.0044 m/s is prescribed at the inlet, to have an approximate residence time of 1 min. At such a low velocity the fluid is in the laminar region. Hence, the Navier–Stokes equations for 2D, incompressible, viscous, laminar flow are used to simulate the reactant flow in the reactor as given in Eq. 5.

$$\rho(\mathbf{u}\nabla\mathbf{u}) = -\nabla P_{flow} + \mu\nabla^2\mathbf{u} + \rho\mathbf{g} \quad (5)$$

Where, \mathbf{u} is the velocity field, \mathbf{g} is the gravitational acceleration, P_{flow} is the pressure.

2.3. Reactant transport

For simulating the reaction within the flow and the conversion of species the transport of dilute species equation is used (see Eq. 6).

$$\nabla(-D\nabla c_i) + \mathbf{u}\nabla c_i = R_{rate} \quad (6)$$

D is the diffusion coefficient, c_i is molar concentration of the i^{th} specie, R_{rate} is the rate of reaction and \mathbf{u} is the velocity profile from the flow simulation. The Arrhenius model for the reaction kinetics is given in Eq. 7 as:

$$K_{flow} = A \cdot e^{\frac{-E}{R_u T}} \quad (7)$$

Where K is the rate constant, A is the pre-exponential factor, E is the activation energy, R_u is the universal gas constant and T is the temperature. The activation energy and pre-constants are obtained from the work of Nouredini et al [15].

2.4. Reaction rate coupling

The rate of reaction R_{rate} was taken as pseudo first order model as per the work of Freedman et al. [16]. To couple the rate of reaction due to sonication and flow agitation the method by Jordan's et al. [14] was adopted. In this procedure the Arrhenius rate constant of sonication was calculated, where the temperature is the one that inside the cavitation bubble. The temperature is calculated using the adiabatic ideas gas transition equation. The rate constant and the cavitation bubble temperature are as per Eq. 8 and 9.

$$k_{son} = A \cdot e^{\frac{-E}{R_u T_{bubble}}} \quad (8)$$

$$T_{bubble} = \frac{T_L P (\gamma - 1)}{P_{vapor}} \quad (9)$$

Where k_{son} is the sonication rate constant, T_{bubble} is the

cavitation bubble temperature, γ is the specific heat ratio, P is the acoustic pressure and P_{vapor} is the vapor pressure. T_L is the liquid temperature however in this study we have taken a fixed value of T_L at 333 K, to have at-least the vapor phase of methanol, since methanol evaporates at 333 K. P_{vapor} was taken as the molar average of the vapor pressures of vegetable oil and methanol.

Using Eq. 8 and 9 in a logical coupling model the coupled reaction rate was calculated. This is setup such that the sonication reaction rate is applied only when the acoustic pressure is above the Blake pressure. The coupling model is given in Eq. 10.

$$-R_{rate} = [(P > P_{blake})\beta k_{son} * [Oil * Methanol] + (1 - \beta)k_{flow} * [Oil * Methanol]] \quad (10)$$

And β is the cavitation bubble volume which is calculated from Eq. 11 [12] [14] and [17].

$$\beta = 2x10^{-9}P \quad \text{for } p_{blake} < P < 1x10^8 Pa. \quad (11)$$

2.5. Boundary conditions

The initial amplitude at the transducer was calculated from Eq. 12.

$$P_w = \sqrt{\frac{2\rho C P_d}{A}} \quad (12)$$

P_w is the initial amplitude in Pa, P_d is the rated power in Watt and A is the area of the transducer. At the walls of the reactor the Dirichlet boundary condition $P=0$ was applied implying pressure release, which is valid when the material is highly absorbing such as Teflon [18].

For the laminar flow velocity of 0.0044 m/s was specified at the inlet and at the outlet $P_{flow} = 0$ was applied. For the transport equation the inlet was specified in terms of concentrations.

3. Results And Discussion

In previous studies related to sono-chemical reactors the simulations were carried out with only single liquid in perspective, but in our study we have a mixture of liquids. Hence the effective properties need to be evaluated. The speed of sound was calculated using Eq. 13.

$$C = \sqrt{\frac{K_E}{\rho_E}} \quad (13)$$

Where K_E and ρ_E are equivalent bulk modulus and equivalent density calculated from volume fractions of the reactants.

For calculating equivalent viscosity the Refutas equation was used. In this method the viscosity blend for the reactants is calculated (see Eq. 14). Using mass fractions the blend index of the mixture is evaluated (see Eq. 15) and finally the effective viscosity is calculated from Eq. 16.

$$VBN_i = 14.534 \times \ln(\ln(v_i + 0.8)) + 10.975 \quad (14)$$

$$VBN_{mixture} = \sum_{i=0}^N x_i \times VBN_i \quad (15)$$

$$\begin{aligned} v_{mixture} &= \left(\exp\left(\exp\left(\frac{VBN_{mixture} - 10.975}{14.534}\right)\right) \right) \\ &- 0.8 \end{aligned} \quad (16)$$

Where VBN is the viscosity blend index, v_i is the kinematic viscosity of the element in cSt, and x_i is the mass fraction.

3.1. Acoustic Pressure Simulation

The acoustic simulation was initially carried out at a frequency of 24,000 Hz and rated power of 100 W. The wave attenuation was clearly evident from the results as can be seen in Fig. 3. The peak pressures were not very different in the two cases but the acoustic pressure waveform was flattened much closer to the sonotrode tip in the case of attenuated pressure. It is observed that in both the cases the acoustic pressure over the static mixer is lower as compared to the acoustic pressure in the flow cell section. This is due to the mixer blades obstructing the

sound wave. Due to this obstruction the sonic energy is concentrated in the region close to the sonotrode. The energy concentration per unit area is higher between the sonotrode and the start of the static blades as compared to any other area in the reactor. This helps in better conversion of reactants and without using additional energy. Using such a design reduces the need for having multiple sonotrodes, which add up to the power consumption and cost. Hence, the design seems superior in terms of utilizing the acoustic energy effectively.

3.1.1 Acoustic sensitivity

To evaluate the design a parametric study was carried out. This study is aimed at identifying the best values of the acoustic parameters to achieve better conversion. The parameters that best govern the acoustic performance of the reactor are the rated power and frequency of the equipment. A parametric study with 5 cases of rated powers and 3 cases of wave frequency was carried out. The rated power was varied from 100 to 300 W in steps of 50 W and three frequencies i.e. 24, 36 and 70 kHz were studied. The results of the attenuated acoustic pressure at different powers is shown in Fig. 4 and the results from the frequency study are shown in Fig. 5.

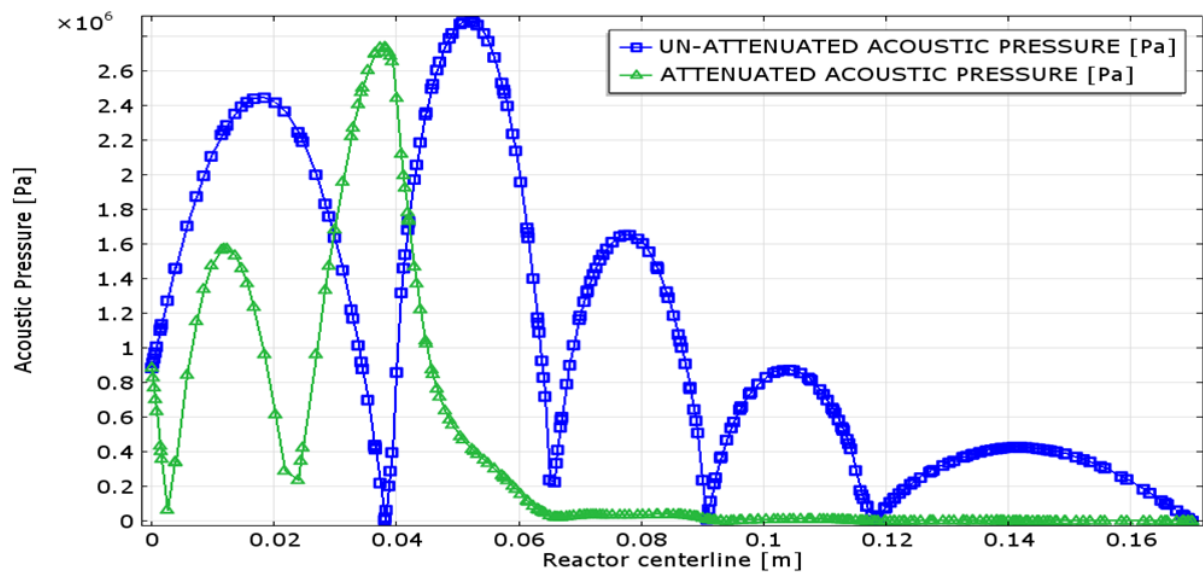


Figure 3: Acoustic Pressure simulation at 100 W and 24000 Hz.

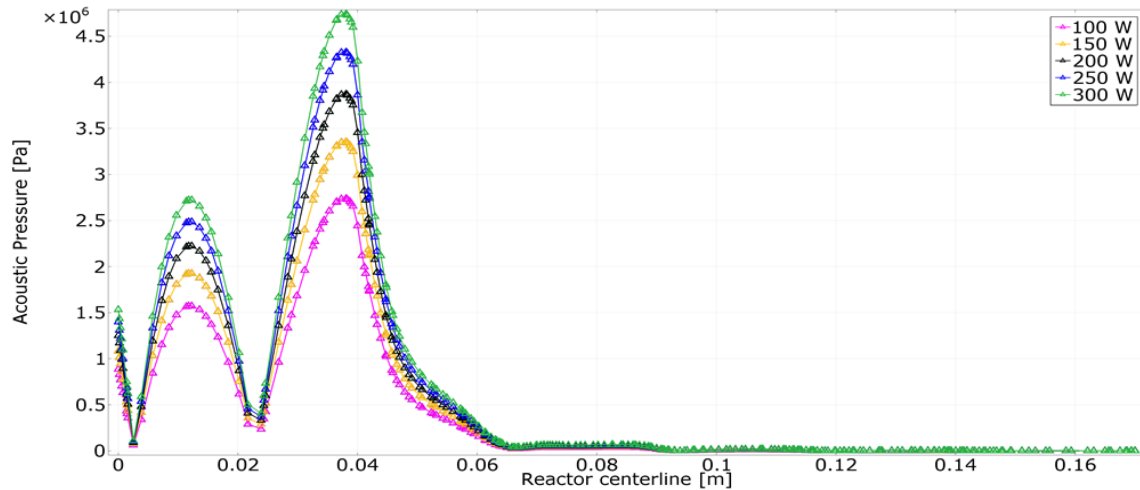


Figure 4: Attenuated acoustic pressure at different power levels at 24000 Hz.

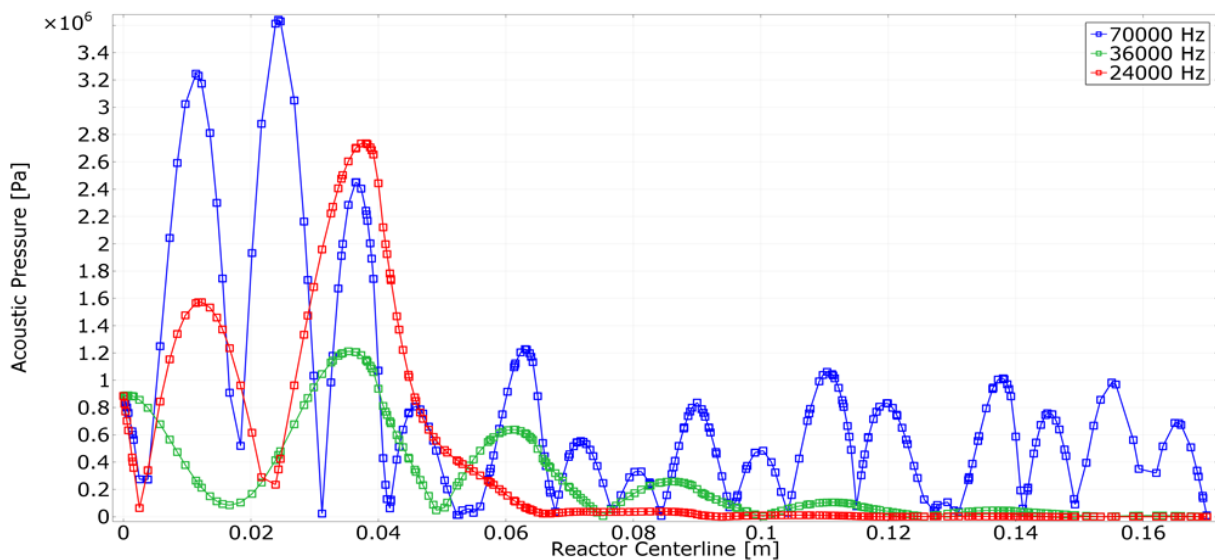


Figure 5: Attenuated acoustic pressure at different frequencies and 100 W power

Power sensitivity: The simulated peak acoustic pressure showed a direct proportionality to the rated power. As the power increased the peak pressure also increased but the pressure distribution profile remained similar. The least acoustic peak pressure of 2.6 MPa was observed under 100 W power at a distance of 0.04 m from the sonotrode. Under a power of 150 W the acoustic pressure was raised to 3.4 MPa whereas the maximum peak pressure of 4.6 MPa was observed at 300 W power at the same position. After a distance of 0.06 m from the sonotrode the pressure started to flatten out.

Frequency Sensitivity: In the frequency study, no defined relation between the acoustic pressure and applied frequency was observed. The peak pressure was highest in case of the highest frequency of 70 kHz, which was about 3.7 MPa. The lowest peak acoustic pressure was observed at 36 kHz which was about 1.2 MPa. This undulation in the peak pressure at different frequencies can be attributed to the relative variation between the transducer initial amplitude, complex wave number and complex impedance. It is observed that a higher acoustic pressures are favored by either a higher imaginary part of the impedance or a higher real part of the wave number. At the frequency of 24 kHz the imaginary part of the impedance is higher whereas at a frequency of 70 kHz the real part of

wave number is higher. At 36 kHz their combination does not support increase in acoustic pressures. At a higher frequency acoustic pressures were observed to be stronger in the whole length of the reactor including the static mixer section. At 36 kHz, though the acoustic pressure is low the wave flattens at a distance of 0.12 m which is higher than what is observed at 24 kHz.

Based on this study it can be said that higher frequencies are better for this reactor and this fluid medium. For different fluids this depends on the density and speed of sound.

3.2. Reactive Flow Simulation

The transesterification reaction highly depends on two factors, the molar ratio and temperature. But when carried out under sonication, the rated power and frequency also affect the product proliferation. As per stoichiometry, one mole of oil needs three moles of methanol to produce three moles of FAME. But this is the ideal case. Increase in molar ratio usually needed and that provides better conversion. This is simply since there is more methanol for every mole of oil which increases the interaction between the reactants on in accordance to Le Chatelier's principle. However, there is a limit to increasing molar ratio. Excess

methanol causes post-process separation difficulties. Excess methanol in the produced fuel renders the fuel unsuitable as per the ASTM standards.

As for temperature, since the Arrhenius kinetic model is adopted the rate constant increases with increase in temperature, thereby increasing the reaction rate. For the reactant volume the max temperature that the reactants can be raised to is 333 K, which is the boiling point of methanol. The power and frequency only affect the cavitation bubble temperature and the sonication rate constant. The calculated bubble temperatures were much higher than the fluid domain temperatures. The sonication rate constants were several orders higher than the conventional rate constants.

Results clearly show that sonication is indisputably better than agitation methods. Visualizations of biodiesel concentrations showed higher concentrations forming between the static mixer blades. A sensitivity study has been carried out to study the effect of molar ratio, temperature, power and frequency on the sonication rate constant.

3.2.1 Reaction sensitivity

Molar ratio sensitivity: For the flow agitation, with increasing molar ratio the biodiesel concentration in the

reactor also increased which is the obvious effect of the increased interaction of reactants. Benefit of having static mixer is proved since higher concentrations of biodiesel were observed between the blades. On the sonication part, with increasing molar ratio it was observed that the temperature of the bubble decreased. This decreased the sonication rate constant. This decrease is caused by the rise in vapor pressure of the cavitation bubble with increase in methanol. This result implies that higher molar ratios are not actually beneficial at the localized level, or more specifically at the scale of a cavitation bubble. This also provides the benefit of adopting lower molar ratios for sonicated transesterification. Fig. 6 shows the concentration profile in the reactor for different molar ratios. The max bubble temperature was observed at molar ratio of 1: 3 at all power levels.

Temperature Sensitivity: As a result of the Arrhenius model, higher concentrations were observed for higher fluid temperatures. There was no effect of temperature on the cavitation bubble temperature or the sonication reaction constant. Fig. 7 gives the concentration profile of biodiesel in the reactor at different temperatures.

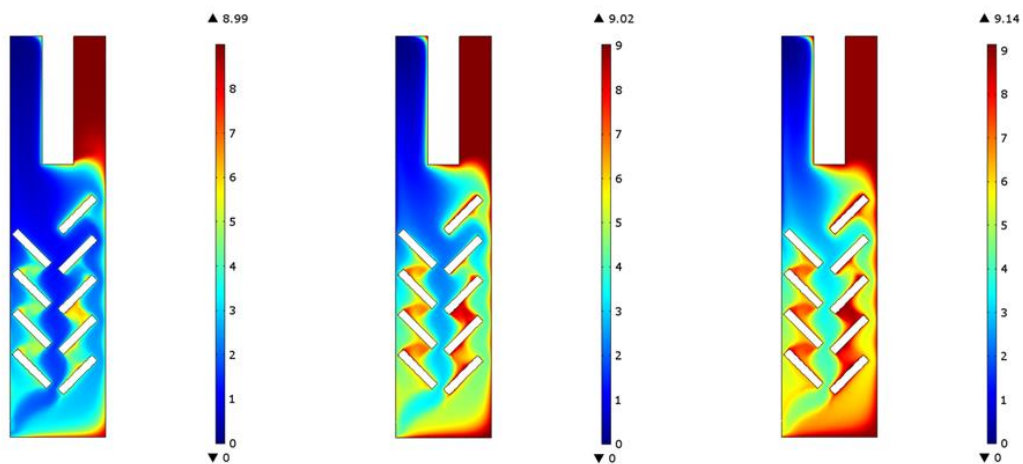


Figure 6: Biodiesel concentration profile (mol/m^3) at molar ratios of 3:1, 6:1 and 9:1 at 330 K temperature

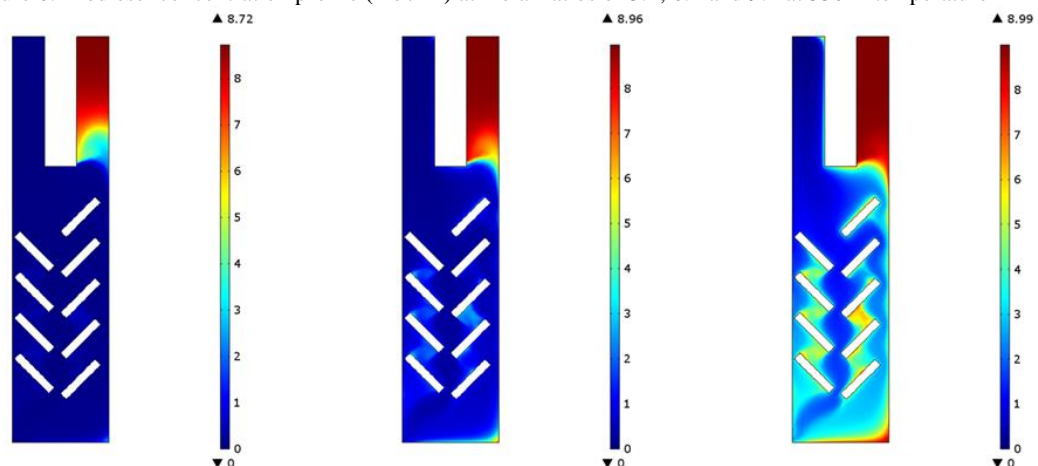


Figure 7: Biodiesel concentration profile (mol/m^3) at 310 K, 320 K and 330 K at 3:1 molar ratio.

Power Sensitivity: As mentioned in the above sections, power increase resulted in a direct increase of acoustic pressures inside the reactor. As from Eq. 9 and 10 we see that the cavitation bubble temperature and rate constant are dependent on the acoustic pressure. To study the same a sensitivity study with 5 different power levels was carried out. Results adhere to relations in the equations. Higher bubble temperature and higher sonication rate constant were observed with increase in rated power. The maximum values were calculated at a power of 300 W.

Frequency sensitivity: The variation in cavitation bubble temperature and K_{son} with frequency was closely similar to that of acoustic pressure. The highest values were obtained at a frequency of 70 kHz and the lowest values were obtained at a frequency of 36 kHz. This variation again implies that higher frequencies are better for this reactor design and fluid medium.

The results for the surface averaged cavitation bubble temperature and sonication rate constant for molar ratio sensitivity are given in Fig. 8. and those for frequency sensitivity are given in Fig. 9.

4. Conclusions

In this work a multi-physics simulation of sonicated transesterification was carried out by following procedures that were experimentally validated in literature to study the physical and chemical effects. The acoustic pressure waves were simulated by the Helmholtz equation. The wave

attenuation due to cavitation was accounted for using complex wave number and impedance. The reactive flow was simulated using a coupled Navier-Stokes and species transport equations. To simulate the cavitation bubble temperature and reaction rates, a logical coupling model based on acoustic pressure was applied. The Arrhenius kinetic model was used for calculating the reaction kinetics. A novel reactor with unique sectioning was tested. A sensitivity study was carried out to study the effect of power, frequency, molar ratio and temperature on biodiesel formation in the reactor. Results showed the rated powers is directly proportional to the bubble temperatures and the reaction rate constants. For the frequency study it was observed that the best conversion results were obtained at 70 kHz and the poorest were at 36 kHz. As for molar ratio, higher molar ratios increased biodiesel formation for the flow agitated conditions but an opposite trend was observed for the sonication case. At higher molar ratios cavitation bubble temperature was lower leading to reduction in the rate constant. This implies that at the localized level the stoichiometric molar ratio is desirable. In the temperature study it was observed that the increase in temperature had a direct relation with biodiesel formation. Apart from studying the effects of sonication, this study also aimed at broadly testing the performance of the reactor design. From the simulations it was clear that having a pseudo flow cell section and a static mixer adds to the performance of a sono-chemical reactor.

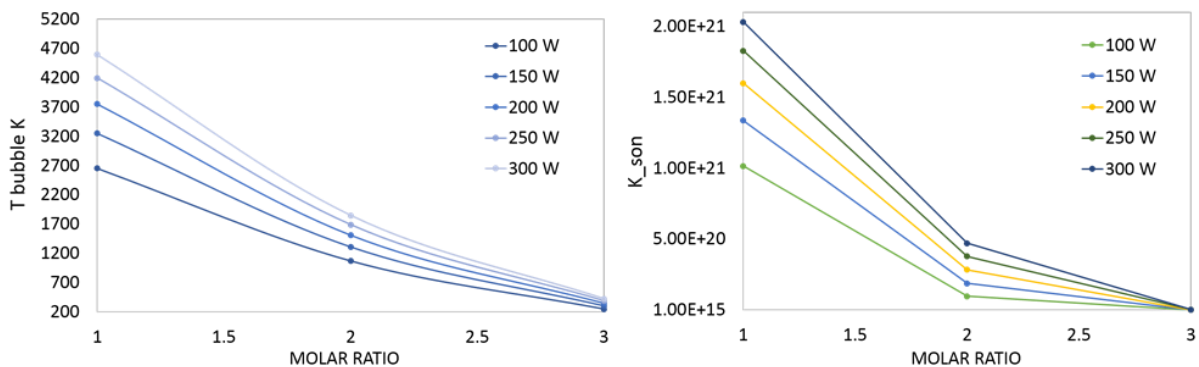


Figure 8: Cavitation bubble temperature and K_{son} at different powers and molar ratio at 24000 Hz.

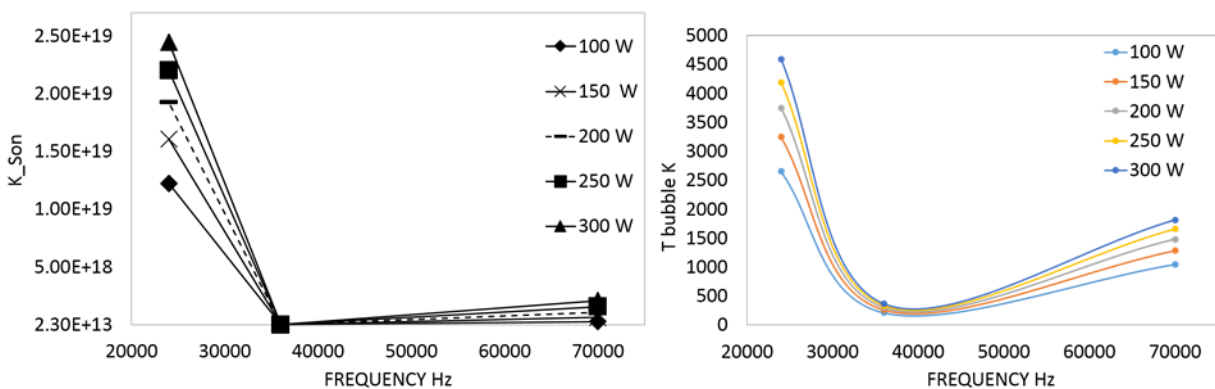


Figure 9: K_{son} and cavitation bubble temperature at different powers and frequencies at 3:1 molar ratio.

Property Table

Property	Unit	Value
Activation energy, E	J/Mol	164958.4
Adiabatic coefficient, γ	-	1.4
Ambient liquid pressure, P_{liq}	Pa	1.00E+05
Blake threshold P_{blake}	Pa	1.00E+05
Oil density [19]	Kg/m ³	883
Dynamic viscosity of oil [20]	Pa.s	1.62E-02
Density of methanol [21]	Kg/m ³	883
Dynamic viscosity of methanol [22]	mPa.s	0.545
Pre-exponential factor A	m ³ /mol/s	3.49E+22
Vapor pressure of vegetable oil [23]	Pa	543
Vapor pressure of methanol[24]	Pa	13020
Universal gas constant R_u	J/mol.K	8.314
Bulk modulus of Methanol [25]	N/m ²	0.8E9
Bulk modulus of Oil [26]	N/m ²	2.1E9

References

- [1] RA Rabu, I Janajreh, C Ghenai, "Transesterification of biodiesel: process optimization and combustion performance", *Int. J. of Thermal & Environmental Engineering* vol. 4 no. 2, 129-136, 2012
- [2] RA. Rabu, I. Janajreh, D. Honnery, "Transesterification of waste cooking oil: process optimization and conversion rate evaluation, *Energy Conversion and Management* Vol. 65, (2013), 764-769
- [3] V. G. Gude, G. E. Grant. "Biodiesel from waste cooking oils via direct sonication", *Applied Energy*, Vol.109, pp.135-144. 2013.
- [4] C. Stavarache, M. Vinatoru, Y. Maeda, "Ultrasonic versus silent methylation of vegetable oils", *Ultrasonics Sonochemistry*, vol. 13, pp. 401-407, 2005.
- [5] S. Manickam, V. N. D Arigela, P. R. Gogate, "Intensification of synthesis of biodiesel from palm oil using multiple frequency ultrasonic flow cell", *Fuel Processing Technology*, vol. 128, pp. 388-393, 2014.
- [6] K. Abhishek, S. Thirugnanasambandam, S. M. Vijayanand, "Physical mechanism of ultrasound-assisted synthesis of biodiesel", 48, 5534-544 , 2009.
- [7] A. P. Priyanka, A. C. Hanif, S. M. Vijayanand, "Mechanistic and kinetic investigations in ultrasound assisted acid catalyzed biodiesel synthesis", 187, 248-260, 2012.
- [8] A. C. Hanif, C. Sankar, S. M. Vijayanand, "Mechanistic insight into sonochemical biodiesel synthesis using heterogeneous base catalyst", 21, 169-181, 2014.
- [9] V. S. Sutkar, P. R. Gogate, L. Csoka, "Theoretical prediction of cavitation activity distribution in sonochemical reactors", *Chemical Engineering Journal*. 74,1457 – 1463, 1997.
- [10] I. Janajreh, T. E. Samad, M. N. Hussain, "Intensification of transesterification via sonication numerical simulation and sensitivity study", *Applied energy*, *Applied Energy* Vol. 185 2151-2159, 2017.
- [11] M. N. Hussain, T. E. Samad, M. Daqaq, I. Janajreh, "Numerical modelling of sonicated, continuous transesterification and evaluation of reaction kinetics for optimizing biodiesel reactor design", *International Journal of Thermal and Environmental Engineering* Vol.11 No.1, 79-86, 2016.
- [12] MN Hussain, S. Al-Kaabi, I. Janajreh, "Optimizing acoustic energy for better transesterification: a novel sono-chemical reactor design", *Energy Procedia* Vol. 105 544-550, 2017.
- [13] MN Hussain, I. Janajreh, "Acousto-chemical analysis in multi-transducer sonochemical reactors for biodiesel production", *Ultrasonics sonochemistry* Vol. 40 184-193, 2018.
- [14] J. Jordens, A. Honings, J. Degrève, L. Braeken, and T. V. Gerven. "Investigation of design parameters in ultrasound reactors with confined channels", *Ultrasonics Sonochemistry*, 20, 1345-1352, 2013.
- [15] H. Nouredini, D. Zhu. "Kinetics of Transesterification of Soybean Oil", *Journal of the American Oil Chemists Society*, Vol.74 No.11, 1457-1463, 1997.
- [16] B. Freedman, R. O. Butterfield, and E. H. Pryde, "Transesterification kinetics of soybean oil", *JAACS* Vol.63 No.10, 1375-1380, 1986.
- [17] R. Jamshidi, B. Pohl, U. A. Peuker, G. Brenner, Numerical investigation of sono-chemical reactors considering the effect of inhomogeneous bubble clouds on ultrasonic wave propagation, *Chem. Eng. J.*, 189–190, 364–375, 2012.
- [18] Maples, E. Robert. "Petroleum Refinery Process Economics", Pennwell Books. ISBN 0-87814-779-9, 2000.
- [19] B. D. Nikoli, B. K., S. D. Markovi, and M. S. Mitrovi. "Determining the speed of sound, density, and bulk modulus of rapeseed oil, biodiesel, and diesel fuel", *Thermal Science*, 16(2), 505-514, 2012.
- [20] O.O. Fasina and Z. Colley, "Viscosity and specific heat of vegetable oils as a function of temperature: 35°C to 180°C", *International Journal of Food Properties*, 11, 738–746, 2008.
- [21] D. R. Lyde, "CRC Handbook of Chemistry and Physics", CRC Press. ISBN 0-8493-0486-5, 2005.
- [22] González, Begona. "Density, dynamic viscosity, and derived properties of binary mixtures of methanol or ethanol with water, ethyl acetate, and methyl acetate at T = (293.15, 298.15, and 303.15) K", *The Journal of Chemical Thermodynamics* 39 (12): 1578–1588. doi:10.1016/j.jct.2007.05.004. 2007.
- [23] P. M. Ndiaye, F. W. Tavares, I. Dalmolin, C. Dariva, D. Oliveira, J. V. Oliveira, "Vapor Pressure Data of Soybean Oil, Castor Oil, and Their Fatty Acid Ethyl Ester Derivatives", *J. Chem. Eng. Data*, 50, 330-333, 2005.
- [24] H. F. Gibbard and J. L. Creek, "Vapor pressure of methanol from 288.15 to 337.65 K", *J. Chem. Eng. Data*, 19 (4), pp 308–310, 1974.
- [25] B. Nesbitt. "Handbook of pumps and pumping", Elsevier, ISBN-978-1-85617-476-3, 2006.
- [26] B. D. Nikolic, K. E. G. L. Breda, S. D. Markovic, M. S. Mitrovic, "Determining the speed of sound, density, and bulk modulus of rapeseed oil, biodiesel, and diesel fuel", *Thermal science* 16(2), 2012



الجامعة الهاشمية



المملكة الأردنية الهاشمية

المجلة الأردنية
للمهندسة الميكانيكية والصناعية

JJIMIE

مجلة علمية عالمية محكمة
تصدر بدعم من صندوق البحث العلمي

اصدار خاص

<http://jjmie.hu.edu.jo/>

ISSN 1995-6665

المجلة الأردنية للهندسة الميكانيكية والصناعية

مجلة علمية عالمية محكمة

المجلة الأردنية للهندسة الميكانيكية والصناعية: مجلة علمية عالمية محكمة تصدر عن
الجامعة الهاشمية بالتعاون مع صندوق دعم البحث العلمي في الأردن

هيئة التحرير

محرر زائر

الأستاذ الدكتور محمد احمد مدان
الجامعة الاردنية

رئيس التحرير

الأستاذ الدكتور أحمد الغندور.

قسم الهندسة الميكانيكية و الصناعية، الجامعة الهاشمية، الزرقاء، الأردن.

الأعضاء

الأستاذ الدكتور محمد أحمد حمدان
الجامعة الاردنية

الأستاذ الدكتور ناصر الحنيطي
الجامعة الاردنية

الأستاذ الدكتور نسيم سواقد.
جامعة مؤتة

الأستاذ الدكتور محمد هياجنه.
جامعة العلوم والتكنولوجيا الاردنية

الأستاذ الدكتور أمين الربيدي.
جامعة البلقاء التطبيقية

الأستاذ الدكتور سهيل كيوان
جامعة العلوم والتكنولوجيا الاردنية

الأستاذ الدكتور محمد ضيف الله الطاهات
الجامعة الاردنية

فريق الدعم

المحرر اللغوي

الدكتور قصي الذبيان

تنفيذ وإخراج

م . علي أبو سليمة

ترسل البحوث إلى العنوان التالي

رئيس تحرير المجلة الأردنية للهندسة الميكانيكية والصناعية

الجامعة الهاشمية

كلية الهندسة

قسم الهندسة الميكانيكية

الزرقاء - الأردن

هاتف : 00962 5 3903333 فرعي 4537

Email: jjmie@hu.edu.jo

Website: www.jjmie.hu.edu.jo